Master thesis and internship[BR]- Master's thesis : EINSTEIN Telescope: Multi-disciplinary optimization of the overall architecture[BR]- Integration internship

Auteur : Lanis, Louison
Promoteur(s) : Jacques, Lionel; Collette, Christophe
Faculté : Faculté des Sciences appliquées
Diplôme : Master en ingénieur civil en aérospatiale, à finalité spécialisée en "aerospace engineering"
Année académique : 2024-2025
URI/URL : http://hdl.handle.net/2268.2/23326

UNIVERSITE DE LIEGE
FACULTE DES SCIENCES APPLIQUEES

CENTRE SPATIAL DE LIÈGE

EINSTEIN Telescope: Multi-disciplinary optimization of the overall architecture

Master's thesis submitted by **Louison Lanis** in order to obtain the degree of Master of Science in Aerospace Engineering

Supervisor:
Lionel Jacques

Co-supervisor:
Christophe Collette

Academic year 2024-2025

Abstract

This thesis investigates the feasibility of using a fully radiative cryostat to cool a suspended mirror to cryogenic temperatures, as required by the Einstein Telescope Low Frequency (ET-LF) gravitational wave detector. The study is based on the E-TEST prototype developed at the Centre Spatial de Liège (CSL).

The first part of the work analyzes the current E-TEST cryostat to assess its performance and identify its limitations. This includes a vibrational study of a single cryostat fin and a thermal analysis using a simplified lumped-parameter model. The vibrational analysis showed that the first natural frequencies of the fins exceed $10\,\mathrm{Hz}$, avoiding resonance with typical environmental disturbances. The validated thermal model confirmed that the mirror can be cooled to $22\,\mathrm{K}$ in less than three weeks.

Based on these results, several improvements were suggested. Low-complexity modifications included resizing the top baffle tubes and applying emissive paint to increase the emissivity of the interior surfaces. An alternative assembly process was also introduced to avoid the temporary disassembly of the inverted pendulum structure.

On the high-complexity side, the radiative heat exchanger (RHX) was completely redesigned to improve space efficiency and assembly. A circular RHX with vertical rectangular fins arranged circumferentially was found to be the most promising. Alternative fin geometries were also explored, showing that black-painted honeycomb fins could potentially reduce the mirror temperature to $20.4\,\mathrm{K}$.

These concepts were then scaled to ET-LF constraints. RHX designs were adapted accordingly, with shorter fins in front of optical apertures and longer ones elsewhere to balance radiative area and clearance around the payload for maintenance access. A final thermal analysis confirmed that the suggested RHX configuration can achieve the target mirror temperature of $20\,\mathrm{K}$.

This thesis demonstrates the feasibility of a fully radiative cryostat for the Einstein Telescope and lays the groundwork for future studies in vibration modeling, thermal noise, and mechanical design optimization.

Acknowledgments

First and foremost, I would like to express my deepest gratitude to my supervisor, Lionel Jacques, for his patience, his interest in the project, and his unwavering commitment. His availability and support were essential to the successful progress of this work.

My warmest thanks also go to my co-supervisor, Christophe Collette, for his expertise and the insightful advice he provided throughout the development of the project.

I am also grateful to all the professors and teaching assistants I encountered during my academic studies. Their teaching and guidance enabled me to acquire the necessary knowledge and skills to undertake this research.

Support from family and friends has been equally important. I am especially thankful to my mother, whose constant encouragement helped me persevere throughout my studies, even in the most difficult moments.

Lastly, sincere thanks go to everyone who, in one way or another, contributed to the realization of this thesis.

ACRONYMS

ET	Einstein Telescope
ET-LF	Einstein Telescope Low Frequency
ET-HF	Einstein Telescope High Frequency
E-TEST	Einstein Telescope Euregio-Meuse-Rhin Site and Technology
RHX	Radiative Heat Exchanger
IRHX	Internal Radiative Heat Exchanger
ERHX	External Radiative Heat Exchanger
GHe	Gaseous Helium
LN_2	Liquid Nitrogen
IP	Inverted Pendulum
MA	Marionette
PF	Platform
FEM	Finite Element Model
MLI	Multi-Layer Insulation
LIGO	Laser Interferometer Gravitational-Wave Observatory
KAGRA	Kamioka Gravitational Wave Detector

CONTENTS

CHAPTER 1

INTRODUCTION

1.1 Scientific context and state of the art

A century ago, Albert Einstein discovered one of the most exciting new finds in physics, gravitational waves. These waves carry information that cannot be obtained in any other way and allow researchers to learn about the early universe. Indeed, gravitational waves are generated by the most extreme events in the cosmos and are disruptions in space-time, like ripples across a pond traveling at the speed of light [1]. In fact, every acceleration of mass produces changes in the space-time curvature in the form of waves, but only a few of them can be detected. This is due to the weakness of the gravity force and the stiffness of space-time. Therefore, gravitational waves are very small, and only the ones generated by massive astronomical objects accelerating very quickly, such as supernovae, neutron stars, or black holes orbiting each other, can be detected [2].

This detection is made with interferometers using the fact that, when a gravitational wave passes by Earth, it squeezes space-time slightly in one direction and stretches it at a right angle. Nevertheless, due to the tiny size of the gravitational waves, the amount of stretch and squeeze of space is also tiny. That is why the instruments must be extremely precise.

The first instrument created to directly detect gravitational waves was the Laser Interferometer Gravitational-Wave Observatory (LIGO), inaugurated in 1999 and built in the United States. Both detectors of LIGO are giant Michelson interferometers with $4\,\mathrm{km}$ long arms, arranged in the shape of an L. Other similar instruments were later built in other parts of the world, such as Virgo, a $3\,\mathrm{km}$ long arm interferometer inaugurated in 2003 and situated in Italy. Actually, the LIGO Scientific Collaboration and the Virgo Collaboration have been working together and have released joint analyses, data sets, and papers since 2010 [3].

Later on, new detectors were developed, including the Kamioka Gravitational Wave Detector (KAGRA) in Japan. The particularity of KAGRA is that it was the first underground interferometer and the first to use cryogenic mirrors. It operates with pulse tube cryocooler and high thermal conductivity low stiffness 6N pure aluminum heat links to cool at $20\,\mathrm{K}$ sapphire mirrors [4]. However, even if this strategy works to cool the mirror to the wanted temperature for ET, the suspension design to mechanically decouple the mirror and isolate it from the cryocooler vibration is very complex[5].

Another new detector is the future American detector, named LIGO Voyager. This detector uses radiative heat transfer instead of conduction to cool the mirror at $123\,\mathrm{K}$ [6]. The cooling is made through two non-contact cylindrical cold shields surrounding the test mass[7].

A further one, more advanced, is the Einstein Telescope (ET). It belongs to the third generation of gravitational-wave observatory instruments. The Einstein Telescope is an underground facility designed to house larger interferometers and reduce seismic and environmental noise.

The original design concept for the ET followed a triangular configuration, made of three co-located detectors working together. Each detector includes two Michelson interferometers with $10\,\mathrm{km}$ long arms. These interferometers operate in different temperature ranges, one optimized for high-frequency signals (ET-HF), and the other for low-frequency signals (ET-LF). The corresponding scheme is shown in Figure 1.1a.

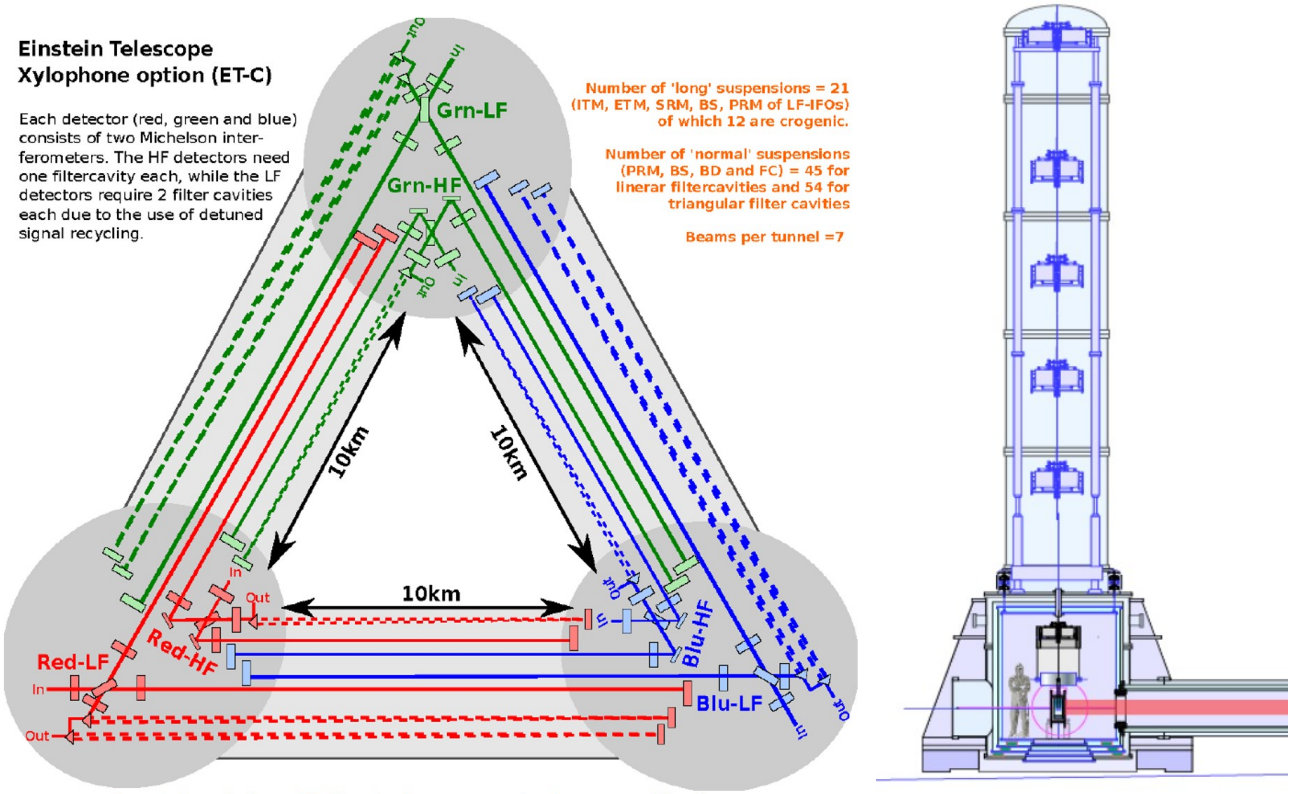

(a) General scheme of the Einstein telescope representing the geometry of the telescope[8].

(b) Mirror side view scheme of the seismic isolation system proposed for ET[9].

Figure 1.1: Einstein Telescope configuration schemes.

However, due to the limited flexibility of the triangular shape and potential noise correlations in collocated detectors, a new 2L configuration is now being considered. This design consists of two L-shaped interferometers, each with $15\,\mathrm{km}$ long arms, placed at different geographic sites.

The triangle design has several advantages. It enables a unique feature called the null stream, which cancels gravitational-wave signals to isolate noise. This helps with glitch rejection and calibration. It also benefits from co-location, simplifying infrastructure and operations. However, being in the same environment increases the risk of correlated noise, especially at low frequencies. The $60°$ arm angles also result in a slight sensitivity loss compared to a standard $90°$ interferometer[10].

On the other hand, the 2L configuration improves sensitivity by using longer arms and standard $90°$ geometry. Placing the detectors far apart improves sky localization and reduces correlated noise. It offers better parameter estimation, especially for cosmological measurements like distance. Its main drawbacks include higher costs, more complex coordination between sites, and the lack of a null stream for noise diagnostics[10].

Therefore, the choice between the triangular and 2L configurations is a balance between stability and measurement accuracy. Each has its own strengths for detecting signals, reducing noise, and finding where the signals come from. For these reasons, the final configuration is still under discussion and has not yet been decided[10].

The ET-HF will operate around room temperature, $290\,\mathrm{K}$, and will use a very powerful laser. In contrast, ET-LF will work at very low temperatures, around $10\,\mathrm{K}$-$20\,\mathrm{K}$, using cryogenic mirrors made of silicon[9]. This is important because thermal noise becomes dominant at low frequencies, and cooling the mirrors drastically reduces this noise. In addition, to isolate the mirror from seismic ground motion, the main optics are suspended to a complex mechanic tower, similar to a longer Virgo-style Superattenuator, as it can be seen in Figure 1.1b[9].

Such dual-frequency detection will allow the Einstein Telescope to observe a wide range of astrophysical sources, from mergers of black holes and neutron stars to signals from the early universe that are invisible today. This configuration is new and requires advanced technologies, especially for ET-LF.

To prepare and validate the technologies necessary for these future instruments, several prototypes and test facilities are being constructed around the world.

ETpathfinder, in Maastricht, is one of them. Actually, ETpathfinder is a laboratory of cryogenic research and development. It tests cryogenic systems, new suspensions, and other components planned for the Einstein Telescope and has similarities in its infrastructure with the one used for KAGRA and LIGO Voyager [11]. However, it uses a different strategy for the active cooling. In fact, ETpathfinder uses sorption-based Joule-Thomson coolers, which are almost vibration-free because they do not have moving parts. The cryostat is made up of four thermal shields with LN_2, Ne, and He shields, and a cascade of three cooler stages using Ne, He and H_2 combined with aluminum heat links [12].

Another prototype that studies an innovative radiative cooling method to reach $20\,\mathrm{K}$ at mirror level, starting from ambient temperature $290\,\mathrm{K}$, is E-TEST. It is an innovative prototype as it applies a unique radiative method to cool the payloads. This prototype is of primary interest in this project and will be described in detail in the following sections.

1.2 E-TEST current prototype

E-TEST stands for Einstein Telescope Euregio-Meuse-Rhine Site and Technology. This project was founded by the European program Interreg Euregio Meuse-Rhine. It started in 2020, ending in 2023. It has been developed in the scope of the Einstein Telescope project, presented in the previous section, and serves a twofold purpose. On one hand, it aims at creating an eco-friendly and non-invasive method for imaging geological conditions, laying the groundwork for the future development of an underground observatory in the Euregio-Meuse-Rhine (EMR) region. On the other hand, which is the main focus of this work, it addresses the need to cool down a suspended mirror to cryogenic temperatures while mechanically decoupling it as much as possible. To do so, a prototype that applies the concept of radiative contactless cryogenic heat exchanger, called E-TEST, has been developed at the Centre Spatial de Liège (CSL), which benefits from a strong expertise in cryogenic space instruments. Another reason for testing this prototype in this place is that the most promising locations for the ET project are the border area of the Netherlands, Belgium, and Germany [13][8].

The key methods currently considered to cool the optics of ET rely on conduction through thin flexible wires made of high purity aluminum. However, despite their flexibility, this method still introduces unwanted vibrations due to mechanical coupling and thermal noise. This is why the

concept of a fully radiative heat exchanger has been proposed and tested with E- TEST, to eliminate these mechanical couplings and reduce vibration transmission to the mirror.

The main idea behind the E-TEST cryostat is to cool the payload at $20\,\mathrm{K}$ using radiative heat transfer. The best of KAGRA and LIGO Voyager is used to create an innovative cryostat more adapted to the needs of the ET-LF. Indeed, while KAGRA introduces vibration through conduction and LIGO Voyager reaches only a temperature of $123\,\mathrm{K}$, E-TEST aims at reaching a cryogenic temperature of $20\,\mathrm{K}$ without conduction heat transfer links assembled to the payload. Therefore, to radiatively cool the payload that is composed of a silicon mirror of $100\,\mathrm{kg}$ $450\,\mathrm{mm}$ diameter and its supporting cold platform, a radiative heat exchanger (RHX) has been created. The complete prototype is described below based on a scheme of its front view which is shown in Figure 1.2.

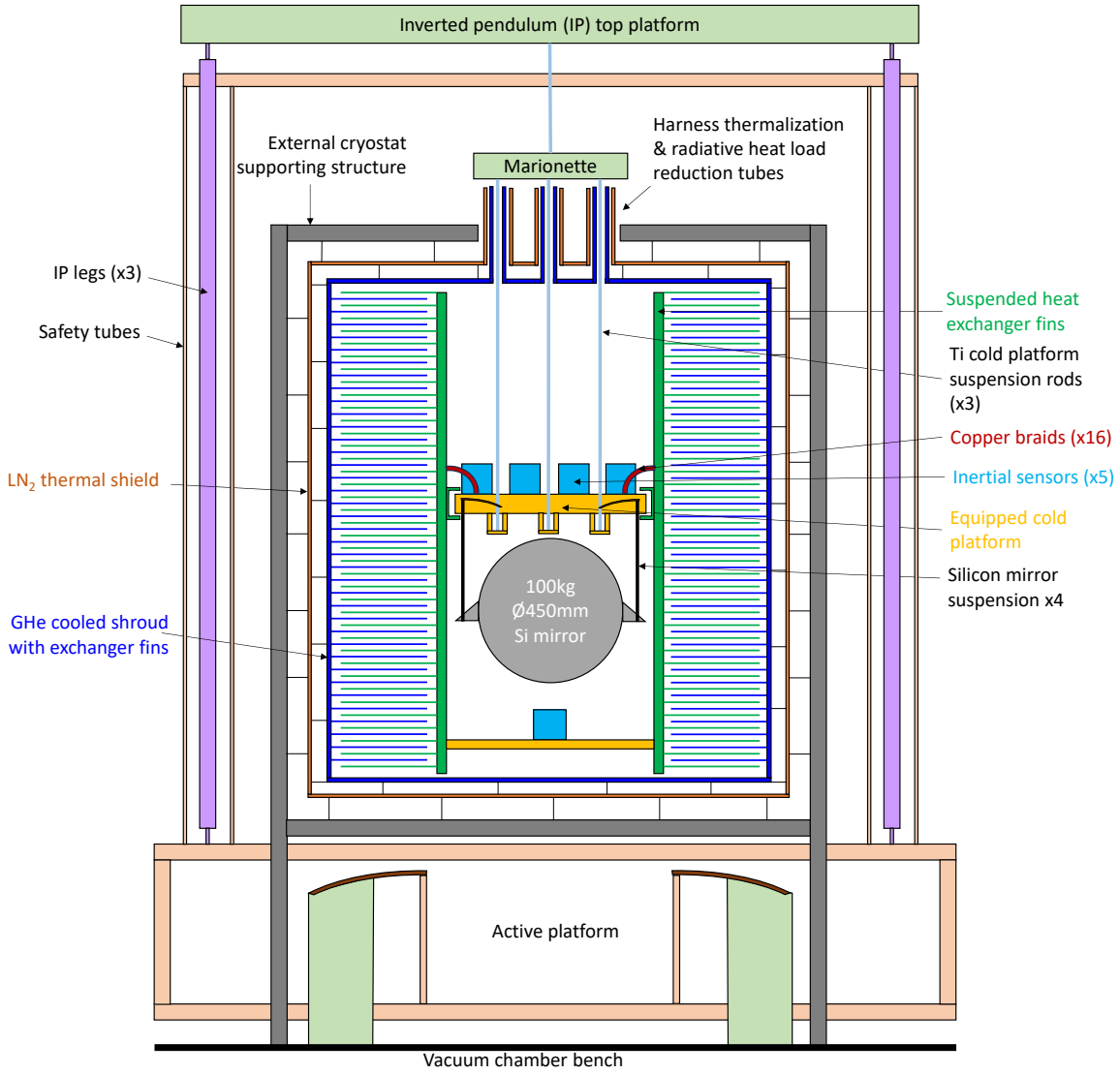

Figure 1.2: Scheme of the E-TEST cryostat initial architecture (front view)[13].

The outer shell of E-TEST that can be seen in Figure 1.2, is the mechanical structure designed to isolate the mirror from external vibrations. This structure is composed of an active platform, on which the inverted pendulum (IP) is mounted. This IP is itself composed of three legs, shown in purple, that holds the top platform, shown in green. Suspended to this top platform through a titanium rod, the marionette, shown also in green, has actuators to correct the position of the mirror. In fact, the mirror is suspended with silicon fibers on the cold platform, shown in yellow,

which is itself suspended to the marionette through titanium rods. On top of the cold platform are placed inertial sensors to determine whether a repositioning of the mirror is needed.

Surrounding the mirror and the cold platform, the RHX is made up of two complementary parts, the internal heat exchanger (IRHX) shown in green in the prototype scheme and the external heat exchanger (ERHX), shown in blue. Each of these elements has 140 horizontal fins. All of the fins have a rectangular shape, but two different sizes are used to enable easy fixation to rectangular structures. The top views of the IRHX and ERHX are presented in Figure 1.3. The short fins are shown in yellow, while the longer fins are shown in purple with the reinforcement fork highlighted with darker colors. The structures on which the fins are mounted are displayed in black.

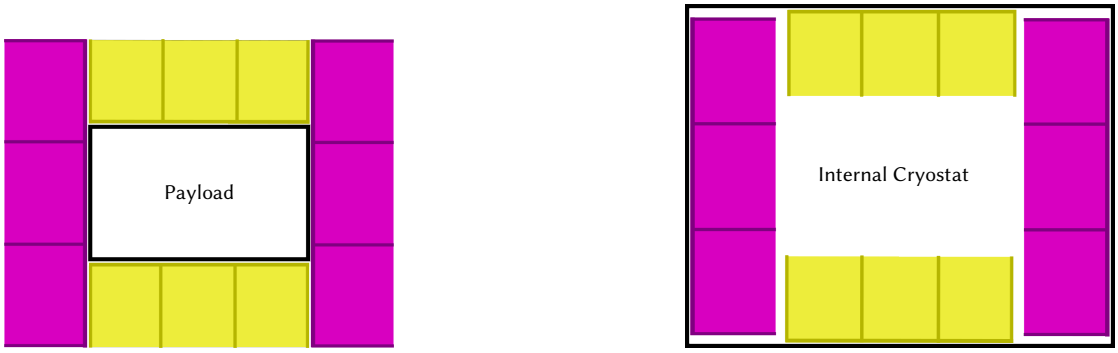

(a) Internal heat exchanger fins configuration.

(b) External heat exchanger fins configuration.

Figure 1.3: Top views of the radiative heat exchanger fins configurations.

The inner frame of the IRHX, displayed in black Figure 1.3a, is directly attached to the cold platform. The outer frame of ERHX, shown in Figure 1.3b, is mounted on actively cooled panels. These panels are fed with gaseous helium (GHe), at $15\,\mathrm{K}$, from the CSL closed-loop helium refrigerator and define the first layer of an external thermal isolation system. Surrounding this RHX is another thermal shield, cooled at $80\,\mathrm{K}$ with liquid nitrogen (LN_2) and shown in brown in Figure 1.2. The last layer of this thermal insulation system is the main support that is at ambient temperature. All the layers of this thermal insulation system are rigidly attached to each other and separated by Multi-Layer Insulation (MLI). This MLI is used to reduce the heat load that could reach the payload from the external environment. It is important to note that this choice of insulation material is made for E-TEST as water contamination is not a problem for the prototype but could not be used in the conditions of the ET-LF

The current E-TEST prototype, resulting from the scheme and characteristics presented above is shown in Figure 1.4. On the left, in Figure 1.4a is shown the E-TEST prototype during its assembly with three of the four sides of the RHX already mounted. The marionette and top platform, as well as the inverted pendulums and the active platform can also be seen. On the right, in Figure 1.4b, a zoom in on the intertwined heat exchanger fins is made. In this figure, the fins, initially gray since they are made in aluminum (Al1050A), appear black because of the paint with which they are coated to increase their emissivity.

1.2.1 Assembly process

As described in the previous section, the E-TEST prototype is a complex system incorporating a cryocooling system housed within a vibration isolation structure. The following section provides a brief overview of the assembly process for this interconnected structure, which is illustrated in Figure 1.5.

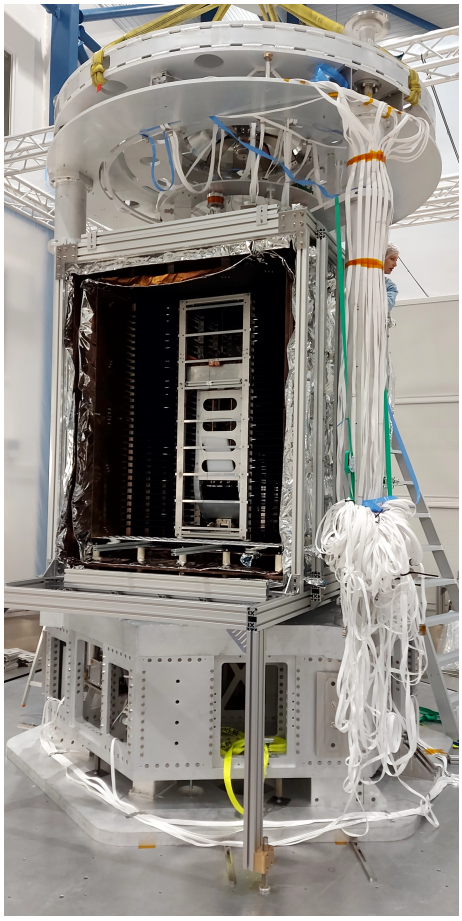

(a) E-TEST during the assembly.

(b) Zoom in on the heat exchanger fins.

Figure 1.4: Pictures of the E-TEST prototype.

Firstly, the fins, fin frames, and inner frame are cleaned and assembled. These are then integrated into the inner cryostat structure, which also includes the cold platform that holds the mirror. Note that, as it can be seen in Figure 1.5a, this assembly is made inside the intermediate frame and above the bottom thermal shield that is already assembled on top of the bottom frame. The intermediate and bottom frames are shown in black in Figure 1.5a.

Next, the inverted pendulum is temporarily installed to adjust the mirror position. In fact, the inner cryostat is suspended and a laser tracker is used to measure and balance the cryostat to achieve a symmetric and stable suspension. This is presented in Figure 1.5b.

Once the system is balanced, the inverted pendulum structure is disassembled to clear the space needed to assemble the outer cryostat. The ERHX sides are already attached to the thermal layers, including the GHe and LN_2 thermal panels, with the MLI positioned in between. These assemblies are then inserted straight in, allowing the ERHX fins to intertwined those of the IRHX while strictly avoiding any contact between them. Once the ERHX is in place, the thermal layers are connected. The resulting assembly is illustrated in Figure 1.5c.

After the outer cryostat is fully enclosed, the inverted pendulum is reinstalled permanently. Then, one side of the inner cryostat, specifically the side not obstructed by the pendulum legs, is temporarily reopened. This allows the reconnection of the cryostat suspension wires and the routing of cables through the top shroud. Finally, the cryostat is completely closed and the system undergoes final alignment and verification steps in preparation for operation[14]. This final state of the prototype is modeled in Figure 1.5d.

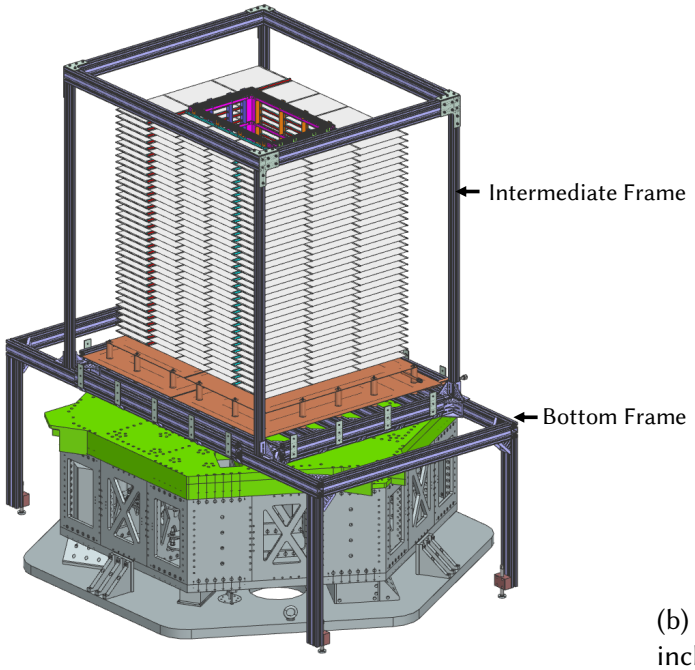

(a) Assembly of the inner cryostat.

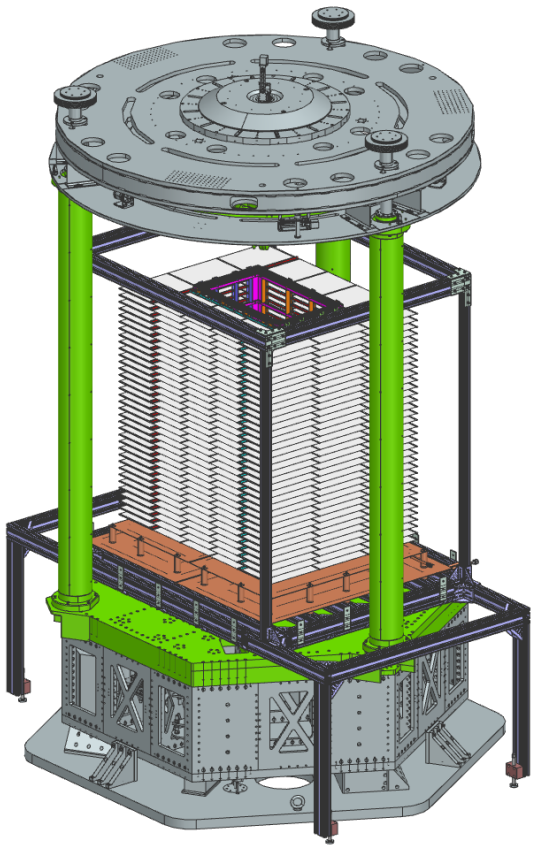

(b) Suspension and adjustment of the mirror position, included in the inner structure, with the inverted pendulum structure.

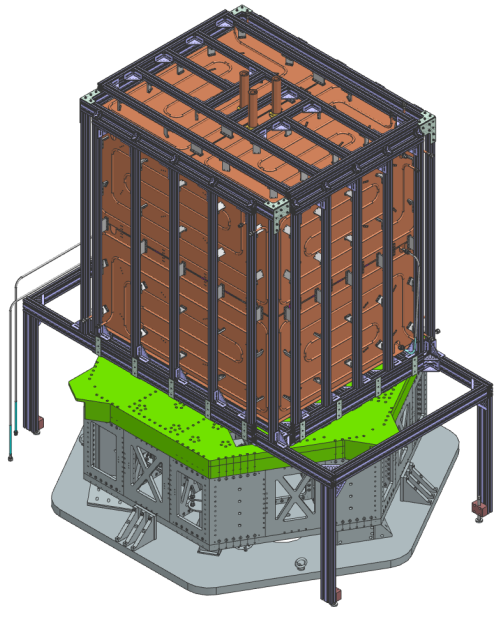

(c) Assembly of the outer cryostat without the inversted pendulum structure.

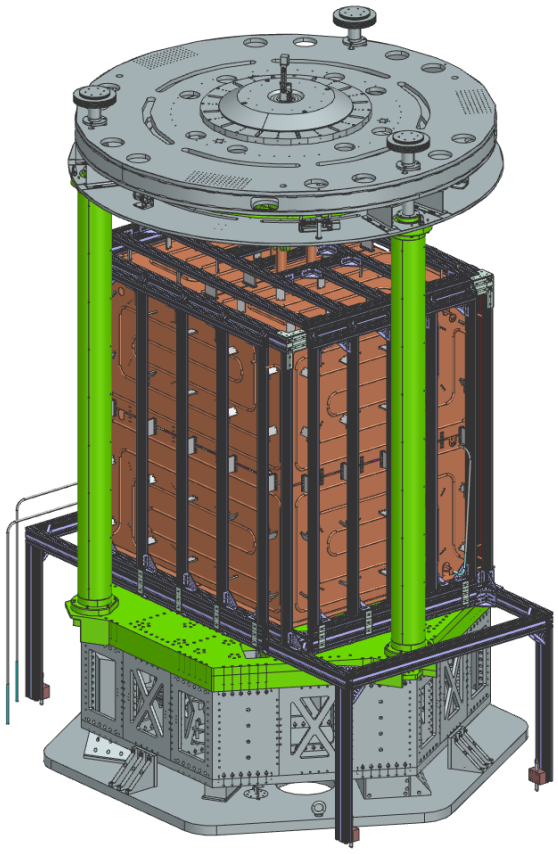

(d) Final assembly and adjustment of the cryostat with the inverted pendulum structure.

Figure 1.5: NX modelisation of the main E-TEST prototype assembly steps.

1.3 ET-LF cryostat geometry

First and foremost, it is important to note that no ET-LF cryostat currently exists. Nevertheless, the subject has been studied for a long time, and some assumptions about the future dimensions and geometries have already been made. This section aims to present the ET-LF design considered and used in this paper. A simplified drawing, inspired by the reference papers [15] and [16], is presented in Figure 1.6.

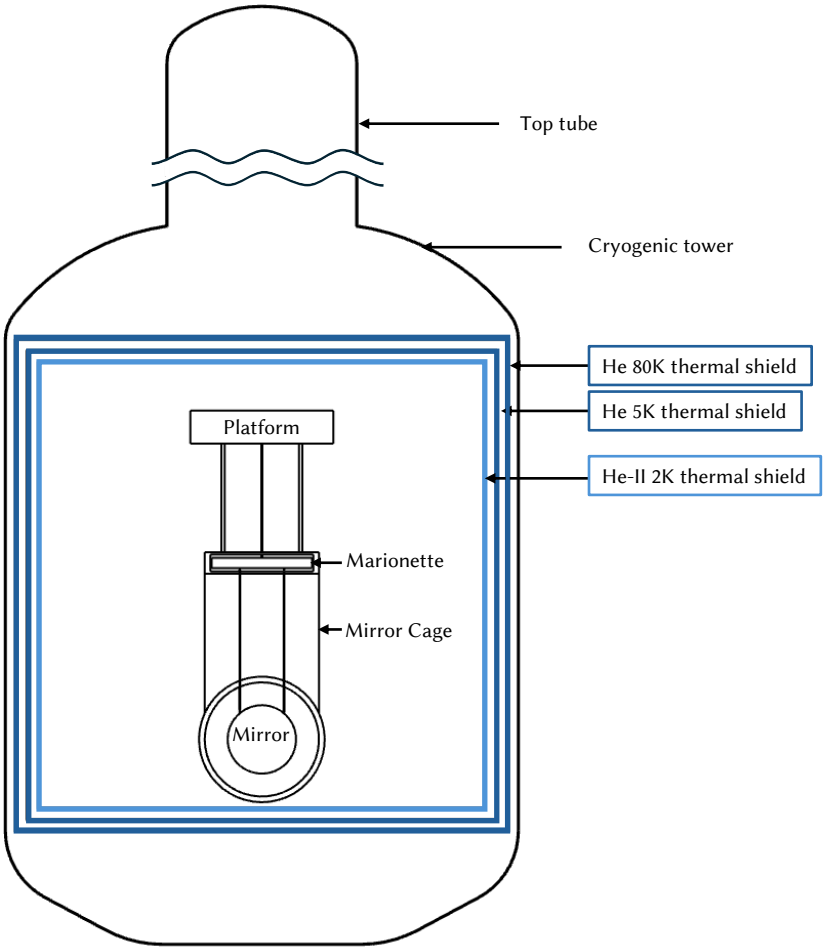

Figure 1.6: Draft of the Einstein Telescope LF cryostat.

The cryostat is isolated from the external environment by the ET-LF cryogenic tower, which has a cylindrical shape topped by a vertical tube. This upper tube contains, notably, the entire suspension system, which is designed to ensure optimal vibration isolation. In reality, the tube is much longer than depicted here, but it is of limited relevance to this study, as the focus lies on the cryostat itself and its boundaries. For this reason, it is not shown to scale and is presented without details.

Inside this physical boundary, three thermal shields are arranged successively. Each surface of each thermal layer is separated from the others by at least $10\,\mathrm{cm}$, ensuring that there is no physical contact between them. These insulation layers are actively cooled and protect the payload from the external heat rate. The outer thermal shields are field with single-phase helium flow at $80\,\mathrm{K}$ and $5\,\mathrm{K}$. The innermost thermal shield, located closer to the mirror, is cooled with static He-II at $2\,\mathrm{K}$.

Unlike the E-TEST prototype configuration, the mirror in this setup weighs $200\,\mathrm{kg}$, has a diameter of $60\,\mathrm{cm}$, and is directly suspended from a marionette. The marionette is in turn suspended from a platform connected to the vibration isolation system inside the top tube. The mirror is enclosed in a mirror cage, which is also suspended from the same platform.

As previously mentioned, the main cooling strategy studied so far relies on conductive cooling, using a thermal link attached either to the platform or directly to the mirror.

The focus in this thesis is to explore an alternative radiative cooling concept for the mirror. In this approach, one set of fins would be attached to the innermost thermal shield, cooled to the same temperature, while another set of fins would be connected to an additional structure mounted on the mirror cage. This configuration allows the payload to be cooled by radiation rather than conduction.

1.4 Constraint differences between ET and E-TEST

Now that both the ET and E-TEST cryostat design have been presented, it can be noticed that even though the overall goal of the E-TEST project is to demonstrate the feasibility and efficiency of a fully radiative cryostat for future use in the Einstein Telescope project, the prototype developed within the project operates under different constraints than the future ET cryostat. This section presents the main differences between these two projects that impact the design of the cryostats.

Some of the specific constraints that apply to ET but not to E-TEST include the following:

- It must operate in an ultra-high vacuum $1 \times 10^{-14}\,\mathrm{Pa}$ to avoid condensation on the mirror surface.
- There must be enough space for technicians to walk around the mirror during assembly.
- Both the marionette and the platform are inside the cryostat and cooled, while only the platform is cooled in E-TEST.
- It has different design constraints related to allocated volume, optical apertures, total heat load, and mirror characteristics, which are presented in more detail below.

First, the available cryostat volume differs between the two prototypes, both in dimensions and in the shape of the limiting structures. These differences are illustrated in Figure 1.7. The inner volume-limiting components are shown in purple, while the outer boundaries of the cryostat space are highlighted in green.

In the ET-LF, the cryostat volume is constrained by cylindrical geometries, as shown in Figure 1.7b. The inner cryostat boundary is the platform from which the marionette and the mirror cage are suspended, presented in Figure 1.6. This set of elements is shown in purple in Figure 1.7b. The more constraining element is the cylindrical platform that can be delimited by defining a radius, $r_{1,ET}$. In addition, the cryostat external volume limit is the thermal shield at $5\,\mathrm{K}$ that is also cylindrical. The latter is shown in green. Note that the innermost thermal shield, at $2\,\mathrm{K}$, is not considered as the volume limit as it supports the fins and thus could have different size depending on what is required, while the size of the intermediate thermal layer is assumed to be fixed. Nevertheless, in the limiting radius $r_{2,ETEST}$ and height, h_{ETEST}, a margin of $10\,\mathrm{cm}$ and $20\,\mathrm{cm}$ respectively must be subtract to ensure that there is no contact as for the other thermal layers. Therefore, all the cryostat size limits can be expressed with limiting radii and height.

In contrast, in the current E-TEST design, the limiting elements for the cryostat volume are non cylindrical. The inner limiting structure is the mirror cage, surrounding the rectangular cold platform. In addition, the external size and shape of the cryostat is limited by the positions of the three IP legs, leaving open spaces between them. The thermal shields in this case are not predefined and could potentially adopt various shapes. Therefore, to facilitate comparison with ET cryostat limiting sizes, the equivalent limiting radii have been defined and are presented in Table 1.1. The inner radius, $r_{1,ETEST}$, approximates half the diagonal of the rectangular cold platform, as seen from the top view. The outer radius is the distance from the mirror center to the nearest IP leg.

However, it is important to note that the limiting value, $r_{2,ETEST}$, presented in Table 1.1, is the corresponding measurement reduced by $20\,\mathrm{cm}$, to account for the space taken by the two thermal insulation layers. The limiting height of the E-TEST cryostat is defined by the distance between the bottom of the marionette and the top of the active platform, also highlighted in green. Similarly to the definition of the outer limiting radius, the height value h_{ETEST} listed in Table 1.1 is reduced by $40\,\mathrm{cm}$ to account for the space required by the thermal insulation layers located at the top and bottom of the cryostat. It is important to note that the top tubes are mounted above the main cryostat structure. These tubes, which surround suspension cables, minimize the heat flux from the external environment, as it will be discussed later in this document. In the ET configuration, these tubes can extend through the large top beam. On the contrary, in the E-TEST configuration, these tubes must be considered in the overall dimensions of the cryostat. Therefore, the tube height that extends beyond the main structure must be included in the total height of the cryostat and this total value must be lower than h_{ETEST}.

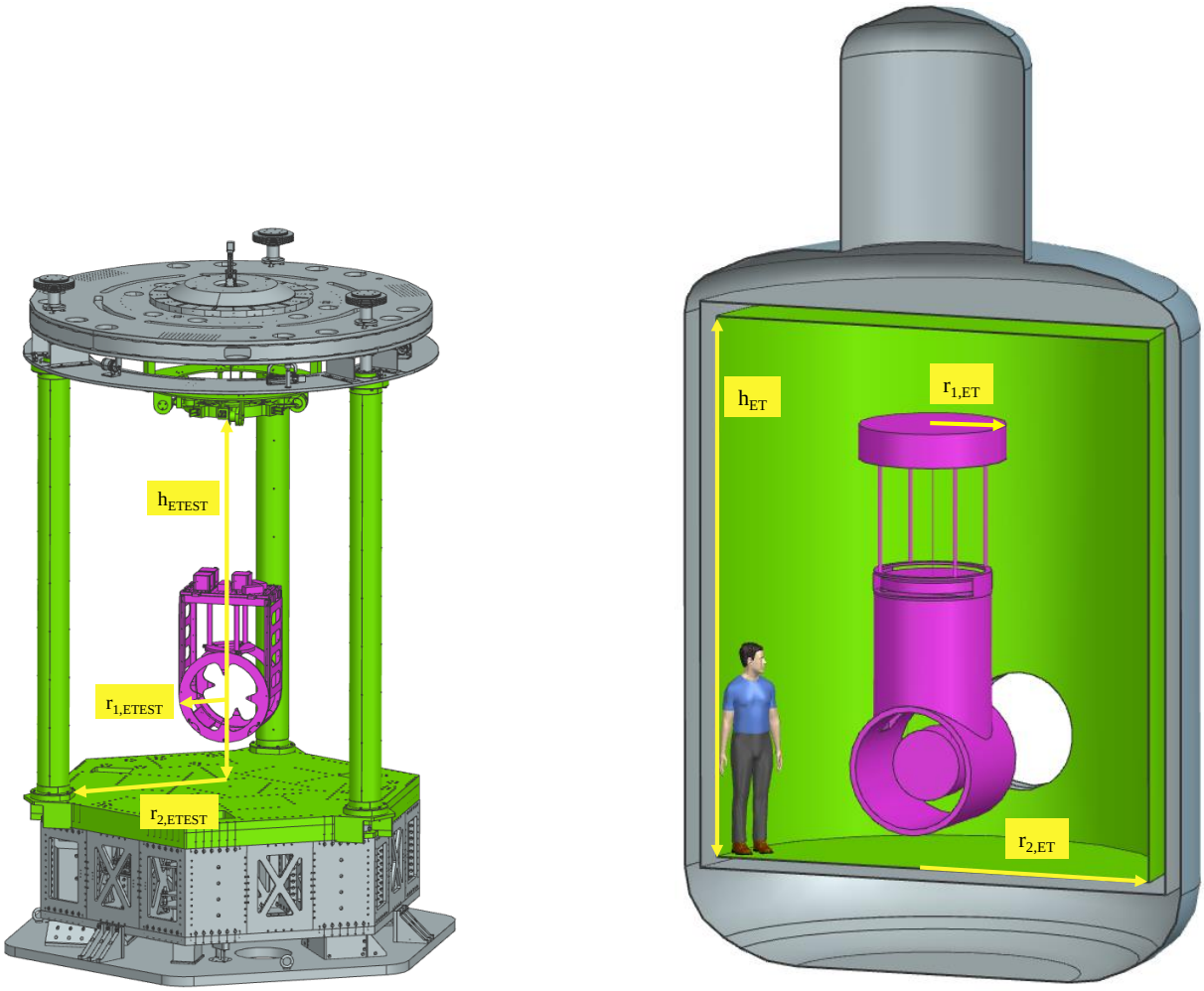

(a) Cryostat volume limits for E-TEST.

(b) Cryostat volume limits for ET.

Figure 1.7: Cryostat volume limits for both prototypes with the inner limiting objects highlighted in purple and the outer limiting objects highlighted in green.

In addition, the mirror size and weight, the apertures, and the heat load to be extracted in E-TEST differ from those in the ET prototype.

For optical apertures, the ET interferometer requires large apertures in both the front and back of the mirror. This does not lead to a significant radiative heat load, thanks to the cryogenic stray light baffle tubes installed on both sides of the mirror. These baffles not only reduce thermal noise but

length [m]	E-TEST	ET
h	2.35	2.6
r_1	0.34	0.6
r_2	0.85	1.95

Table 1.1: Limiting values of the lengths presented in Figure 1.7

also limit optical noise. Similarly, the large aperture at the top of the ET cryostat, needed for the suspension system, is not critical. The associated heat load is limited by the top tower that houses the vibration isolation system. In contrast, E-TEST cannot accommodate large thermal baffles due to space limitation in the vacuum chamber. Therefore, only three small apertures are used in front of the mirror and three at the top of the cryostat.

The heat load to be extracted from the E-TEST cryostat will be discussed in detail later. However, an initial estimate of $250\,\mathrm{mW}$ has been published in [13]. For ET, the expected heat load includes contributions from mirror bulk and coating absorption, thermal radiation, and an additional margin. The total heat budget is estimated at $500\,\mathrm{mW}$ [17].

A summary of these key parameters for both ET and E-TEST is provided in Tab. 1.2.

Parameter	ET	E-Test
Mirror diameter [m]	0.6	0.45
Mirror weight [kg]	200	100
Apertures:		
- number	3	6
- diameter [m]	1	0.03
Heat load to extract [mW]	500	250

Table 1.2: Comparison of ET and E-TEST parameters

Nevertheless, if the E-TEST prototype yields satisfying results, the main principle could be adapted to the conditions of the ET project, providing an innovative cryogenic cooling method, which is discussed in later parts of this document.

In short, E-TEST plays an important role in preparing the Einstein Telescope, even though it works in a different environment. It helps to test new ideas for cryogenic cooling that could improve the sensitivity and allow ET to observe signals from the early universe.

1.5 Motivation and objectives

The first version of the E-TEST prototype has been made in a duration of only three years as mentioned earlier in this introduction. This relatively short period of time led to a prototype that produced fairly satisfactory results but nevertheless left behind a certain number of uncertainties and issues. Moreover, building the prototype helped to highlight issues that had not been noticed during its theoretical development. Therefore, this thesis aims at studying more deeply the current prototype and suggesting some enhancements, which could help to improve the thermal performance of the prototype and make its assembly easier. In addition, it also aims at studying the feasibility of adapting the concepts developed for E-TEST to the more demanding constraints of the ET-LF.

1.6 Layout

In order to meet the objectives presented in the previous section, this paper is organized as follows.

To begin, Chapter 2 recalls the theoretical background necessary to evaluate the thermal performance of the cryostat. It reviews the fundamental principles of heat transfer, focusing on conduction, radiation, and transient thermal behavior. These concepts are essential to understand the thermal analyses used in the thesis.

Next, Chapter 3 focuses on the current E-TEST prototype. It first studies the vibrational behavior of a single cryostat fin via experimental testing. Then, simplified models, a mass-spring system and a FEM model, are developed to replicate the vibrational behavior of the fin. The goal is to create in the future a sufficiently accurate model that can be extended to the full cryostat to gets insights into its vibrational behavior. After that, a thermal analysis of the E-TEST cryostat is lead using a simplified node-based model and the results are compared to the test measurements. This is done to develop thermal analyses that are used later in the document to determine the thermal performance of the new cryostats and to compare them to the current one.

Following this, Chapter 4 explores possible improvements to the E-TEST prototype. On the low-complexity side, it suggests increasing the emissivity of the interior surfaces of the top tubes to enhance thermal performance, reduce the risk of cable bending, and facilitate assembly. An alternative assembly method is also presented to simplify the overall process. On the high-complexity side, the chapter investigates complete redesigns of the radiative heat exchanger, as well as different fin shapes, with the goal of optimizing thermal performance and assembly process.

Based on these results, Chapter 5 evaluates whether the RHX concept developed for E-TEST can be adapted to the geometric and thermal constraints of the Einstein Telescope. Several RHX configurations are analyzed to assess their feasibility and efficiency.

Then, Chapter 6 presents a detailed thermal analysis of the ET cryostat using a simplified thermal node model. It aims to confirm whether the RHX design proposed in the previous chapter can meet the performance requirements of ET-LF, particularly achieving a mirror temperature below 20 K using only radiation between the payload and the actively cooled thermal shield.

Finally, Chapter 7 concludes the work by summarizing the main findings and suggesting possible future developments based on the results obtained in this study.

CHAPTER 2

HEAT TRANSFER THEORY

The E-TEST and ET-LF projects are connected by the common goal of cooling a mirror to cryogenic temperatures. This thesis focus on assessing the feasibility of using a RHX for this purpose. To do so, a thorough understanding of heat transfer is essential. This chapter revisits key aspects of heat transfer theory that are later used to analyze the thermal behavior of the E-TEST and ET cryostats.

2.1 Heat transfer via conduction

The general equation of conduction heat transfer can be written as

$$\dot{Q}_{c,ij} = GL_{ij}(T_i - T_j) = k_{ij}A_{ij}\frac{T_i - T_j}{L_{ij}}, \tag{2.1}$$

With k_{ij}, the thermal conductivity ($\mathrm{W\,m^{-1}\,K^{-1}}$), that is a property of the conductor material, A_{ij} its cross-sectional area ($\mathrm{m^2}$), T_i and T_j the temperatures of this conductor at the points of interest (K), and L_{ij}, the length of the conductor between the these two points (m)[18].

2.2 Heat transfer via radiation

Similarly, the general equation of radiation heat transfer can be written as

$$\dot{Q}_{r,ij} = GR_{ij}\sigma(T_i^4 - T_j^4), \tag{2.2}$$

Where, $\sigma = 5.67 \times 10^{-8}\,\mathrm{W\,m^{-2}\,K^{-4}}$ is the Stefan-Boltzmann constant, GR the effective radiative conductance ($\mathrm{m^2}$), and T_i and T_j the temperatures of the two surfaces (K). The effective radiative conductance includes the emissivity and geometry, via the radiative heat exchange factor including the view factor and area[18].

2.2.1 Radiative heat transfer between the fins and corresponding radiative transfer area

This subsection aims at presenting the theory behind the radiative heat transfer formula used in this thesis to evaluate the heat exchanged between the fins of the cryostat. It also presents the relevant outcomes of a modified expression of this formula to highlight the impacts of the surface parameters on the radiative transfer area needed.

To begin, the net radiation exchange between opaque, diffuse, gray surfaces in an enclosure is expressed as follow [18],

$$\dot{Q}_{r,12} = \frac{\sigma(T_1^4 - T_2^4)}{\frac{1-\varepsilon_1}{\varepsilon_1 A_1} + \frac{1}{A_1 F_{12}} + \frac{1-\varepsilon_2}{\varepsilon_2 A_2}}. \tag{2.3}$$

In this study, the fins used in the IRHX and ERHX have the same characteristics. They have the same dimensions and their surfaces have the same emissivity. Therefore, $A_1 = A_2 = A_{IRHX} = A_{ERHX}$ and $\varepsilon_1 = \varepsilon_2 = \varepsilon_{RHX}$. Moreover, because the fins are intertwining and close to each other, it is assumed that the view factor between the surfaces is equal to one, $F_{12} = 1$.

Applying these assumptions to Equation 2.3 leads to the simplified expressions

$$\dot{Q}_{parasit} = \sigma A_{IRHX} \frac{\varepsilon_{RHX}}{(2 - \varepsilon_{RHX})}(T_{IRHX}^4 - T_{ERHX}^4), \tag{2.4}$$

$$\Leftrightarrow A_{IRHX} = \dot{Q}_{parasit} \frac{(2 - \varepsilon_{RHX})}{\varepsilon_{RHX}\sigma} \frac{1}{T_{IRHX}^4 - T_{ERHX}^4}. \tag{2.5}$$

Equation 2.5 shows that the relation between the transfer area, A_{IRHX}, noted A_1 in Equation 2.3, and the heat to be evacuated from the payload, $\dot{Q}_{parasit}$, is linear. Therefore, a multiplication of the heat load induces a multiplication of the radiative surface area. In contrast, the relations between the emissivity, the temperatures, and the radiative surface area are not so simple. To illustrate this, the evolutions of the transfer area needed to reach an increasing IRHX temperature for different emissivities, evaluated at four different ERHX temperatures, considering a constant heat load, $\dot{Q}_{parasit} = 250\,\mathrm{mW}$, are presented in Figure 2.1.

As shown in the graphs, an increase in T_{IRHX} leads to a systematic decrease in the required radiative transfer area, with steepest curves at higher ERHX temperatures for lower IRHX temperatures. Moreover, as the ERHX temperature increases from $10\,\mathrm{K}$ to $15\,\mathrm{K}$, the required area for a given IRHX temperature rises sharply, and the curves steepen considerably, particularly at lower IRHX temperatures. This is because the temperature gradient between the ERHX and the IRHX is smaller and thus more sensitive to slight variations.

Additionally, the influence of the emissivity is clearly highlighted across all subfigures. For a given temperature configuration, the required area significantly decreases with increasing emissivity. It can also be noted that the gap between the curves for different emissivity decreases with increasing emissivity.

These results emphasize the necessity of maintaining both high emissivity and a sufficiently low ERHX temperature to minimize the required radiative exchange surface, especially when low cryogenic IRHX temperatures are researched.

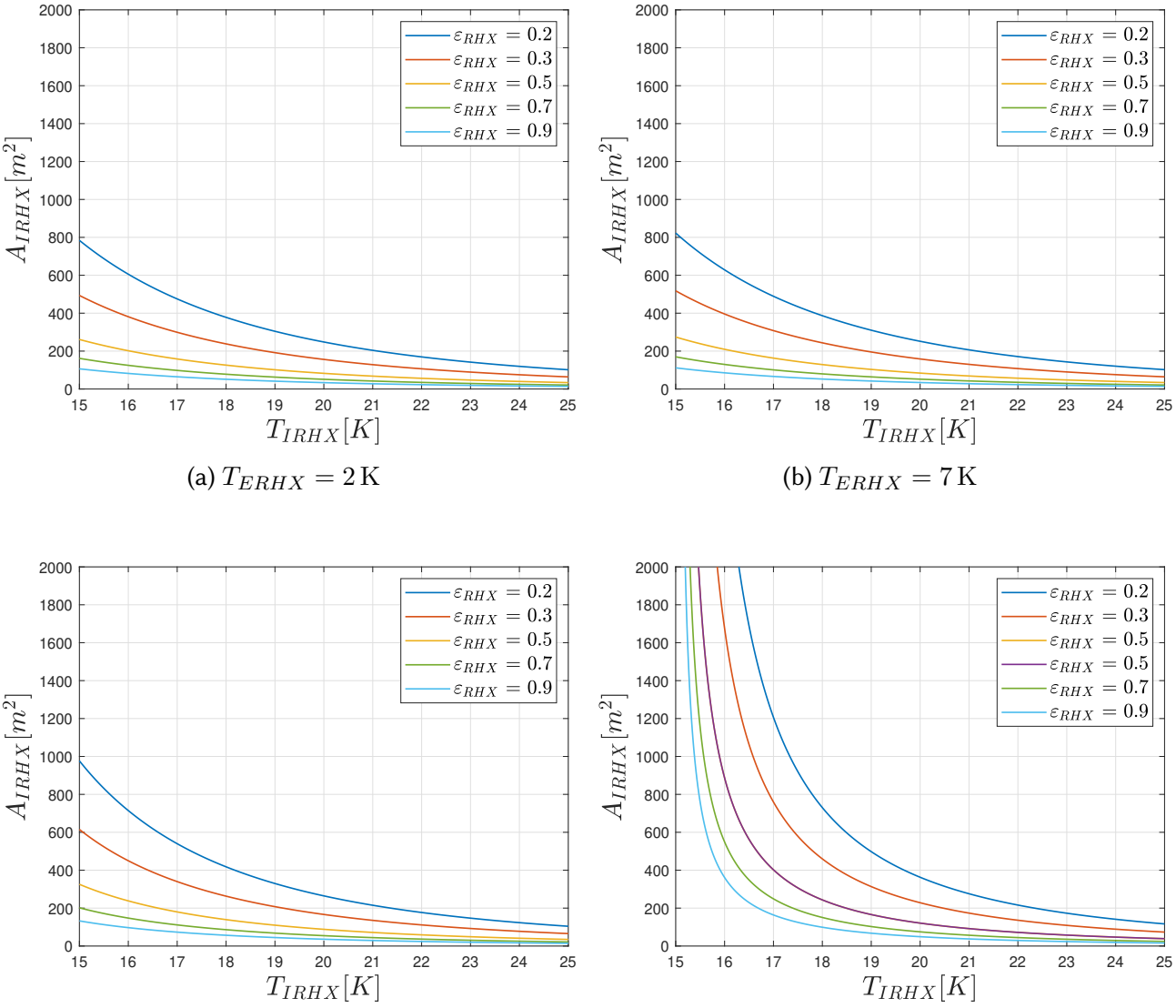

(a) $T_{ERHX} = 2\,\mathrm{K}$

(b) $T_{ERHX} = 7\,\mathrm{K}$

(c) $T_{ERHX} = 10\,\mathrm{K}$

(d) $T_{ERHX} = 15\,\mathrm{K}$

Figure 2.1: Evolution of the transfer area needed to reach an increasing IRHX temperature (T_{IRHX}) for different fin emissivities (ϵ_{RHX}) evaluated at four different ERHX temperatures (T_{ERHX}) considering a constant heat load $\dot{Q}_{parasit} = 0.25\,\mathrm{W}$.

2.3 Gebhart's Method

The main idea behind Gebhart's method is to obtain Gray Body Factors that can further be used to express radiative conductance from view factors. Recall that the view factor, F_{ij}, quantifies the fraction of energy emitted from one surface that arrives directly to the other surface, while the gray body factor, B_{ij}, quantifies the fraction of energy leaving one surface that is absorbed by the other through all possible paths, direct and indirect. It should be noted that this method uses the assumption of diffuse reflection on isothermal, uniformly irradiated gray surfaces[19][20].

To begin, the gray body factor or Gebhart factor between two surfaces i and j is expressed as,

$$B_{ij} = \frac{\text{Energy absorbed at } A_j \text{ emitted by } A_i}{\text{Total radiation emitted by } A_i}.$$

The general formula for N_s surfaces Equation 2.6 is

$$B_{ij} = \varepsilon_j F_{ij} + \sum_{k=1}^{N_s} \left((1 - \varepsilon_k) F_{ik} B_{kj} \right). \tag{2.6}$$

In addition, by conservation of energy,

$$\sum_{i=1}^{N_s} Bij = 1. \tag{2.7}$$

The view factors, F_{ij}, used in the previous equation possess two important properties, reciprocity and summation. The reciprocity relation, shown in Equation 2.8, states that the view factor from one surface to another, multiplied by the area of the emitting surface, is equal to the view factor in the reverse direction multiplied by the area of the receiving surface. The summation rule, presented in Equation 2.9, indicates that the sum of all view factors from a given surface to all surrounding surfaces is equal to 1[18].

$$A_i F_{ij} = A_j F_{ji}, \tag{2.8}$$

$$\text{and } \sum_j F_{ij} = 1. \tag{2.9}$$

The radiative conductance and thus, using Equation 3.35, the radiative exchange from a surface i to j can be written as

$$GR_{ij} = \varepsilon_i A_i B_{ij} \tag{2.10}$$

$$\dot{Q}_{r,ij} = \varepsilon_i A_i B_{ij} \sigma (T_i^4 - T_j^4) \tag{2.11}$$

2.3.1 Radiative heat transfer between the fins

Considering again the case of the radiation between the parallel fins, the assumption of a view factor of 1 between the surfaces can again be made. Therefore, the Equations 2.6 and 2.7 can be written as the system presented in Equation 2.12, leading to

$$\begin{cases} B_{12} = \varepsilon_2 + (1 - \varepsilon_2) B_{22} \\ B_{22} = 1 - B_{12}, \end{cases} \tag{2.12}$$

$$\Rightarrow B_{12} = \varepsilon_2 + (1 - \varepsilon_2)(1 - B_{12}) = \frac{1}{2 - \varepsilon_2}. \tag{2.13}$$

In addition, since the fins are the same, the surface emissivity is the same $\varepsilon_1 = \varepsilon_2 = \varepsilon_{RHX}$. Therefore the radiative conductance is

$$GR_{12} = \frac{\varepsilon_{RHX} A_{IRHX}}{2 - \varepsilon_{RHX}}. \tag{2.14}$$

Injected in Equation 3.35, it yields the same expression as the one presented in the previous section, that is, Equation 2.4.

2.4 Transient behavior of a thermal node in a lumped thermal network

Considering a thermal system, the thermal evolution of each of its elements with time can be approximated with an electrical network analogy, using isothermal nodes discretizationt. The temperature evolution at each node can be obtained applying the following theory.

Considering a thermal nodes model, the first law of thermodynamics states that for a control mass k,

$$\frac{dU_k}{dt} = \dot{Q}_{net,k}, \tag{2.15}$$

with $U_k = m_k c_{p,k} T_k$, the internal energy of the node, assuming constant specific heat capacity at constant pressure $c_{p,k}$ and mass m_k, and $Q_{net,k}$, the net heat input rate into the node k. Rearranging the terms in Equation 2.15, and dividing the net heat input rate in terms of convection, conduction, radiation within the system, and external contributions, Equation 2.16 is obtained. Then, neglecting the convection heat rate contribution and developing, radiative and conductive heat input rate contributions, as well as external heat rates, the expression in Equation 2.17 is obtained.

$$\frac{dT_k}{dt} = \frac{1}{m_k c_{p,k}} \dot{Q}_{net,k} = \frac{1}{m_k c_{p,k}} \left(\dot{Q}_{cond,k} + \dot{Q}_{conv,k} + \dot{Q}_{rad,k} + \dot{Q}_{ext,k} \right), \tag{2.16}$$

$$\Rightarrow \frac{dT_k}{dt} = \frac{1}{m_k c_{p,k}} \left(-\sum_i GL_{ki}(T_k - T_i) - \sum_j \sigma GR_{kj}(T_k^4 - T_j^4) + \dot{Q}_{ext,k} \right). \tag{2.17}$$

In Equation 2.17, GL_{ki} is the thermal conductance between node k and node i in W/K, GR_{kj} is the radiative exchange factor from node k to node j, in m^2, and σ is the Stefan-Boltzmann constant $\sigma = 5.67 \times 10^{-8} \mathrm{W\,m^{-2}\,K^{-4}}$.

Conclusion

This chapter has outlined the fundamental principles of heat transfer, conduction, radiation, and transient thermal behavior, useful for the thermal analysis of the E-TEST and ET-LF cryostat systems. Special emphasis was placed on radiative heat exchange between cryostat fins and the use of Gebhart's method to evaluate complex radiative interactions. These theoretical foundations will be applied in the following chapters to assess the feasibility and performance of RHX in achieving the desired cryogenic temperatures.

Part I

E-TEST

CHAPTER 3

STUDY OF THE CURRENT PROTOTYPE

During the development of the E-TEST, some aspects of the cryostat were not fully explored. To improve the current prototype, its thermal and vibrational behaviors must be better understood. This chapter analyzes the cryostat from both perspectives. First, the vibrational behavior of a single fin is examined. Then, the thermal behavior of the full cryostat is investigated.

3.1 Vibrational analysis of one single cryostat fin

This section focuses on the analysis of the vibrational behavior of a single cryostat fin. The objective is twofold. The first goal is to identify the natural frequencies of the fin in order to ensure they are sufficiently high to avoid resonance with the environment. The second goal is to develop a simplified model that can later be scaled up to represent the entire cryostat. This model will serve to analyze the overall vibrational behavior, estimate thermal noise, and assess whether it presents a critical concern.

The study is structured in several parts. It begins with a series of laboratory experiments to determine both the natural frequencies and the transfer function of the fin. Then, an equivalent mass-spring model is introduced to evaluate how accurately it can reproduce the observed vibrational behavior. Finally, a simplified FEM model is built, using NX software, and is also compared to the experimental results.

3.1.1 Experimental evaluation of the fin vibrational characteristics

The objective of the laboratory is to extract the transfer function and first natural frequencies of one of the long cryostat fins, which measures $1.11\,\mathrm{m}$ length and $0.3\,\mathrm{m}$ width. Transfer functions are obtained by measuring the displacement of some points of the fins in response to an applied force. The experiment was carried out multiple times, using different actuator instruments and changing the measurement parameters, to achieve the desired level of accuracy. This section presents the various laboratory tests conducted and highlights the most relevant results.

Hammer actuator vibrational laboratory

During the initial test campaign, a hammer, shown in Figure 3.1, was used to apply the input force. The force was applied at the same location of the fin for all measurements, identified as point

H in Figure 3.1a. The resulting vibrational response was measured at several locations using a laser vibrometer. These measurement points, numbered and highlighted in blue, are also shown in Figure 3.1a. As it can be seen in this figure, to enhance reflectivity and ensure accurate laser readings, reflective tape was applied at each measurement location.

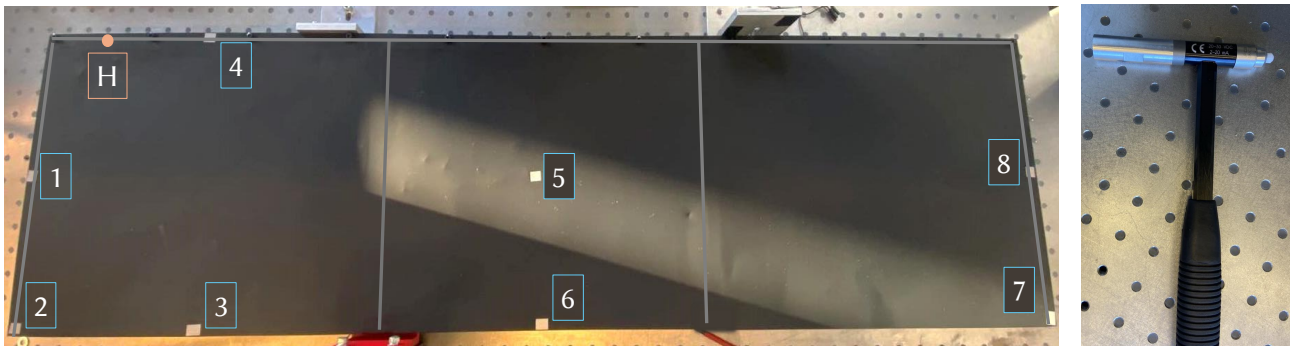

(a) Tested fin with reinforcement fork highlighted in gray, hammer actuation point shown in orange and the measurement point shown in blue.

(b) Hammer.

Figure 3.1: First experimental tests set up.

To improve the reliability of the results, each measurement was repeated multiple times. However, due to the manual nature of the hammer impacts, many of these measurements were not valid. In particular, some impacts were too strong, causing the response signal to exceed the voltage range of the measurement system (+/- $10\,\mathrm{V}$). This resulted in signal saturation, where the data no longer accurately represented the object motion.

Another common issue was the occurrence of double hits. These happened when the hammer bounced due to an uncontrolled strike, producing multiple impacts in a single attempt and thus invalidating the measurement.

To address these issues, the measurements taken at the same point were filtered to remove invalid data. The transfer function was then calculated for each valid measurement and averaged to reduce the influence of disturbances.

An example of this filtering process is shown in Figure 3.2, which presents data from measurement point 2 in Figure 3.1a. The plots on the left show the force and velocity signals at this point over the entire duration of the test, including multiple hammer impacts. As seen in Figure 3.2b, the first velocity signal is saturated, reaching $-10\,\mathrm{V}$. This measurement must therefore be discarded.

The result of the filtering is illustrated in Figures 3.2c and 3.2d. As expected, the first impact no longer appears in the processed data. Additionally, the signals are now segmented, showing the individual valid measurements instead of a continuous signal as in Figures 3.2a and 3.2b. Different colors are used to clearly distinguish the separated impacts.

Despite this filtering, the measurements still contained some inaccuracies, mainly due to slight residual double hits or inconsistencies in the impacts. For instance, in Figure 3.2d, the second impact seems valid at first glance. However, a closer look at the corresponding force signal reveals that it is actually composed of three small impacts rather than a single one.

As a result, the calculated transfer functions remained unclear. Figure 3.3a shows the transfer functions for each individual valid measurement at point 2, while Figure 3.3b presents the averaged transfer function. The peaks in these graphs are poorly defined, and the overall quality of the data is not sufficient for precise analysis. Therefore, a more reliable actuation method was required.

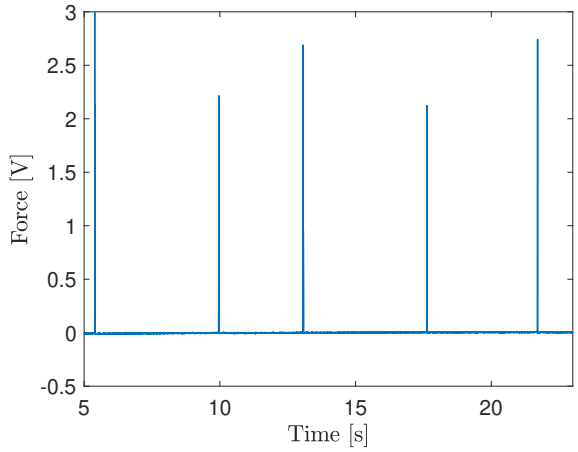

(a) Measured force signal during the entire laboratory test.

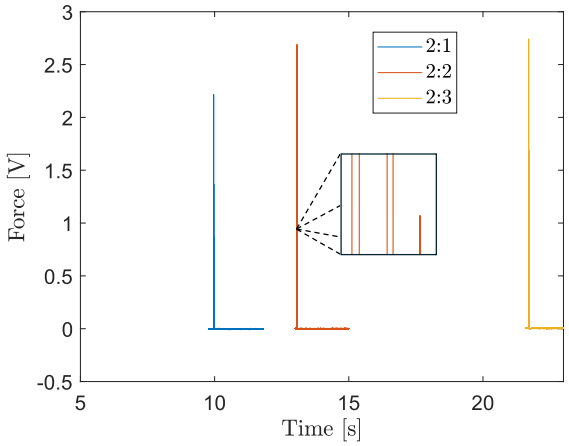

(b) Measured velocity signal during the entire laboratory test.

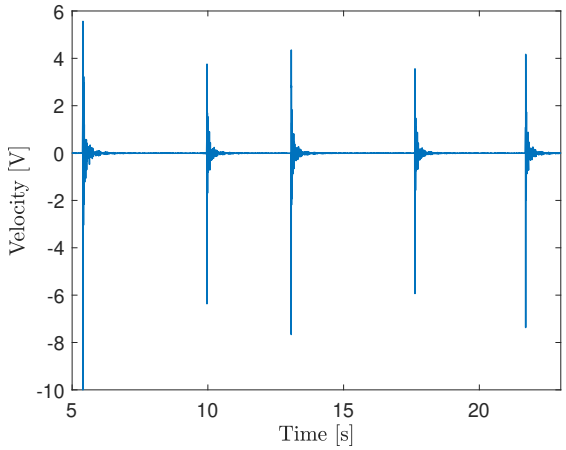

(c) Filtered and segmented force signal.

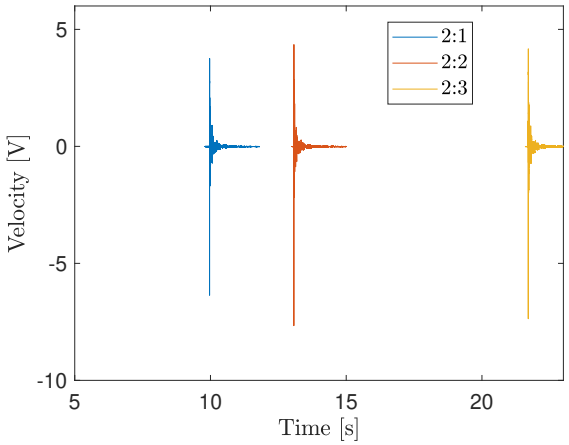

(d) Filtered and segmented velocity signal.

Figure 3.2: Input and output signals, before and after being filtered, of the measurement made at point 2.

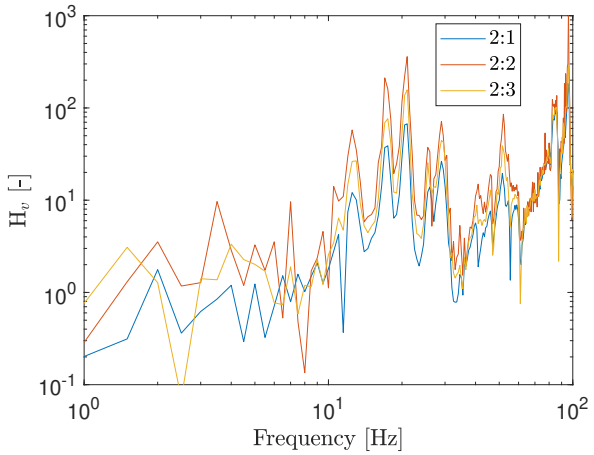

(a) Transfer functions of the several measurements.

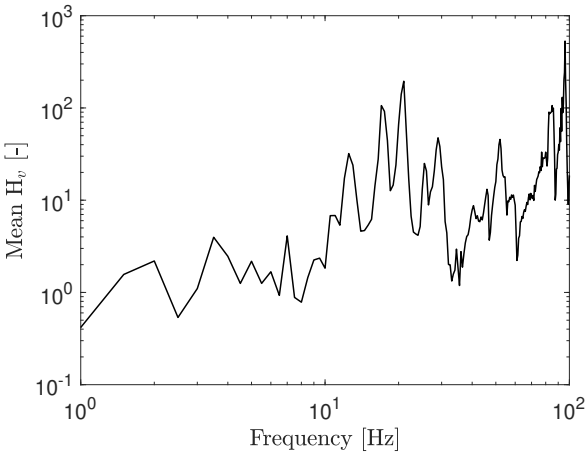

(b) Averaged transfer function.

Figure 3.3: Transfer functions resulting from the measurements made at point 2.

First laboratory with Voice Coil Actuator

To obtain a more accurate excitation signal, the hammer was replaced with a voice coil actuator, positioned at the second reinforcement of the fin, identified as VCA in Figure 3.4a. The vibrational response was again recorded with a laser vibrometer, using the same measurement points as in the previous test. The fin was excited using white noise over a duration of $50\,\mathrm{s}$ per measurement point.

(a) Tested fin with reinforcement fork highlighted in gray, Voice Coil actuator impact point shown in orange and the measurement point shown in blue.

(b) Voice coil actuator shown on the right with current injector at its left.

Figure 3.4: Second experimental tests set up.

The input signal is sent from a microlabbox in V. It is converted to a force through a current injector with a gain of $0.2\,\mathrm{A\,V^{-1}}$, followed by the actuator with a gain of $2.58\,\mathrm{N\,A^{-1}}$. Both instruments are shown in Figure 3.4b. The output signal, coming from the laser, is also in V. It is converted into velocity using a gain of $50\,\mathrm{mm\,s^{-1}\,V^{-1}}$. Thus, the actual physical quantities are obtained through the relations

$$F = F_{signal} \times 0.2 \times 2.58 \quad [\mathrm{N}], \tag{3.1}$$

$$V = V_{signal} \times 0.05 \quad [\mathrm{m/s}]. \tag{3.2}$$

The corresponding transfer function linking velocity and applied force is given by

$$H_v(\omega) = \frac{V(\omega)}{F(\omega)} \quad \left[\frac{\mathrm{m\,s^{-1}}}{\mathrm{N}}\right]. \tag{3.3}$$

However, the transfer function of interest relates the applied force to response displacement. In the frequency domain, the displacement is given by

$$X(\omega) = \int x(t) e^{-i\omega t}\, dt, \tag{3.4}$$

which implies that the velocity becomes

$$V(\omega) = \frac{dX}{dt} = -i\omega \cdot X(\omega), \tag{3.5}$$

with $\omega = 2\pi f$.

Therefore, the displacement based transfer function is expressed as

$$H_x(\omega) = \frac{X(\omega)}{F(\omega)} = \frac{H_v(\omega)}{-i\omega} \quad \left[\frac{\mathrm{m}}{\mathrm{N}}\right]. \tag{3.6}$$

Despite improved instrumentation, the results of this second test remained insufficiently precise. The short measurement duration and broadband excitation introduced noise and reduced resolution in the frequency response. Thus, longer and more targeted measurements were required.

Second laboratory with Voice Coil Actuator

In the third and final laboratory tests configuration, the voice coil actuator was placed at the same location as before, referred to as VCA point in Figure 3.5. However, the number of measurement points was reduced to three strategic locations. The first point, collocated with the actuator, served as a reference and is noted point C. The second measurement point, point S in Fig. 3.5, is located at the center of the second soft section near the tip of the fin. The third, point R, was placed at another reinforcement point not collocated with the actuator.

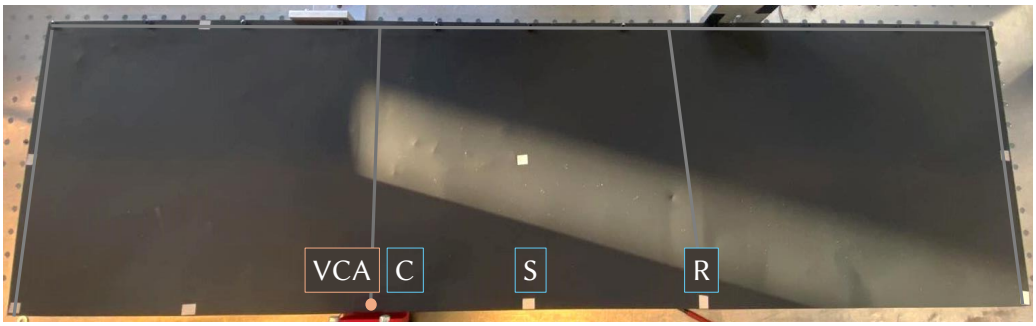

Figure 3.5: Tested fin with reinforcement fork highlighted in gray, Voice Coil actuator impact point shown in orange and the measurement point shown in blue.

The excitation signal consisted of filtered white noise that was cutoff at $50\,\mathrm{Hz}$ to avoid environmental resonances. In addition, the measurements were recorded over $200\,\mathrm{s}$ per point. The input and output signals were scaled as before to express them in terms of force and velocity physical quantities, and the displacement transfer functions were again computed using the relation presented in Equation 3.6.

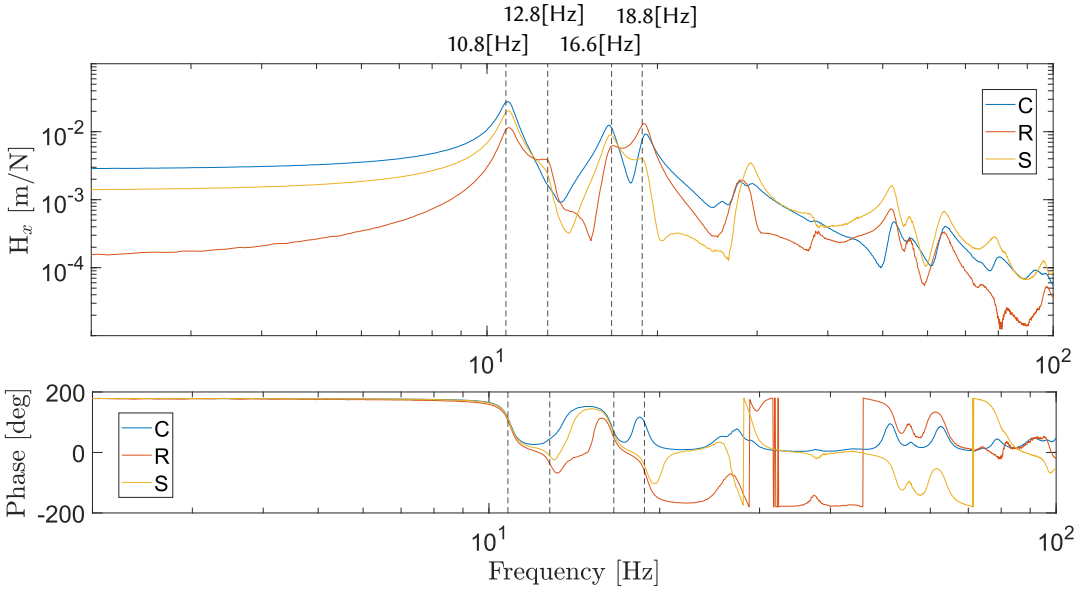

Figure 3.6: Displacement transfer functions of the collocated (C), the soft part (S), and the reinforcement (R) points.

The resulting transfer functions showed smoother curves and cleaner peaks, with significantly improved precision and interpretability, as it can be seen in Figure 3.6. The natural frequencies, identified as the abscissas of the peaks, are listed in Table 3.1.

Mode	**Natural Frequency [Hz]** **Experimental**
1	10.8
2	12.8
3	16.6
4	18.8

Table 3.1: Experimental natural frequencies of the fin.

From these results, the damping can be computed using the half-power bandwidth method,

$$\zeta = \frac{\omega_2 - \omega_1}{2\omega_n}, \tag{3.7}$$

where ω_n is the natural pulsation and ω_1, ω_2 are the half-power pulsation, i.e., the pulsations where the amplitude drops to $1/\sqrt{2}$ of the peak. The resulting damping values for each mode and at each measurement point are listed in Table 3.2.

Mode	**Damping factor [-]** **C**	**Damping factor [-]** **S**	**Damping factor [-]** **R**
1	0.032	0.028	0.035
2	/	/	/
3	0.024	0.0063	/
4	0.027	/	0.0264

Table 3.2: Damping factors of the different modes from the different measurement point.

Another quantity that can be obtained from the transfer functions is the stiffness between two points. In the time domain, stiffness is defined as the ratio of force to displacement. This leads to the expression

$$k = \frac{F}{x}. \tag{3.8}$$

As shown in Equation 3.6, the transfer function gives the displacement per unit force. Therefore, the stiffness can be approximated by the inverse of its magnitude,

$$k(\omega) \approx \frac{1}{|H(\omega)|}. \tag{3.9}$$

To estimate the stiffness between two measurement points, the inverse of the transfer function is evaluated at a frequency that is small but not zero. Stiffness is a static property, and at very low frequencies, the dynamic response approaches the static case. However, using zero frequency is not possible, as it leads to undefined expressions and high sensitivity to noise. A small nonzero frequency avoids these issues and still gives a reliable estimate of the stiffness.

Since the collocated measurement point is taken as a reference value, the stiffness of the reinforcement, k_R is calculated with the difference of the transfer functions evaluated at point C and R.

Similarly, the stiffness at the soft part, k_S, is calculated with the difference of the transfer functions evaluated at point C and S. The resulting values are presented in Table 3.3.

$\mathbf{k_R}[\mathrm{N\,m^{-1}}]$	$\mathbf{k_S}$ $[\mathrm{N\,m^{-1}}]$
367	720.8

Table 3.3: Stiffness between the soft part and reinforcement measurement point with the collocated point.

Note that the magnitude order of the stiffness of the reinforcement part correlates with the clamped beam theory. Indeed, for a beam of length $L = 28.5\,\mathrm{cm}$, thickness $h = 3.55\,\mathrm{mm}$, and width $b = 10\,\mathrm{mm}$, the moment of inertia and the displacement under a $1\,\mathrm{N}$ force at the free end are,

$$I = \frac{bh^3}{12}; \quad f = \frac{1L^3}{3EI} = 0.003\,\mathrm{m}, \tag{3.10}$$

with $E = 6.9 \times 10^{10}\,\mathrm{Pa}$. This yields a stiffness

$$k = \frac{1}{f} = 333.38\,\mathrm{N\,m^{-1}}. \tag{3.11}$$

This value is of the same order of magnitude as the measured one, k_R, which indicates that the laboratory test values are not incoherent.

These laboratory results, including the transfer functions, mode frequencies, damping factors, and stiffness, will serve as a reference to validate the simplified models presented in the following section.

3.1.2 Simplified mass-spring model

Now that the vibrational experimental values of the fin are known, the goal is to create a simplified mechanical model that can simulate the vibrational behavior of this fin. The underlying idea is to later expand this model to the entire cryostat structure, in order to gain an initial understanding of its vibrational behavior without the need for experimental testing.

The simplified model is initially made of spring and lumped masses. Each reinforcement is represented by a spring that is fixed at one end and have a lumped mass at the other end. The fixed end approximates the much stiffer cryostat structure. The soft parts are modeled by another lumped mass that is connected by two springs on each side of reinforcements. This configuration is presented in Figure 3.7.

The stiffness is assumed to be the same for all the reinforcement springs. It is taken as the experimental data, $k_\mathrm{R} = 367\,\mathrm{N\,m^{-1}}$.

The stiffness of the soft section springs could not be directly inferred from the measurements since the displacement measured at the midpoint of the soft section reflects the overall stiffness, distributed across the entire segment, not just at its ends. As a result, the experimental value appears to be stiffer than appropriate for the model. Instead, the stiffness was tuned numerically to match the observed natural frequencies.

The natural frequencies $f_n = \omega_n/(2\pi)$ are obtained by solving the eigenvalue problem

$$\det\left(K - \omega_n^2 M\right) = 0. \tag{3.12}$$

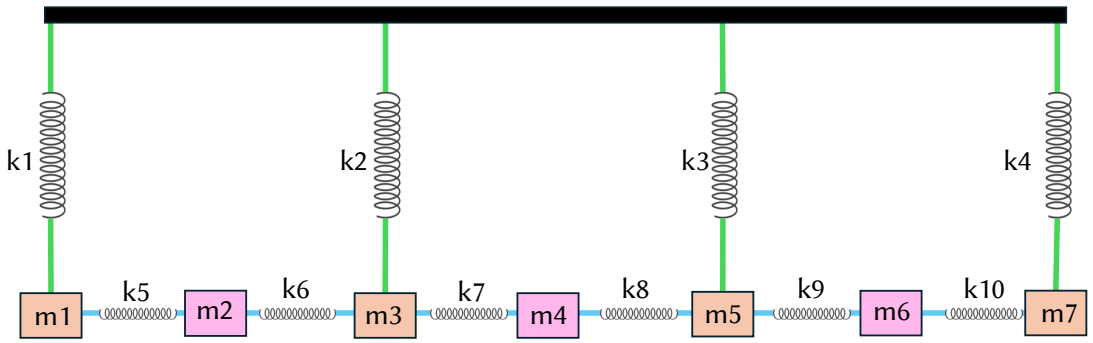

Figure 3.7: Fin Mass-Spring model.

The mass and stiffness matrices are defined as follows,

$$K = \begin{bmatrix} k_1 + k_5 & -k_5 & 0 & 0 & 0 & 0 & 0 \\ -k_5 & k_5 + k_6 & -k_6 & 0 & 0 & 0 & 0 \\ 0 & -k_6 & k_2 + k_6 + k_7 & -k_7 & 0 & 0 & 0 \\ 0 & 0 & -k_7 & k_7 + k_8 & -k_8 & 0 & 0 \\ 0 & 0 & 0 & -k_8 & k_3 + k_8 + k_9 & -k_9 & 0 \\ 0 & 0 & 0 & 0 & -k_9 & k_9 + k_{10} & -k_{10} \\ 0 & 0 & 0 & 0 & 0 & -k_{10} & k_{10} + k_4 \end{bmatrix}, \tag{3.13}$$

$$M = \mathrm{diag}(m_1, m_2, m_3, m_4, m_5, m_6, m_7), \tag{3.14}$$

with

$$k_1 = k_2 = k_3 = k_4 = 367\,\mathrm{N\,m^{-1}}, \tag{3.15}$$

$$m_1 = m_3 = m_5 = m_7 = 0.025\,\mathrm{kg}, \tag{3.16}$$

$$k_5 = k_6 = k_7 = k_8 = k_9 = k_{10} = 103\,\mathrm{N\,m^{-1}}, \tag{3.17}$$

$$m_2 = m_4 = m_6 = 0.04\,\mathrm{kg}. \tag{3.18}$$

The resulting natural frequencies are compared with the experimental results in Table 3.4. Although the model does not perfectly match the measured values, it reproduces the correct frequency range and provides a reliable first-order approximation.

Frequency [Hz] **Experimental**	**Frequency** [Hz] **Mass-Spring model**
10.8	10.9
12.8	12.9
16.6	15.8
18.8	26

Table 3.4: Comparison between the natural frequencies from the laboratory tests transfer functions and the ones from the mass-spring model.

To compute the transfer function of the system, damping is introduced. This later is assumed to be

proportional to the stiffness and is thus defined as,

$$C = 0.0005 \times K. \tag{3.19}$$

The proportional factor 0.0005 was determined through empirical adjustment in order to best match the experimental data. The average damping coefficient derived from the experimental values shown in Table 3.2, 0.03, was initially tested, but it excessively attenuated the response curve, making it impossible to identify the peaks and thus the natural frequencies.

The system equation of motion in the frequency domain becomes

$$(K - \omega^2 M + j\omega C)\hat{X} = \hat{F}, \tag{3.20}$$

where $\omega = 2\pi f$, and $\hat{X}$ and $\hat{F}$ are the complex displacement and force amplitudes, respectively. The transfer function is then

$$H_x(\omega) = \frac{\hat{X}}{\hat{F}} = (K - \omega^2 M + j\omega C)^{-1}. \tag{3.21}$$

In the experiment the force was applied vertically at the collocated point (C) and the displacement response measurements were made at this same point as well as at the middle of the soft part (S) and at the reinforcement (R), as presented in Figure 3.5. To replicate this with the model presented in Figure 3.7, a unitary vertical force is applied at the mass m3. The measurements are made at m3, m4 and m5, corresponding respectively to C, S and R. Mathematically the displacement responses are $\hat{X}_i$ with $i = 3, 4, 5$ and the force is noted $\hat{F}_2 = 1$. Therefore, the transfer functions are expressed as,

$$H_{i,2} = \frac{\hat{X}_i}{\hat{F}_2} = \hat{X}_i. \tag{3.22}$$

The corresponding transfer functions are presented in Figure 3.10. To compare them with the laboratory test results while keeping a good visibility, the transfer functions of each measurement are presented in separated Figures 3.9a, 3.9b and 3.9c.

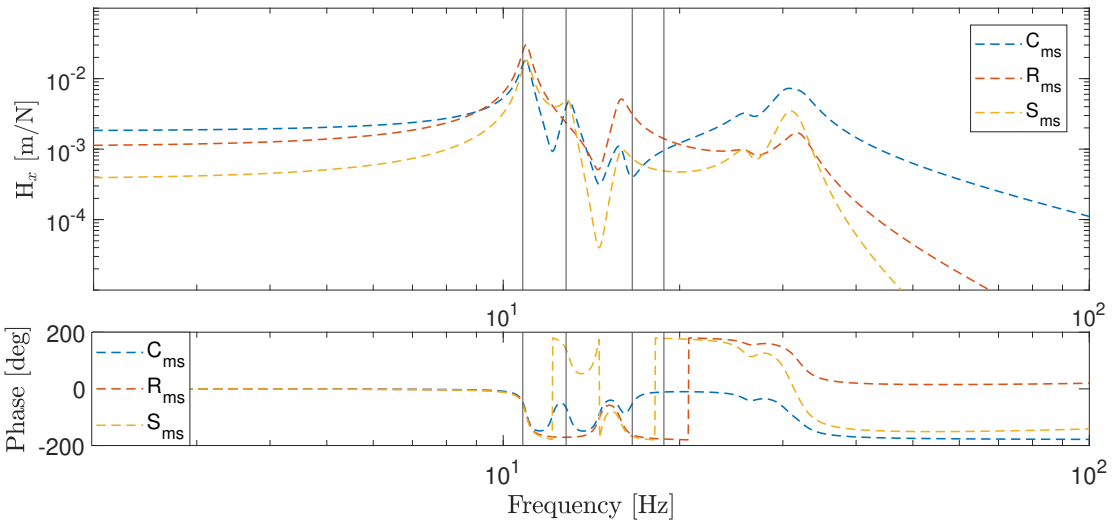

Figure 3.8: Transfer functions obtained with the Mass-Spring (ms) model at the different measurement points, collocated (C), reinforcement (R), soft part (S). The vertical lines highlight the experimental natural frequencies of the fin.

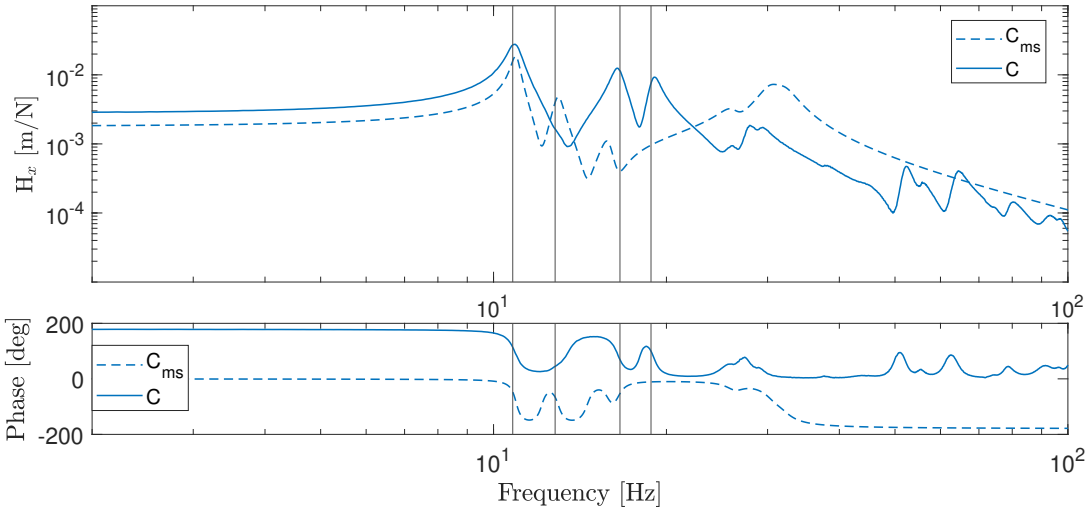

(a) Collocated measurement point (C) that corresponds to the mass m3.

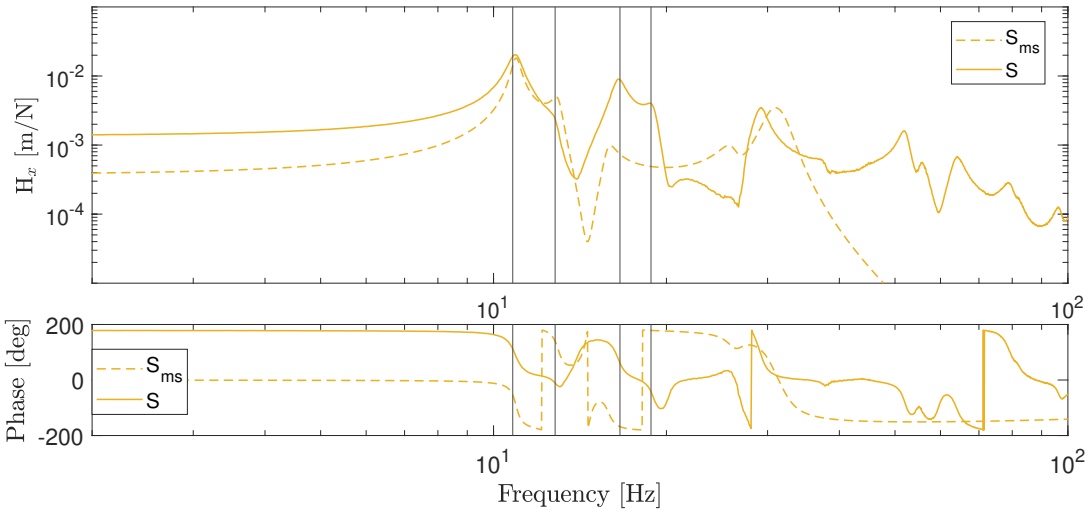

(b) Soft part point (S) that corresponds to the mass m4.

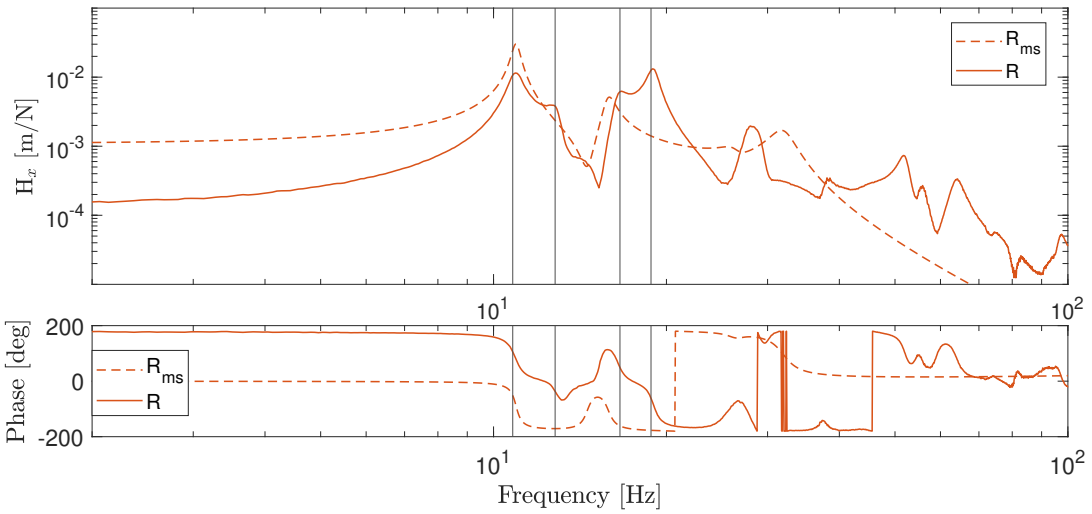

(c) Reinforcement point (R)that corresponds to the mass m5.

Figure 3.9: Comparison between the experimental transfer functions (solid lines) and the ones obtained with the Mass-Spring (ms) model (dashed curves) at the different measurement points with the vertical lines that highlight the experimental natural frequencies of the fin.

As shown in Figure 3.9, the simplified model captures the main trends observed in the experimental data, especially the location of the first few natural frequencies.

In both the experimental and model results, the first major peaks appear at similar frequencies. This leads to comparable natural frequencies for the fin, as listed in Table 3.4. These frequencies are mainly linked to bending in the soft regions of the fin. However, some differences are seen in the shape and amplitude of the transfer functions, especially at higher modes.

A notable difference is found in the fourth peak. The experiment shows a peak at 18.8 Hz, while the model predicts it at 26 Hz. This gap may result from the model simplifications, such as the use of constant stiffness and damping. The real fin also undergoes local deformations that the lumped model does not capture. In fact, the tested fin was visibly deformed, particularly in the soft section represented by mass m2, likely causing a local drop in stiffness.

At low frequencies, another difference is observed. In Figure 3.8, the MS model shows a higher transfer function amplitude for point R than for point S. In contrast, the experimental results in Figure 3.3a show the opposite trend.

These mismatches come from the limits of the mass-spring model. It treats the fin as separate masses linked by ideal springs. The actual fin, however, is a continuous structure with complex shapes and interactions. Damping and stiffness vary along its length, and the coupling between parts is more detailed than the model assumes. This simplification smooths out key effects, shifting some frequencies and altering mode shapes.

Despite its limits, the model offers a good first approximation. It can also be improved. One possible improvement is to refine the stiffness assumption used in Equations 3.15 and 3.17. Another way to enhance the model would be to add more springs, better capturing how the soft regions connect to the full reinforcement contour.

In summary, although the higher natural frequencies and mode shapes differ from those in the experiments, the model gives a useful estimate of the first natural frequencies. Since it is simple to use and to adjust, it remains a valuable tool. Further refinement could make it even more accurate, making it worth keeping and developing.

3.1.3 Simplified FEM model

A simplified model of the fin vibrational behavior is created using the finite element method (FEM) in NX software. The fin is modeled with 2D elements. The aluminum sheet is represented by 2D elements with a mesh size of $10\,\mathrm{mm}$. The fork that reinforces the sheet is also modeled with 2D elements, using a finer mesh of $5\,\mathrm{mm}$. The beam that supports the fin and connects it to the cryostat structure is modeled with 2D elements and a $10\,\mathrm{mm}$ mesh. This part is assumed to be nearly fixed.

A lumped mass is added using a 0D element to represent the magnet of the voice coil used during experimental tests.

Element weights are determined by their material and thickness. Each 2D element is assigned the actual design thickness, $0.3\,\mathrm{mm}$ for the aluminum sheet, $3.5\,\mathrm{mm}$ for the fork, and $10\,\mathrm{mm}$ for the support beam. The fork and the support beam are defined with the Al6061 material. A custom material is created for the sheet.

In reality, the fin is coated with black paint to increase emissivity. Due to the small thickness of the sheet, the added mass from the paint is significant, while the increase in stiffness is assumed negligible. The surface mass density of the painted sheet is computed from the total measured mass of the fin and the known masses of the fork and the support beam. The new material is defined with this surface mass density in addition to the one of the aluminum and uses the same Young modulus as Al6061.

To prevent any relative movement between components, 1D RBE2 elements are used. These elements connect the 2D parts and the 0D mass, reflecting the physical configuration. The final mesh is shown in Figure 3.10.

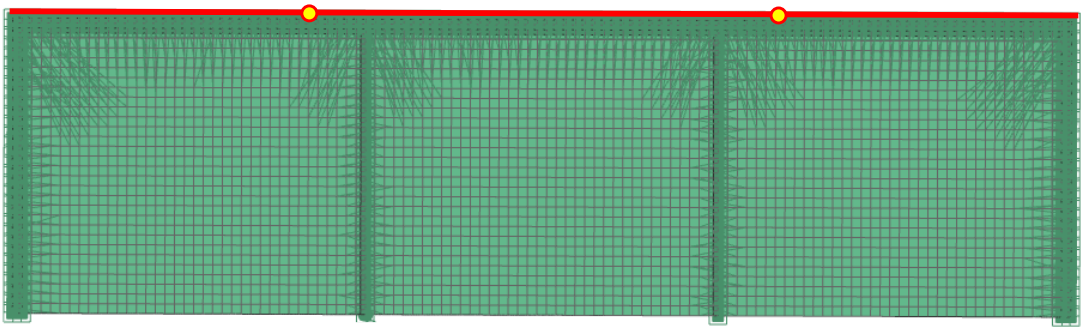

Figure 3.10: NX fin mesh with the two different boundary conditions shown in red and yellow.

Regarding the constraints, the edge of the support beam is fixed along one side, as shown in red in Figure 3.10. This setup is used as a simplified way to represent how the fin is held. However, in the actual experiment, the fin was attached using screws at two separate points. Therefore, to verify that this difference only affects slightly the results, a second simulation is carried out, this time with only the two points, shown in yellow in Figure 3.10, fixed.

Both simulations are run using Simcenter Nastran with the SOL 103 Response Dynamics solver, which provides natural frequencies and mode shapes.

The frequencies from the first simulation, along with detailed information for each mode, including the percentage of mass in the vertical direction (%Z Mass) and in rotation about the X-axis (%RX Mass), are listed in Table 3.5. For comparison, the frequencies from the second simulation are shown in gray. As seen in the table, the natural frequencies change only slightly between the two cases. In addition, the mode shapes of the two simulations are the same. Therefore, the simplified constraint used in the first simulation is considered sufficient, and the rest of the study will focus only on the results of this first simulation.

Mode	Frequency [Hz] Fixed Edge	%Z Mass	%RX Mass	Frequency [Hz] 2 Fixed Points
1	10.8	7%	20%	10.7
2	12.1	3%	10%	12
3	12.2	5%	14%	12.1
4	21	2%	10%	20.6
5	25.3	7%	0.7%	25
6	26.4	1%	4%	25.2
7	26.7	0.4%	0.1%	26
8	27.1	0.6%	3%	26.8
9	28.9	0.1%	0.2%	27
10	30.6	54%	15%	27.3

Table 3.5: Frequency and mass distribution of the modes from the first FEM simulation, with a comparison to the mode frequencies from the second FEM simulation.

The modal mass percentages, shown in Table 3.5, help to determine which modes are most relevant. Higher values in the Z direction and around the X-axis (RX) indicate that a mode is more likely to be excited when a force is applied in those directions. This is particularly important here, as the

excitation in the laboratory tests was applied in the Z direction, which also causes some rotational motion around the X-axis.

The modes with the highest modal mass percentages are highlighted in yellow in Table 3.5 and their corresponding shapes are shown in Figure 3.11. In all the sub-figures, a cube appears at the position of the lumped mass that represents the magnet of the VCA in the laboratory test. The first three modes, illustrated in Figures 3.11a to 3.11c, represent local bending of the fin soft segments. It indicates that under vertical excitation, the soft parts of the fin tend to oscillate independently at frequencies around $11\,\mathrm{Hz}$. These deformations occur primarily in the vertical (Z) direction and are accompanied by rotation around the X-axis. This behavior is consistent with their relatively high modal mass values in the Z and RX directions.

As the frequency increases, the deformation patterns become more complex and less predictable. In Figure 3.11d, the entire structure participates in the motion, including the stiff region where the VCA magnet is attached. However, in the following mode, shown in Figure 3.11e, the deformation is limited to the soft central region of the fin and forms a wavelike shape. The mode presented in Figure 3.11f is more complex. It shows multiple wave fronts distributed along the structure. Despite its higher natural frequency, this mode is particularly significant due to its exceptionally high modal mass in the Z direction (54%), which highlights the complexity in the interpretability of these modes.

To enable a meaningful comparison between the simulation and experimental data, the simulated modes and frequencies in Table 3.6 must be filtered. In the experimental transfer function plots, closely spaced modes cannot be distinguished clearly due to limited frequency resolution and overlapping peaks. Therefore, only modes that are well separated and have substantial modal mass can be reliably identified. For instance, between the second and third simulated modes, only the second is retained for comparison, as it carries more modal mass and is thus more likely to appear clearly in the experimental data.

Additionally, the analysis is limited to modes with natural frequencies up to $25\,\mathrm{Hz}$. This range corresponds to the first four peaks observed in the experimental transfer functions and includes the most clearly identifiable modes.

The selected simulation results are compared with the measured frequencies in Table 3.6.

Frequency [Hz] Experimental	**Frequency [Hz] First FEM Simulation**	**Mode First FEM Simulation**
10.8	10.8	1
12.8	12.2	3
16.6	/	/
18.8	21	4

Table 3.6: Comparison between the natural frequencies from the laboratory tests transfer functions and the mode frequencies from the first FEM simulation.

As shown in Table 3.6, although the natural frequencies from the simulation do not match the measured values exactly, they are of the same order of magnitude. This similarity in frequency is a good indication that the simulation model captures the general dynamic behavior.

However, comparing the mode shapes from the simulation with those suggested by the experimental transfer functions is more difficult. There are noticeable differences between them. For example, the first mode shape in NX, shown in Figure 3.11a, appears almost symmetric, with the largest movement occurring in the soft region at the center of the fin. In contrast, the measurements show

that the collocated point has the highest amplitude compared to the soft part and the reinforcement. Additionally, the simulation does not provide enough information to make clear conclusions about the phase of the mode shape.

Therefore, although the correlation in natural frequencies supports the idea that the FEM model captures the general dynamic behavior of the system, the differences observed in the mode shapes make it difficult to validate the model.

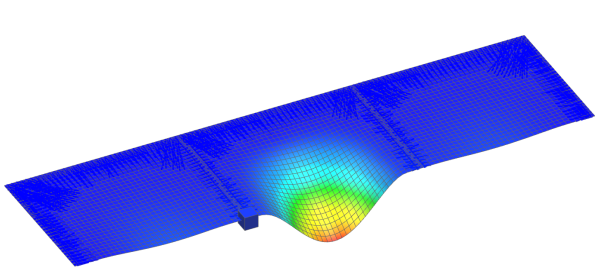

(a) Mode 1: 10.8 Hz.

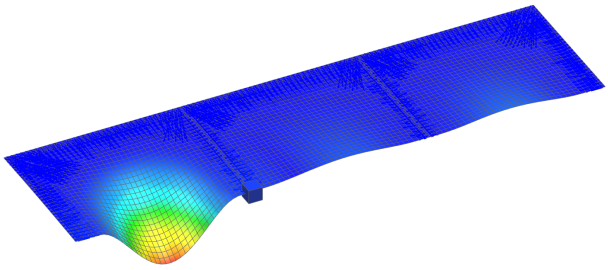

(b) Mode 2: 12.1 Hz.

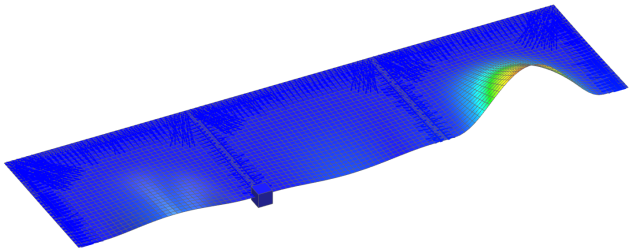

(c) Mode 3: 12.2 Hz.

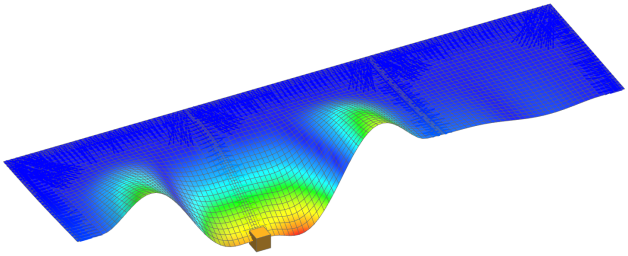

(d) Mode 4: 21 Hz.

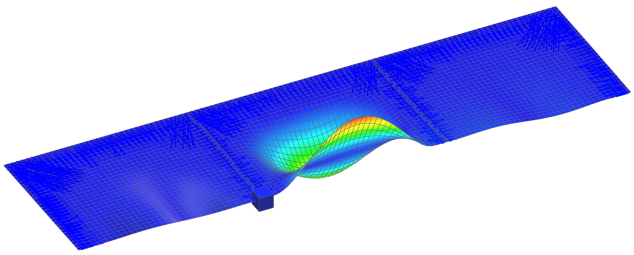

(e) Mode 5: 25.3 Hz.

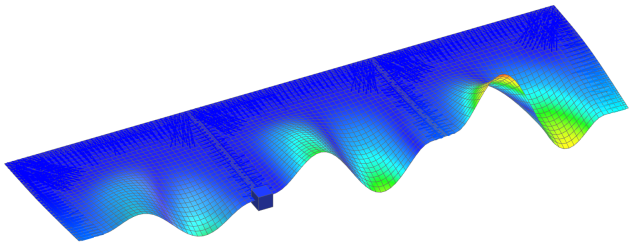

(f) Mode 10: 30.6 Hz.

Figure 3.11: NX first mode shapes from the fin FEM simulation.

Vibrational analysis conclusion

This section analyzed the vibrational behavior of a single cryostat fin using experiments and simplified models. Laboratory tests yielded the first natural frequencies, damping ratios, and stiffness at selected points. Then, simple mass-spring and FEM models were developed to reproduce the vibrational behavior of the fin. The mass-spring model captured general trends and gave a good estimate of the first frequencies. However, it did not reproduce mode shapes or higher-order modes. Similarly, the FEM confirmed the frequency range but showed different mode shapes.

Therefore, despite the differences, all results agree that the first four vibration modes are between 10 Hz and 20 Hz. These values are above typical environmental vibration ranges, reducing the risk of resonance.

This work provides a starting point for extending the vibration analysis to more accurate fin models and later adapting these models to the full cryostat.

3.2 Thermal model description

To begin the thermal study of the E-TEST prototype, an electrical network analogy is made using isothermal node discretizations. This simplified model is composed of 3 nodes, the mirror, the internal radiative heat exchanger (IRHX) that corresponds to the set of fins directly linked with the payload, and the external radiative heat exchanger (ERHX), that is the thermal sink of the system. This latter is composed of the complementary outer set of fins mounted on the GHe-fed panels. This model is presented in Figure 3.12. The radiation between the IRHX and the mirror is neglected as it is assumed that they are at close temperature and that the conduction heat transfer is more important than the radiation. In addition, it is assumed that external parasitic heat loads are transferred to the IRHX and not directly to the mirror.

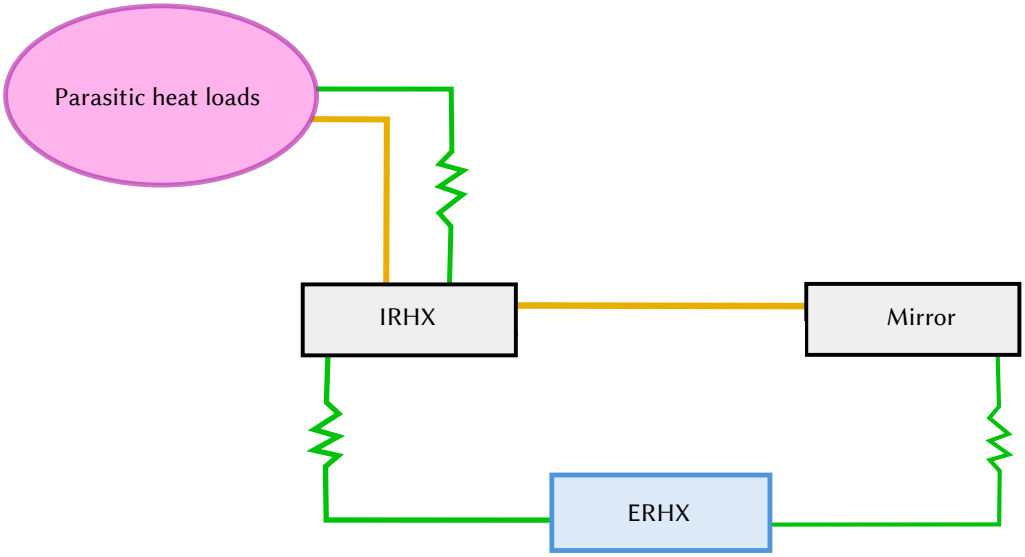

Figure 3.12: Electrical network analogy to represent the thermal model of the E-TEST cryostat system. The radiative links are presented in green while the conductive links are shown in orange.

3.2.1 Parasitic heat loads evaluation

It is essential to evaluate the heat load transferred to the payload from the external environment, as this determines the amount of heat that the heat exchanger must remove. This, in turn, directly influences the required radiative surface area A_{IRHX}. These parasitic heat loads originate from four primary sources, heat conduction through marionette suspension wires, conduction through the harness wires (necessary for the thermal and vibration sensors), and radiative heat transfer from the external environment via the tubes on top of the cryostat and in front of the mirror, as well as through discontinuities in the thermal insulation. This can be summarized in the following expression,

$$\dot{Q}_{parasit} = \dot{Q}_{c,harness} + \dot{Q}_{c,suspension} + \dot{Q}_{r,MLI} + \dot{Q}_{r,tubes}. \tag{3.23}$$

The parasitic heat loads have been assessed in the reference study [13], using ESATAN, a software tool for thermal analysis of spacecraft. This evaluation yielded a total heat rate of $366\,\mathrm{mW}$. In the following sections, an analytical approach is employed to estimate the parasitic heat loads. The analytical results are expected to be consistent with those obtained with ESATAN. The goal is to adjust the simplified model such that it reproduces the reference results as closely as possible.

Starting by the conduction parasitic heat loads, $\dot{Q}_{c,harness}$ and $\dot{Q}_{c,suspension}$ can be computed using Equation 2.1, presented in the heat transfer theory recall chapter. To do so, the cross-sectional areas, thermal conductivity, and length of the conductors must be evaluated.

The cross-sectional areas are accurately known based on the specifications of the cables used in the E-TEST. The suspension wires consist of three titanium cables, each with a diameter of 3 mm. The electrical harness is made from a combination of 150 AWG32 cables and 50 AWG24 cables, all composed of phosphor-bronze[13].

In addition, the thermal conductivities for both the harness and suspension wires are also known. As said in the theoretical recall, the thermal conductivity is a material property that depends only on the temperature. In addition, the temperatures are assumed to be $293\,\mathrm{K}$ in the surrounding environment and $22\,\mathrm{K}$ inside the cryostat. Therefore, the thermal conductivities are evaluated at the average temperature, using reference tables from [21] and [22].

In contrast, the effective cable lengths over which the temperature gradient takes place are not precisely known. Therefore, they were tuned to match the ESATAN results of [13]. The effective length of the suspension cables is $\approx 30\,\mathrm{cm}$. The harnesses are assumed to be much longer since they are coiled around them and their effective length is assumed to be $\approx 2\,\mathrm{m}$.

A summary of the cables parameters and the estimated resulting parasitic loads is presented in Table 3.7.

Parameters	Harness	Suspension
$A[\mathrm{mm}^2]$	15	21
$\Delta x[\mathrm{m}]$	2	0.3
$k[\mathrm{W\,m^{-1}\,K^{-1}}]$	34.79	4.81
$\dot{Q}_c[\mathrm{mW}]$	71	92
$\dot{Q}_{c,ESATAN}[\mathrm{mW}]$	62	84
$\dot{Q}_{r,ESATAN}[\mathrm{mW}]$	19	5

Table 3.7: Parameters of the harness and suspension cables along with their analytical resulting conductive heat loads in comparison with the corresponding radiative and conductive reference heat loads obtained with ESATAN in [13].

For the radiative parasitic heat loads, the two contributions must be treated separately due to their different configurations. The first involves radiation through discontinuities in the MLI and thermal shielding layers (LN_2 and GHe), while the second concerns radiation along thermal baffling tubes.

To estimate the radiative heat transfer through the MLI, the unfilled surface areas of the cold shrouds were quantified using the CAD model of the E-TEST prototype thermal layers, which are illustrated in Figure 3.13. The GHe plates are depicted in blue and shown Figure 3.13a. The surrounding LN_2 thermal layer is shown in brown in Figure 3.13b. The unfilled surfaces between the plates represent all potential paths through which environmental heat can penetrate. They were measured, and the total unfilled surface areas of both thermal layers are presented in Table 3.8.

	GHe thermal layer	LN2 thermal layer
$\mathbf{A_{unfd}}[\mathrm{m}^2]$	0.77	0.55

Table 3.8: Thermal layers unfilled surface areas.

A typical assumption in CSL analyses is that a heat flux of $5\,\mathrm{W\,m^{-2}}$ occurs through one square meter of MLI between $300\,\mathrm{K}$ and $80\,\mathrm{K}$. Based on this, an effective emissivity can be derived using Equation 3.35,

$$\varepsilon^*_{MLI} = \frac{5}{\sigma(300^4 - 80^4)} = 0.0109[-]. \tag{3.24}$$

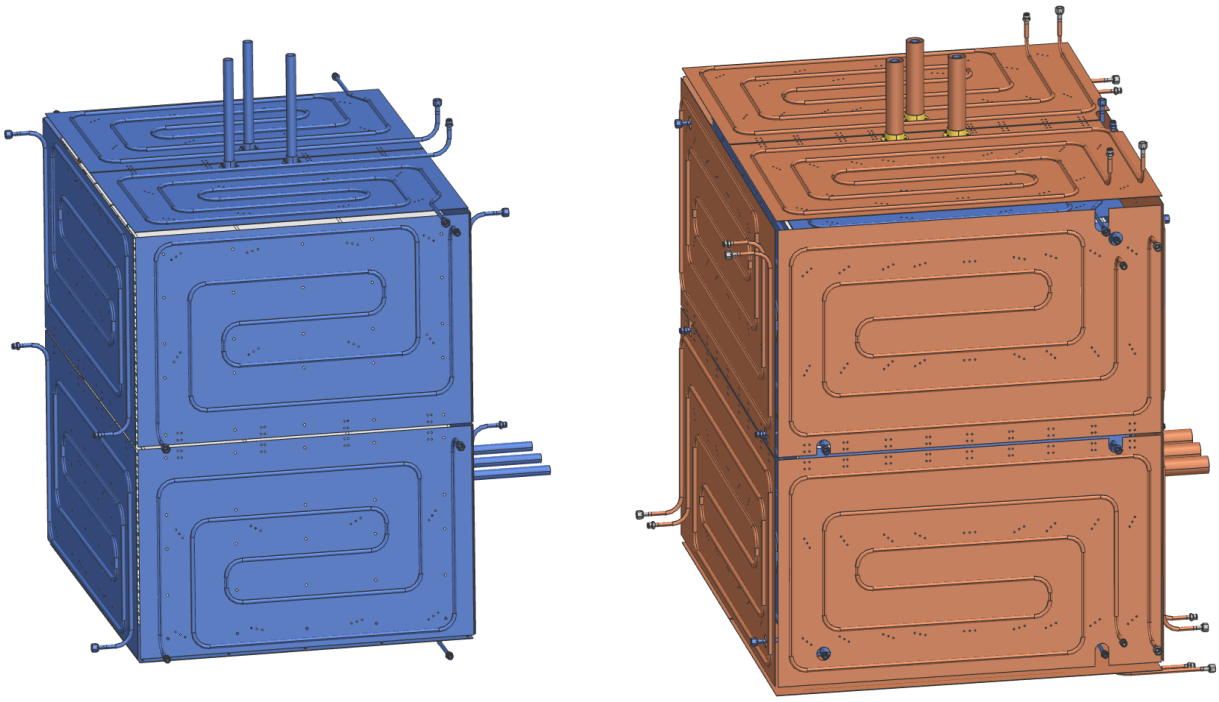

(a) GHe thermal layer CAD model.

(b) LN2 thermal layer CAD model.

Figure 3.13: NX CAD model of the thermal layers showing visibly unfilled surface areas.

Using this effective emissivity and assuming a view factor of 1 between the LN_2 plates at $80\,\mathrm{K}$ and the GHe plates at $15\,\mathrm{K}$, the effective radiative conductance through the MLI is:

$$GR_{MLI} = (A_{LN_2,unfd} + A_{GHe,unfd})\varepsilon^*_{MLI}, \tag{3.25}$$

$$\tag{3.26}$$

This is then injected in Equation 3.35 to compute the radiative heat transfer through a perfect MLI. However, some imperfection must be considered in the MLI. This is done considering an MLI performance degradation $\approx 300\%$. This value was tuned so that the resulting heat load was close to the ESATAN one. Both are compared in Table 3.9.

	Analytic	**ESATAN**
$Q_{r,MLI}[\mathrm{mW}]$	129	143

Table 3.9: Radiative heat transfer through MLI layer from the analytical model and ESATAN results in [13].

The analysis is now focused on the parasitic radiative fluxes transmitted through the tubes that establish a direct connection between the external environment and the space surrounding the payload. The two sets of three tubes are made of copper with a diameter $d = 3\,\mathrm{cm}$ and a length $l = 40\,\mathrm{cm}$. The emissivity of copper at cryogenic temperatures is very low, $\varepsilon_{copper} \approx 0.07$[23].

Additionally, to be able to use Gebhart's method, it is assumed that the interior surface is diffuse, isotherm, uniformly irradiated, and gray. The diffuse surface assumption means that the inside surface of the tubes acts like a matte wall where the radiation reflects in all directions uniformly.

The first step consists in determining the view factors. Note that the top and bottom surfaces are named respectively, 1 and 2, while the side surface is noted 3. The view factor between the top and

bottom is obtained using the formulas of the view factor from a disk to a parallel coaxial disk of same radius[24]. That is

$$\begin{aligned} R &= \frac{d/2}{l}, \\ X &= \frac{2R^2+1}{R^2}, \\ F_{12} &= 0.5\left(X - \sqrt{X^2-4}\right). \end{aligned} \tag{3.27}$$

By symmetry and using the property specific to the view factors, the following expressions are obtained.

$$F_{21} = F_{12}, \qquad \text{(By symmetry)} \tag{3.28}$$

$$F_{13} = 1 - F_{12}, \qquad \text{(from Eq. 2.9)} \tag{3.29}$$

$$F_{23} = 1 - F_{21}, \qquad \text{(from Eq. 2.9)} \tag{3.30}$$

$$A_1 = \pi(d/2)^2; A_3 = 2\pi(d/2)l; \qquad F_{31} = \frac{A_1 F_{13}}{A_3}, \qquad \text{(from Eq. 2.8)} \tag{3.31}$$

$$A_2 = A_1; \qquad F_{32} = \frac{A_2 F_{23}}{A_3}. \qquad \text{(from Eq. 2.8)} \tag{3.32}$$

To simplify the computation of the Gebhart's factor, the expression presented in the theoretical reminder in Equation 2.6 can be rewritten in a matrix form as

$$\beta_{ij} = F_{ij}\varepsilon_j; \quad \mathbf{B} = (\mathbf{I} + \boldsymbol{\beta} - \mathbf{F})^{-1}\boldsymbol{\beta}, \tag{3.33}$$

with F_{ij}, the view factors obtained just above, and ε_j, the vector containing the emissivity of each surfaces of the tubes. The top and bottom surfaces are left opened which means the absorptivity is total and thus the emissivity is also of 100%. The third surface is the internal surface of the copper tube that has an emissivity of 7%. However, due to the big assumptions made to use the Gehbart's method, using this emissivity lead to a radiation heat rate more than four times bigger then the one resulting from the ESATAN model. Therefore, to better match the reality the emissivity of the interior surfaces of the tubes has been increased to 40%. Therefore, the vector of emissivities is,

$$\boldsymbol{\varepsilon} = [1 \quad 1 \quad 0.4]. \tag{3.34}$$

Then, the radiative conductance matrix can be defined using Equation 2.10. The element of this matrix that is of interest is the element GR_{12} ($= GR_{21}$ by symmetry), as it defines the radiative conductance between the top and bottom of the tube, where the heat flux is transferred from the external environment. Therefore, injecting this expression in the equation of radiative heat transfer shown in Equation 3.35, and taking into account that there is actually six tubes, one gets,

$$\dot{Q}_{r,tubes} = 6 \times GR_{12}\sigma(T_1^4 - T_2^4) = 6 \times (1.85 \times 10^{-5})\sigma(T_1^4 - T_2^4). \tag{3.35}$$

The resulting radiative heat load, considering a environment temperature, T_1, of $295\,\mathrm{K}$ and a payload surrounding temperature, T_2, of $22\,\mathrm{K}$, is presented in Table 3.10, where it is compared to the value obtained with ESATAN presented in the reference paper[13].

	Gebhart method	ESATAN
$Q_{r,tubes}[\mathrm{mW}]$	50	51

Table 3.10: Radiative heat transfer through the tubes from the analytical model and ESATAN results in[13].

Finally, a summary of the values obtained for the different contributions to the parasitic heat load, along with the results presented in[13] is provided in Table 3.11.

Heat loads $[\mathrm{mW}]$	**Analytic**	**ESATAN**
$\dot{Q}_{harness}$	71	62 + 17
$\dot{Q}_{suspension}$	92	84 + 5
$\dot{Q}_{MLI}$	129	143
$\dot{Q}_{tubes}$	50	51
Total $\dot{Q}_{parasitic}$	342	366

Table 3.11: Parasitic heat load contributions from the analytical model and ESATAN results in [13].

As shown in Table 3.11, the total parasitic heat load estimated analytically is $342\,\mathrm{mW}$, which is about 7% lower than the $366\,\mathrm{mW}$ obtained from the ESATAN simulation. This is a pretty good estimation considering such a simple model. The analytical method gives a good rough estimate of the total parasitic load. However, it should be used with caution in later design stages as big assumptions where made to obtain these results.

3.2.2 Transient thermal behavior of the simplified model

The transient thermal behavior of the E-TEST prototype is analyzed using the node model depicted in Figure 3.12. The simulation spans 18 days, with the heat exchanger and mirror temperatures as the unknowns. The environmental temperature is considered constant and known, while the sink temperature is externally controlled. Specifically, the GHe panels are cooled by the CSL helium refrigerator, which provides a known sink temperature.

The environmental temperature is assumed to be $293\,\mathrm{K}$ throughout the experiment. The sink temperature starts at room temperature and takes $\approx\ 12\,\mathrm{h}$ to reach $15\,\mathrm{K}$, at which point it remains constant for the remainder of the experiment.

To determine the transient temperature behavior of the IRHX and mirror nodes, a system of ordinary differential equations is first implemented using the expression presented in Equation 2.16 that is particularized to each node. This yields the system

$$\begin{cases} \dfrac{dT_m}{dt} = \dfrac{1}{m_m c_{p,m}} \left(-\dot{Q}_{c,IRHX\to m} - \dot{Q}_{r,ERHX\to m}\right), \\ \dfrac{dT_{IRHX}}{dt} = \dfrac{1}{m_{IHX} c_{p,RHX}} \left(\dot{Q}_{parasitic} + \dot{Q}_{c,m\to IRHX} - \dot{Q}_{r,ERHX\to IRHX}\right), \\ \qquad\quad = \dfrac{1}{m_{IRHX} c_{p,RHX}} \left(\dot{Q}_{c,harness} + \dot{Q}_{c,suspension} + \dot{Q}_{r,MLI} + \dot{Q}_{r,tubes} \right. \\ \qquad\qquad \left. + \dot{Q}_{c,m\to IRHX} - \dot{Q}_{r,ERHX\to IRHX}\right). \end{cases} \tag{3.36}$$

In this system presented in Equation 3.36, m_m and m_{IRHX} are, respectively, the mass of the mirror and the mass of the IRHX, which includes the mass of the fins and the structure on which it

is mounted and the payload excluding the mirror. These two values, known from the prototype, are presented in Table 3.12. Similarly, $c_{p,m}$ and $c_{p,RHX}$, are the thermal capacities under constant pressure of the mirror and heat exchanger. The thermal capacity of an element depends on its temperature. As the mirror and IRHX are both made of aluminum 6061, their thermal capacities at the various temperatures are computed based on the same formula found in NIST data base[25].

$\mathbf{m_m}[\mathbf{kg}]$	$\mathbf{m_{HX}}[\mathbf{kg}]$
100	191

Table 3.12: Mass values of the mirror and heat exchanger

The evaluation of the parasitic heat loads during the simulation follows exactly the same method as presented in the previous section but with a transient IRHX temperature.

Looking at the heat transfer inside the system, it can be seen that some heat is transmitted from the mirror to the internal radiative heat exchanger ($\dot{Q}_{c,m\rightarrow IRHX} = -\dot{Q}_{c,IRHX\rightarrow m}$) and that both the mirror and the heat exchanger transmit heat to the ERHX.

To determine the heat load that passes through the conductive link between the mirror and the IRHX, Equation 2.1 is again used. The link is made of CuCrZr, for which thermal conductivities at different temperatures are provided in [26]. The link is composed of three sections, with the middle section being larger than the extremities but all sections being circular. The diameter and length of each part are presented in Table 3.13.

Parameters	**Extremities**	**End**
L $[\mathrm{cm}]$	4.5	54
d $[\mathrm{mm}]$	3	9

Table 3.13: Lengths (L) and diameters (d) of the different parts of the link between the mirror and the internal radiative heat exchanger.

Knowing that the cross sections are circular, the equation of conduction, Equation 2.1 is then used to compute the heat load that is transferred from the mirror to the IRHX with the varying temperatures.

The radiative heat loads transferred from the mirror and the IRHX to the ERHX, $-\dot{Q}_{r,ERHX\rightarrow m}$ and $-\dot{Q}_{r,ERHX\rightarrow IRHX}$, are computed following the same methodology, using again the expression in Equation 3.35. The mirror and the fins of the heat exchanger are made of aluminum painted in black, which leads to a value of the emissivity assumed to $\varepsilon_{RHX} = 0.65$[13]. Nevertheless, both elements are in different configurations, leading to different radiative conductances. For the heat exchanger, the case of two infinite diffuse, opaque and gray surfaces is considered. This yields the expression shown in Equation 2.4, which yields the following radiative conductance,

$$GR_{IRHX\rightarrow ERHX} = A_{IRHX}\frac{\varepsilon_{RHX}}{2-\varepsilon_{RHX}}, \tag{3.37}$$

with $A_{IRHX} = 79.3[m^2]$, the radiative surface of the internal heat exchanger.

On the contrary, for the radiative heat transfer between the mirror and the ERHX, it is assumed that there is a factor of view of one between these two elements. Therefore the radiative conductance is simply,

$$GR_{m\rightarrow ERHX} = A_m\varepsilon_m, \tag{3.38}$$

with $A_m = 0.7[m^2]$, the radiative surface of the mirror.

Once the system of ordinary differential equations is properly defined, it is solved numerically using *ode23* in Matlab. This solver function is based on a low-order Runge–Kutta method suitable for non-stiff problems and computes the evolution of the system over time, providing temperature values at each time step[27]. Indeed, the thermal system exhibits smooth and gradual dynamics without rapid transients or sharp discontinuities, justifying the use of a non-stiff solver that is computationally efficient and accurate for such behavior.

To ensure high numerical precision, the relative and absolute error tolerances are both set to 10^{-12}. The solver uses an adaptive time-stepping strategy based on the Runge–Kutta method, automatically adjusting the step size to meet the error criteria. No initial or maximum step size is specified, so the solver selects them automatically. The integration time interval is set to 18 days, as it was the duration of the prototype test, and the mirror and the IRHX were initially set at the ambient temperature of $293\,\mathrm{K}$.

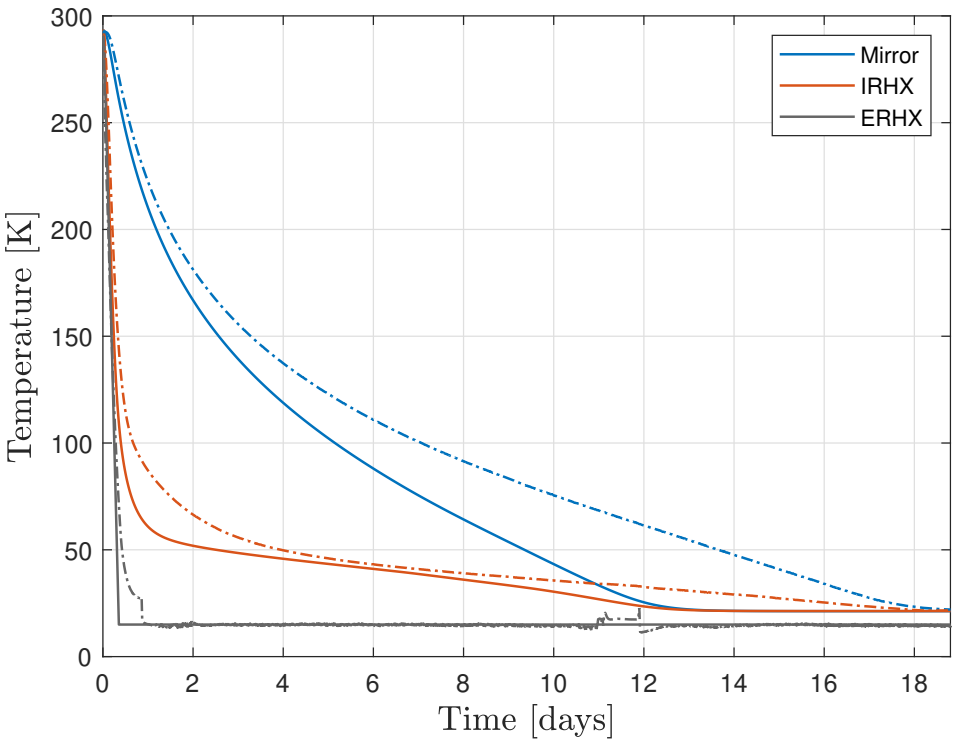

Figure 3.14: Time evolution of the mirror, IRHX, and ERHX temperatures. Analytical results are shown as solid lines, while experimental data from the E-TEST cooling experiment (conducted at CSL) are shown as dashed-dotted lines.

Figure 3.14 compares the temperature evolutions of each component of the experimental test with those resulting from the analytic method presented just above. Although the analytical and experimental curves do not perfectly overlap, they exhibit a similar overall trend. This suggests that the simplified model provides a reasonably accurate first approximation of the cooling behavior of the prototype.

To be able to compare the experimental results more precisely with the analytical method, the final temperatures, after 18 days of cooling, of each element of the thermal node model, from the simulation and the experimental test, are compared in Table 3.14. It can already be seen that the CSL helium refrigerator has a higher cooling performance than expected as the ERHX temperature is slightly overestimated.

The differences between the experimental data and the analytical results are mainly caused by

Node	Temperature [K] Experimental	Temperature [K] Simulation
Mirror	22.11	21.27
IRHX	21.6	21.32
ERHX	14.7	15

Table 3.14: Comparison of the temperatures, after 18 days of cooling, of the thermal node model elements resulting from the simulation and the experimental test.

simplifications in the thermal model. The model does not fully capture the complexity of the real system. Specifically, the analytical study only includes heat conduction through the harness and suspension cables. However, the ESATAN results indicate that radiative heat transfer also occurs in these parts in Figure 3.7.

In addition, the model uses lumped masses, while the actual mass is distributed. Therefore, the heat capacity at constant pressure is calculated at a single temperature per element while in reality, the temperature varies across different parts of the same element.

Similarly, temperature is only computed at the two ends of the conductor between the mirror and the IRHX. The thermal conductivity is then estimated at the average of these two temperatures. This method does not reflect how temperature changes along the conductor. Therefore, it cannot accurately capture how the thermal conductivity of the material varies with temperature, which affects the predicted mirror temperature.

To improve accuracy, the simplified model should include more nodes and account for radiative heat transfer in the harness and suspension components.

However, despite these limitations, the simplified model remains a useful tool for obtaining a general understanding of the thermal behavior of the cryostat.

Thermal analysis conclusion

This section has presented the development of a reduced thermal model of the current E-TEST prototype. Although the model is very simple, it already provides a reasonable approximation of the thermal behavior of the cryostat. Therefore, this thermal analysis will be used in the next chapters to evaluate and compare the thermal performance of possible improved design with that of the current prototype.

3.3 Conclusion

The objective of this chapter was to better understand the current E-TEST prototype by studying its vibrational and thermal behavior and to develop simplified models that approximate its behavior well.

The vibrational behavior of an individual cryostat fin was first investigated. Experimental measurements showed that the first natural frequencies lie between 10 and 20 Hz, which is sufficiently high to avoid resonance with typical environmental disturbances. Two simplified models, a mass-spring system and a finite element model, were developed to reproduce this behavior. Both captured the correct first natural frequency range, but their mode shapes differed from those observed experimentally. The mass-spring model was found to be the most promising for further use due to its adaptability and simplicity. With minor refinements, it could realistically replicate the fin vibrational behavior. Then, the objective would be to scale this model up to represent the full E-TEST cryostat vibrational behavior.

Subsequently, a simplified three-node thermal model was elaborated. Parasitic heat loads were estimated analytically and tuned to match results from the ESATAN software in [13]. A transient simulation of the cryostat cooling process confirmed that the mirror reaches its target temperature of approximately $22\,\mathrm{K}$ in less than three weeks, consistent with experimental data. This model provides a useful framework for analyzing and comparing the thermal performance of future cryostat designs.

In summary, this chapter introduced simplified models for estimating the vibrational and thermal behavior of the current cryostat prototype. The mass-spring model is expected to be refined and scaled up to the full structure, while the thermal modeling approach will be directly reused in the following chapters to assess the thermal performance of the new E-TEST cryostat designs. In the second part of this paper, it will also be adapted to simulate the thermal behavior of the ET-cryostat.

CHAPTER 4

POTENTIAL IMPROVEMENTS

This chapter explores several possible improvements to the current E-TEST cryostat design. Some aim at simplifying the assembly process or reducing the risk of mechanical contact, while others focus on enhancing thermal performance. The proposed changes are grouped into low-complexity modifications, which can be implemented with minimal redesign, and high-complexity modifications that involve a complete rethinking of the RHX or fins geometry.

4.1 Low-complexity improvements

4.1.1 Enhancement of the emissivity of the inner surface of the tubes

During the E-TEST prototype assembly, an issue with the top tubes has been observed. Since the tubes are relatively long and end up very close to the marionette, the electrical cables and optical fibers coming out of the tubes have to bend sharply to avoid this marionette. This is not ideal and increases the risk of contact, in addition to the risk of damaging the optical fibers. One possible solution is to shorten the three tubes located on top of the cryostat structure and possibly increase their diameter to make assembly easier. However, shortening the tubes and/or increasing their diameter leads to higher heat transfer from the environment to the payload. Therefore, to compensate for the reduced length, the inner surface emissivity of the tubes should be increased.

This section first highlights the limitations of the analytical and numerical methods used to evaluate the radiative heat load through the tubes, and then assesses the impact of different tube geometries, either shorter or with a larger diameter.

Analytical method limitations for evaluating heat transfer through the top tubes

It is important to realize that even if the analytical method to compute the heat rate passing through the tubes of the prototype, presented in Section 3.2.1, yields a good first order of magnitude, it is still inexact and could diverge from the reality for other parameter considerations. Therefore, to evaluate the imprecision of the analytical method, a numerical method, using ESATAN and its ray-tracing capabilities, has been applied to the same configuration.

For both methods, the heat loss is evaluated using the expression of radiation heat transfer given in Equation 3.35. Since the focus is on the total radiative heat loss through the three tubes located on top of the cryostat, the equation simplifies to

$$\dot{Q}_{r,TopTubes} = 3 \times GR\sigma(T_{env}^4 - T_{IRHX}^4), \tag{4.1}$$

With $T_{env} = 293[K]$ and $T_{IRHX} = 15[K]$. In the analytical approach, the Gebhart method is used to calculate the GR factor, following the same procedure as for $\dot{Q}_{r,tubes}$ described in Section 3.2.1. This method assumes that the surfaces are isotherm, uniformly irradiated, gray, and perfectly diffuse.

In contrast, for the numerical approach, ESATAN computes the GR via Monte Carlo ray tracing. This method allows for varying the ratio of diffusivity to specularity, and can model extreme cases of fully diffuse or fully specular surfaces. In addition, it inherently takes into account non-uniformly irradiated surfaces.

Initially, the ESATAN model is used under the same conditions as the analytical method, assuming purely diffuse radiation. Therefore, the main differences between the Gebhart method and ESATAN arise from the way radiative exchanges are computed. The Gebhart method uses analytical view factors and solves radiation exchange through matrix inversion, as shown in Equation 3.33, which can introduce approximation errors, especially in capturing multiple reflections or subtle angular effects. In contrast, ESATAN uses Monte Carlo ray tracing to numerically compute view factors and simulate multiple reflections explicitly, offering higher accuracy by accounting for geometric nuances and energy redistribution more precisely. This explains the observed differences in GR values, despite the identical geometry and diffuse assumptions.

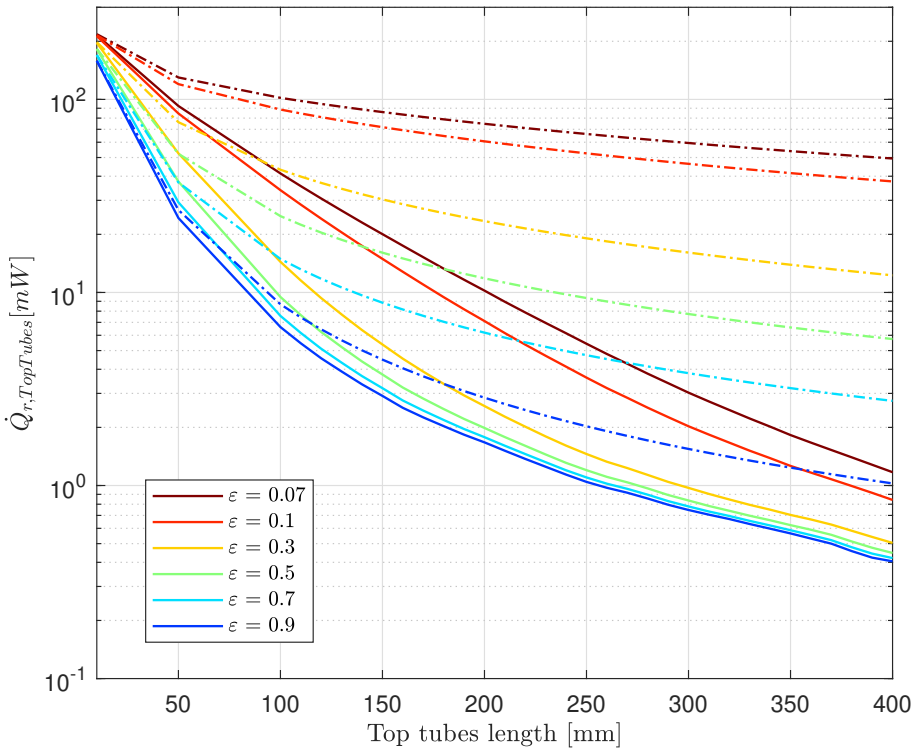

Figure 4.1: Evolution of the heat rate passing through the top tubes for different tube lengths and a constant tube diameter of $3\,\mathrm{cm}$ at different emissivity. The dashed-dotted lines are the result of the analytical method while the solid lines are the results of the Monte Carlo ray-tracing method considering diffuse inner tubes surface.

A clear difference between the analytical results, in dashed-dotted lines, and the ray-tracing results assuming diffuse radiation, in solid lines can be seen in Figure 4.1. This highlights that the analytical method significantly underestimates the heat rate. Nevertheless, it can already be seen that, as

expected, the heat rate increases with the shortening of the tubes on top of the cryostat. It is also shown that an increase in the emissivity of the interior surface of the tubes helps reach the same order of magnitude for smaller tubes length.

Influence of tube characteristics on heat transfer through the top tubes

Next, to investigate the thermal impact of shortening the top tubes or increasing their diameter, the same ESATAN program is used to model radiative heat transfer under two extreme assumptions, perfectly diffuse and perfectly specular inner surface behavior. In reality, the inner surface of the tubes is neither fully diffuse nor fully specular, but its exact reflectivity characteristics are not known.

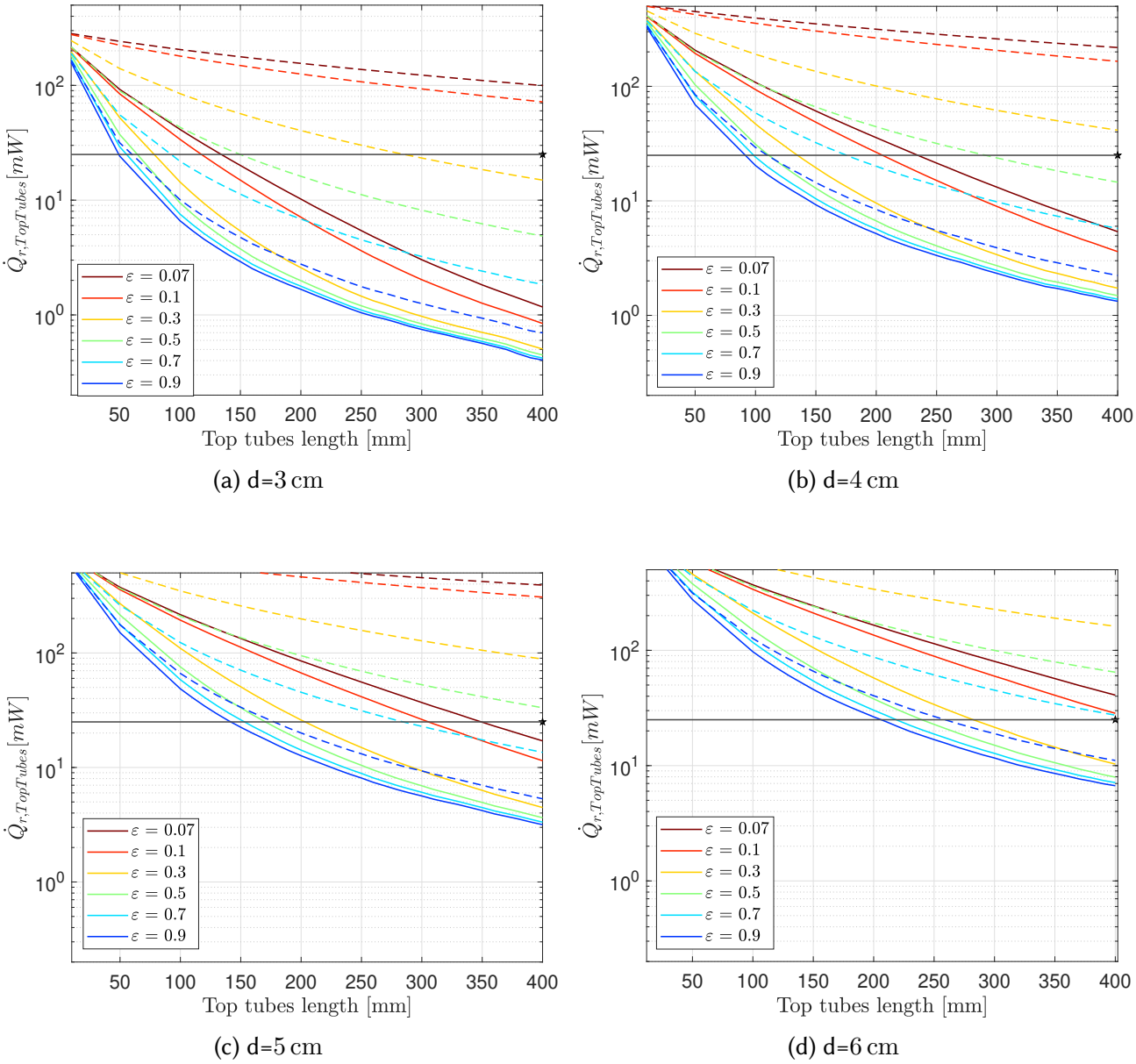

(a) d=3 cm

(b) d=4 cm

(c) d=5 cm

(d) d=6 cm

Figure 4.2: Evolution of the heat rate passing through the top tubes with tube lengths for various surface emissivities considering different tube diameter values. The solid lines assume diffuse inner tubes surface while the dashed lines assume fully specular inner tubes surface.

To account for this uncertainty, both limiting cases are presented in Figure 4.2, providing a conservative envelope for the expected heat rates. The completely diffuse radiation considerations are plotted with solid lines while the specular radiation considerations are shown in dashed lines. Additionally, a star marker indicates the estimated heat transfer for the actual prototype configuration. This value is around $25\,\mathrm{mW}$, considering a copper surface emissivity of 0.07[23], a tube diameter of $3\,\mathrm{cm}$ and a tube length of $40\,\mathrm{cm}$. This value corresponds to half the total heat rate through all six tubes as reported in the reference study[13], considering that only the three top tubes are analyzed here because these are the most critical due to cable routing constraints.

For clarity, a horizontal line representing this estimated heat rate is also plotted. This allows for a direct visual comparison and helps identify which tube geometries remain within the acceptable thermal budget.

It can be seen in the figures that, for different tube diameters, reducing the length of the tubes requires an increase in the interior surface emissivity to maintain the same heat load through the top tubes, to remain below or on the reference horizontal line.

For example, in Figure 4.2a, it can be seen that if it is necessary to reduce by half the tubes length to facilitate the assembly of the prototype, the tubes should be painted with a paint that yields an emissivity of at least 0.5. Note that this is a conservative condition as both the diffuse and specular radiation curves are below the horizontal line at this emissivity but it can not be asserted with certainty that an emissivity of 0.3 would be sufficient as the percentage of specularity is unknown.

Another parameter to look at, in order to make assembly easier, is increasing the tube diameter. This parameter also increases greatly the heat rate passing through the tubes. Indeed, considering again tubes of half the initial length, that is of $200\,\mathrm{mm}$, it can be seen in Figure 4.2b that if the diameter increases by $1\,\mathrm{cm}$, then interior surface coat must reach an emissivity of 0.7 to ensure that the heat rate is bellow the limit for any specular-diffuse radiation ratio. This emissivity value seems reachable as the paint applied on the actual prototype fins is already assumed to reach and emissivity of 0.65[13]. Considering now a diameter of $5\,\mathrm{cm}$, Figure 4.2c shows that the emissivity has to increase to 0.9 to ensure to be under heat rate limit. Lastly, with a diameter of $6\,\mathrm{cm}$ any value of inner surface coating emissivity is sufficient to ensure that the heat rate stays under the limit, even for a completely diffuse surface, as presented in Figure 4.2d.

Design adaptations of the GHe and LN_2 thermal plates for the inner surface coating of the tubes

To allow high-emissivity paint coating of the inner surfaces of the tubes located on the top side of the thermal insulation layers, it is necessary to open the tubes in two halves.

Additionally, for easier assembly, it is preferable to fix the tubes to the insulation plates before installation. To enable this, an alternative cutting pattern of the thermal insulation plates is required. The new design links the plate cuts with the cuts of the tubes.

An alternative cut of each of the thermal shield that enables this approach is shown in Figure 3.13.

In practice, only the inner tubes, those connected to the GHe plate, are painted to increase their inner surface emissivity. The corresponding new GHe plates and tubes cut is shown in Figure 4.3b. However, the LN2 tubes are also cut using the same method, as depicted in Figure 4.3b. This facilitates the overall assembly process, even though these tubes are not painted.

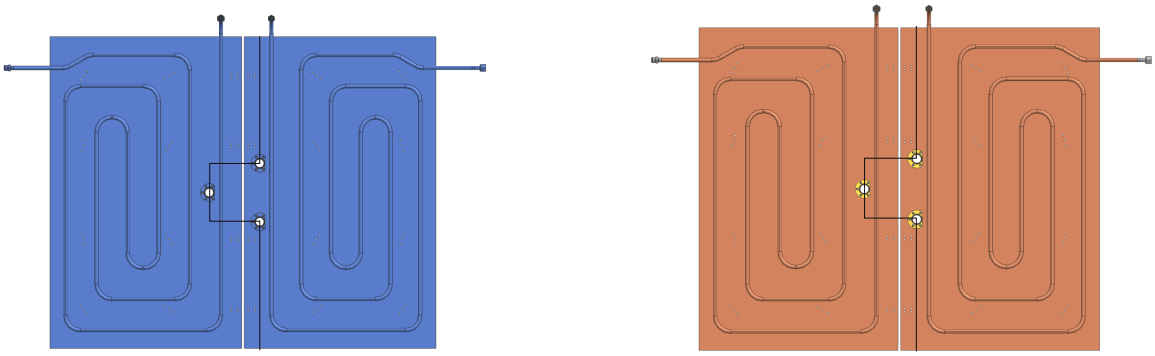

(a) GHe top plates and corresponding top tubes.

(b) LN2 top plates and corresponding top tubes.

Figure 4.3: Alternative cut of the thermal insulation top plates and corresponding top tubes, shown in dark.

4.1.2 Alternative assembly process

As mentioned in Section1.2.1, the current E-TEST assembly process is complex, involving multiple assembly, disassembly, and reassembly steps for the inverted pendulum structure. This section proposes an alternative method to simplify the procedure without modifying the prototype. The main assembly steps, illustrated in Figure 4.5 are roughly the same. However, in this new approach, the inverted pendulum is assembled only once. In addition, the outer cryostat and the top thermal layers are installed differently.

First, as in the original procedure, the fins, fin frames, and inner frame are cleaned and assembled. Then they are integrated into the inner cryostat structure, which includes the cold platform. However, unlike the original procedure, the intermediate frame that can be seen in Figure 1.5a is not yet assembled at this stage, only the bottom one with the bottom thermal isolation shields is already assembled. This is illustrated in Figure 4.5a.

Next, the inverted pendulum legs are assembled to support the top platform from which the mirror is suspended, as shown in Figure 4.5b. In contrast to the initial procedure, this is a permanent assembly, the inverted pendulum will not be later disassembled.

After that, the external fins structure must be installed, closely surrounding the internal set of fins. A challenge arises because the external fins form a rectangular enclosure, while the inverted pendulum legs are arranged in a triangular configuration. As a result, it is not possible to insert all sides of the external structure in a straightforward manner, without first dismantling the pendulum.

To avoid this, a specific assembly sequence, presented in Figure 4.5c is followed using gantry canes and a temporary external structure. Instead of placing all sides directly, some of them must be carefully slid into position to navigate around the pendulum legs.

The detailed steps for assembling the outer cryostat are shown in Figures 4.5d, 4.5e, 4.5f, and 4.5g. In this series of figures, the inner cryostat is partially transparent to highlight the outer structure. Additionally, the short and long fins sides are temporarily highlighted in yellow and purple respectively, for a better visibility. Figure 4.5d, shows the final position of the first side of the outer cryostat. It has to be slid into place carefully to avoid contact with the tubes in front of the mirror and the inverted pendulum leg behind. Once in position, an external structure, modeled in blue, is installed to hold this side in place during the rest of the assembly. The second side is then slid into position and fixed to the first side using bracket. This can be seen in Figure 4.5e. The third side is installed similarly, as depicted in Figure4.5f. Lastly, the fourth side is placed directly since no pendulum leg obstructs its path. This step is shown in Figure 4.5g. Lastly, once all sides are attached to each other and to the bottom frame, the blue external structure is removed. This leads to Figure 1.5c

After all sides are in place and sealed together, the top thermal shields, including the LN_2 and GHe top plates, are installed, completing the enclosure shown in Figure4.5h. Given that the thermal shields are cut as illustrated in Figures4.3a and 4.3b, these top layers can also be inserted without dismantling the inverted pendulum. One part slides straight in, while the other has to move straight and then move a little bit to the left to reach the other part as displayed in Figure 4.5i.

Gantry Crane and Counter Weights

To assemble the outer cryostat, a gantry crane and counterweights are used. Indeed, the fins of the IRHX and the ERHX are positioned very close to each other, but any contact between them must be strictly avoided. Therefore, each side must be horizontally moved with high precision during installation.

The sides of the ERHX are installed using similar counterweight structures as in the first assembly process version except that they must be slightly adapted to take into account the additional weight of the intermediate frame as it is directly mounted on the ERHX sides. In addition, the motion of the gantry crane must be adapted as explained above and shown in Figure 4.5i.

A key difference from the previous assembly method lies in how the top panels of the ERHX and the thermal insulation shields are installed. In this version, both components are inserted together using a horizontal sliding motion. They are guided into place through the narrow gap between the top of the intermediate frame and the marionette, which blocks direct vertical access. As a result, the gantry crane is mounted to the side to carry out the operation.

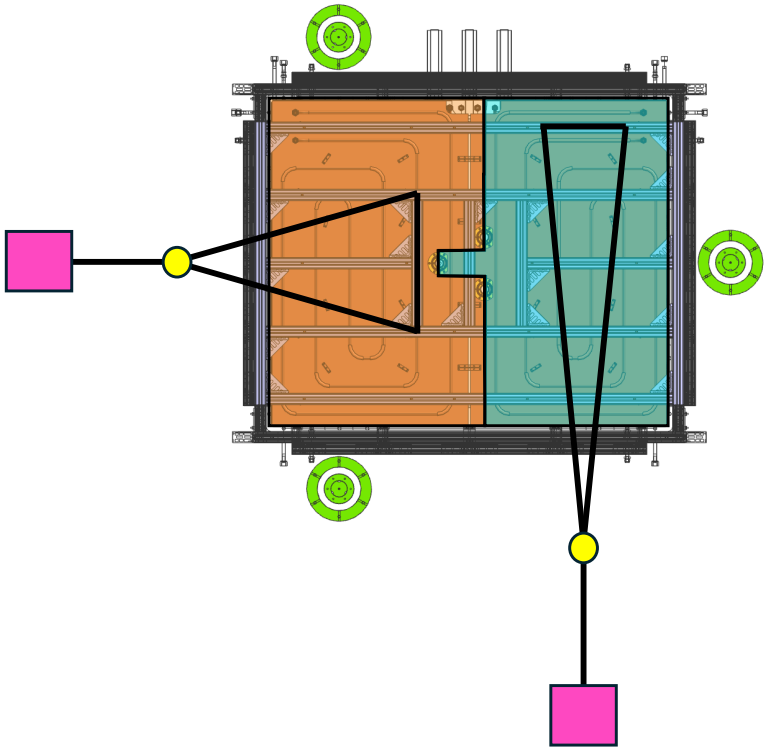

Figure 4.4: Scheme of the structures used to hold and slide the top plates (in orange and blue). The counterweights are shown in pink while the gantry crane attachment point is shown in yellow.

This horizontal insertion requires a redesigned counterweight system. The legs of the counterweight structures are positioned in the plane of the top frame and are directly attached to it, while the gantry crane attachment point, is located completely outside of the cryostat structure. The counterweights, shown in pink, are carefully placed and dimensioned to balance the weight of the

top plates, ensuring that they remain horizontally oriented during installation. A top view of this setup is shown in Figure 4.4.

It is important to note that assembling the top plates with the top tubes already attached is only possible if the tubes are shortened. However, it has been demonstrated earlier in this chapter that it was possible to shortened the tube length by two without affecting the thermal performance of the cryostat, if their interior surfaces are painted in high emissive black paint.

In this specific case, it has been verified through geometry checks that there is enough space to slide the full length of the tubes through the gap between the marionette and the top of the intermediate frame. Indeed, even though only part of the tubes will stick out of the cryostat after installation, the full length must pass through this narrow space during the sliding process. This verification leads to a clearance value of about $5\,\mathrm{cm}$ for the assembly, which is considered sufficient to carry out the procedure safely.

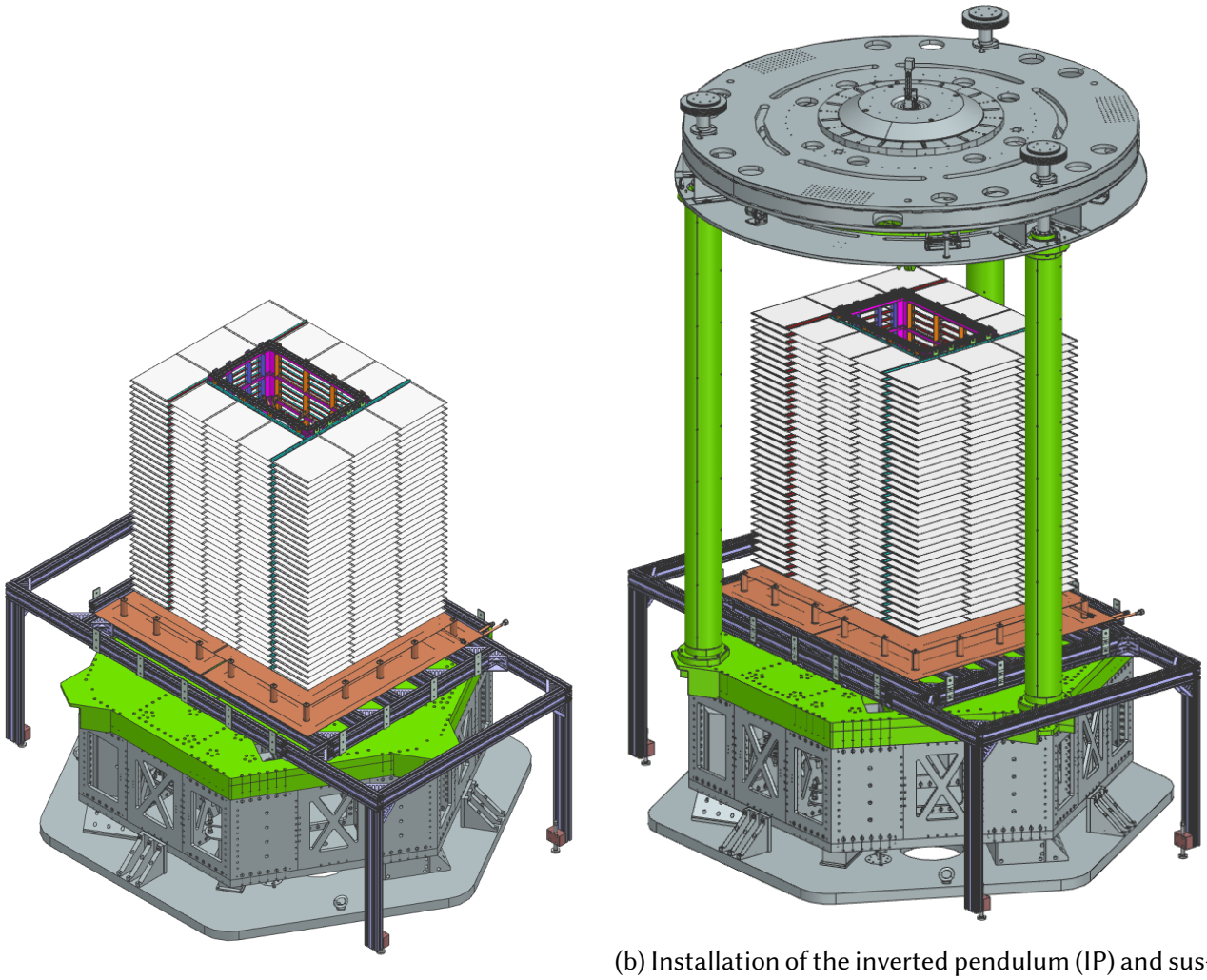

(a) Assembly of the inner cryostat.

(b) Installation of the inverted pendulum (IP) and suspension of the payload to the marionette.

Figure 4.5: NX modelisation of the main steps of the new assembly method for the E-TEST prototype.

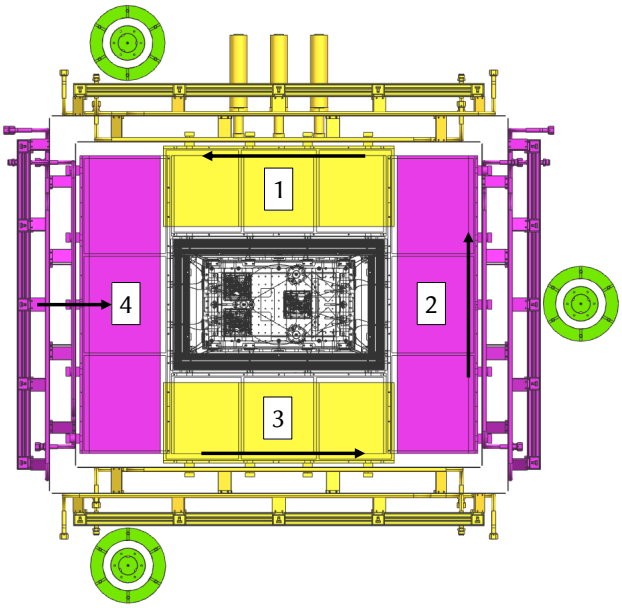

(c) Order and direction in which the sides of the outer cryostat, including the thermal barriers, are slipped into place.

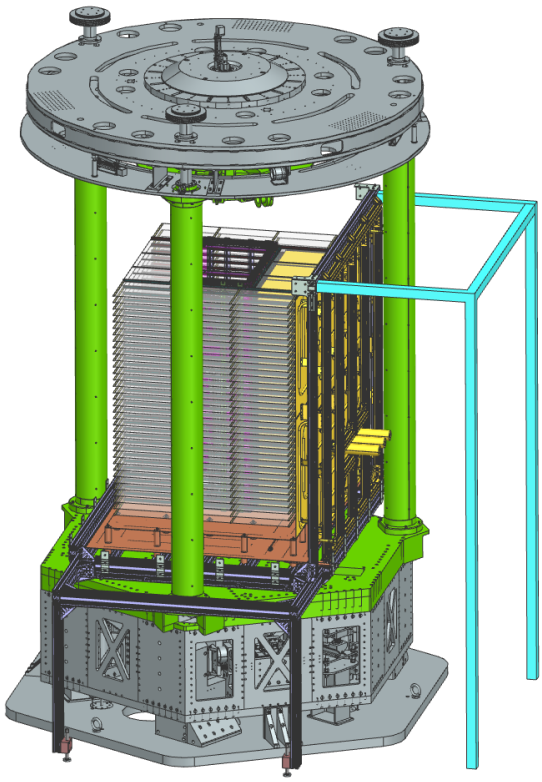

(d) Installation of the outer cryostat first side, shown in yellow, and the external support structure, highlighted in blue.

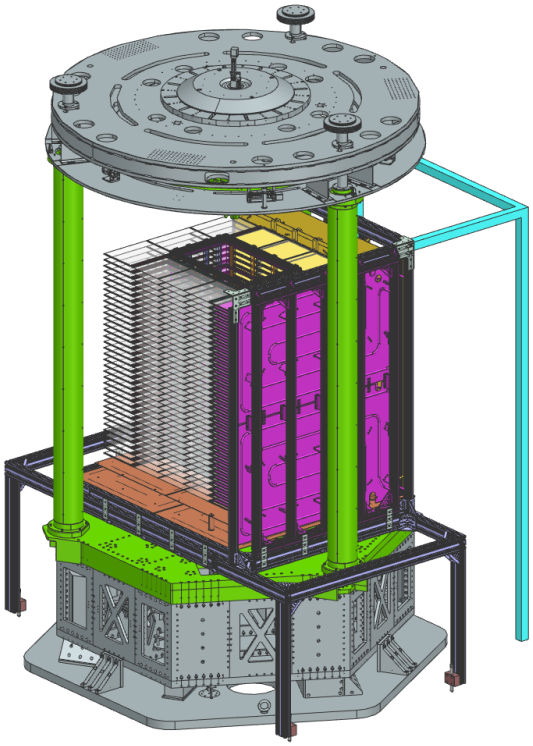

(e) Insertion of the second side of the outer cryostat.

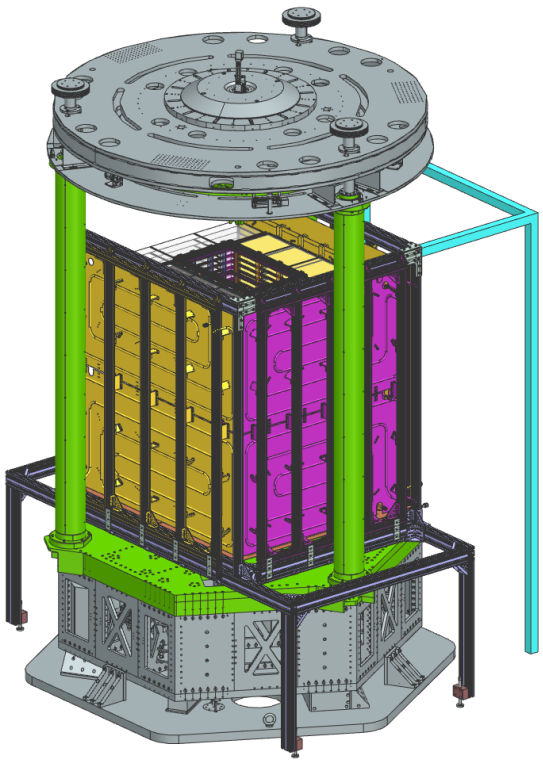

(f) Installation of the third outer cryostat side.

Figure 4.5: NX modelisation of the main steps of the new assembly method for the E-TEST prototype.

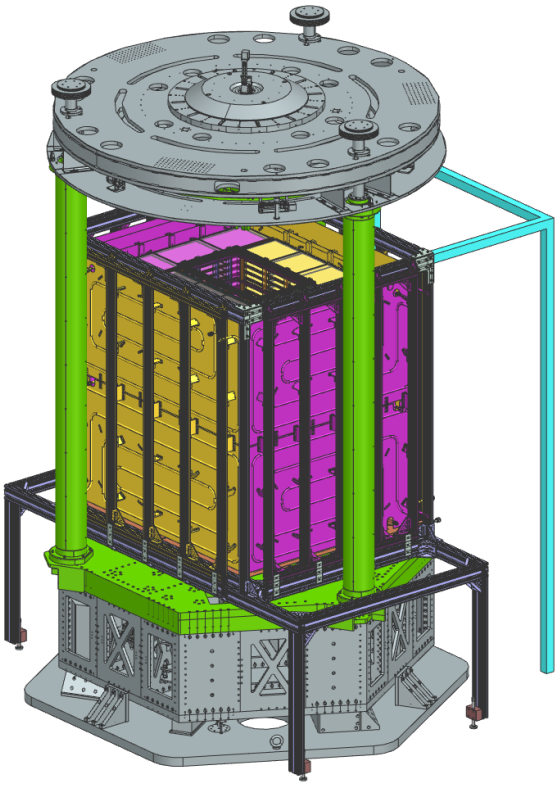

(g) Insertion of the last side of the outer cryostat.

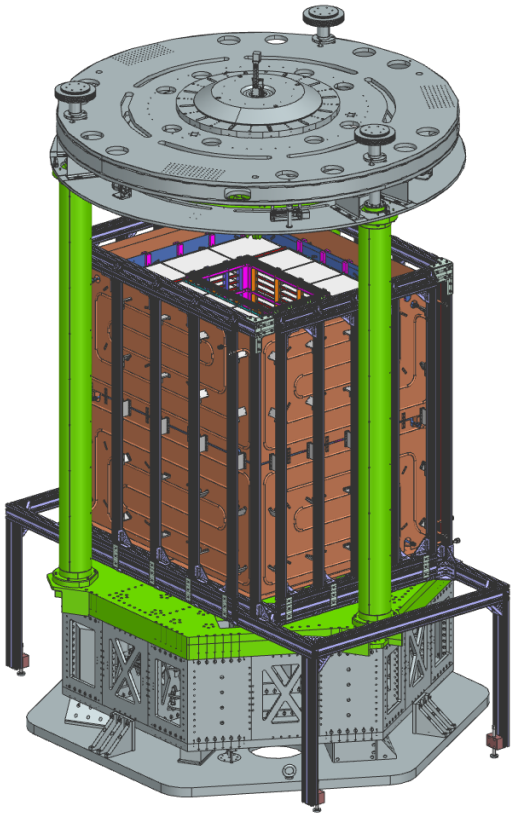

(h) End of the outer cryostat assembly and disconstruction of the external support.

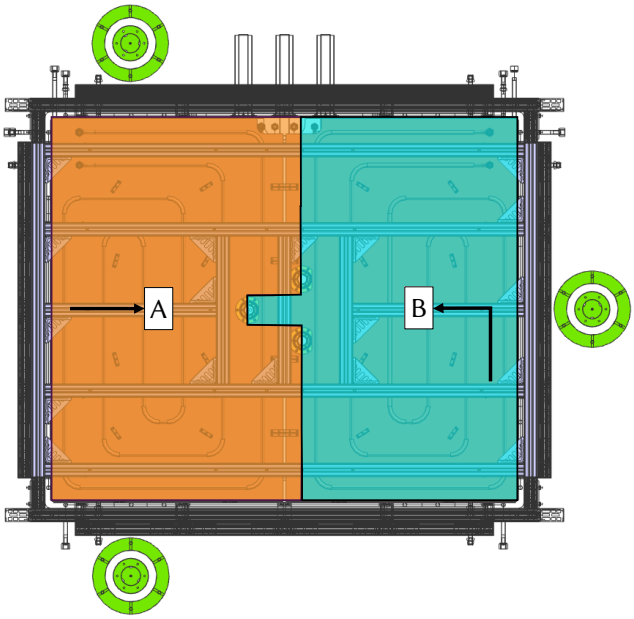

(i) Direction in which the top plates are mounted, with a highlight of the new cut of these plates.

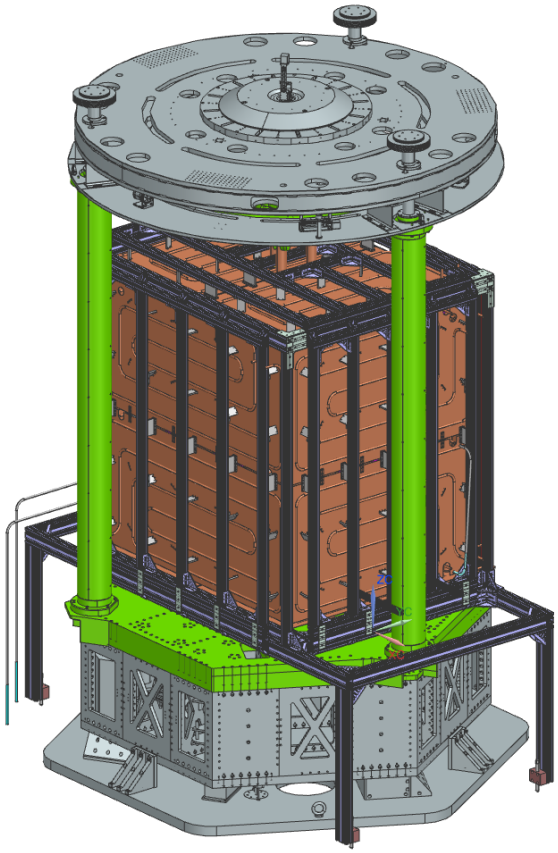

(j) Complete CAD model of the assembled E-TEST prototype.

Figure 4.5: NX modelisation of the main steps of the new assembly method for the E-TEST prototype.

4.2 High-Complexity Improvements

After implementing simpler modifications that improve both the assembly and performance of the prototype, this section investigates more advanced changes that could further enhance the design. First, it presents a complete redesign of the RHX architecture. Then, it examines the impact of alternative fin shapes.

4.2.1 Alternative RHX designs

A potential improvement consists in redesigning the RHX to facilitate assembly and optimize the allocated space. As previously mentioned, the current RHX forms a rectangular structure that must fit within the triangular space defined by the IP legs. This configuration is difficult to assemble and leaves unused volume in the cryostat. Therefore, alternative fin geometries are explored to determine whether the existing design is truly optimal.

New RHX design options

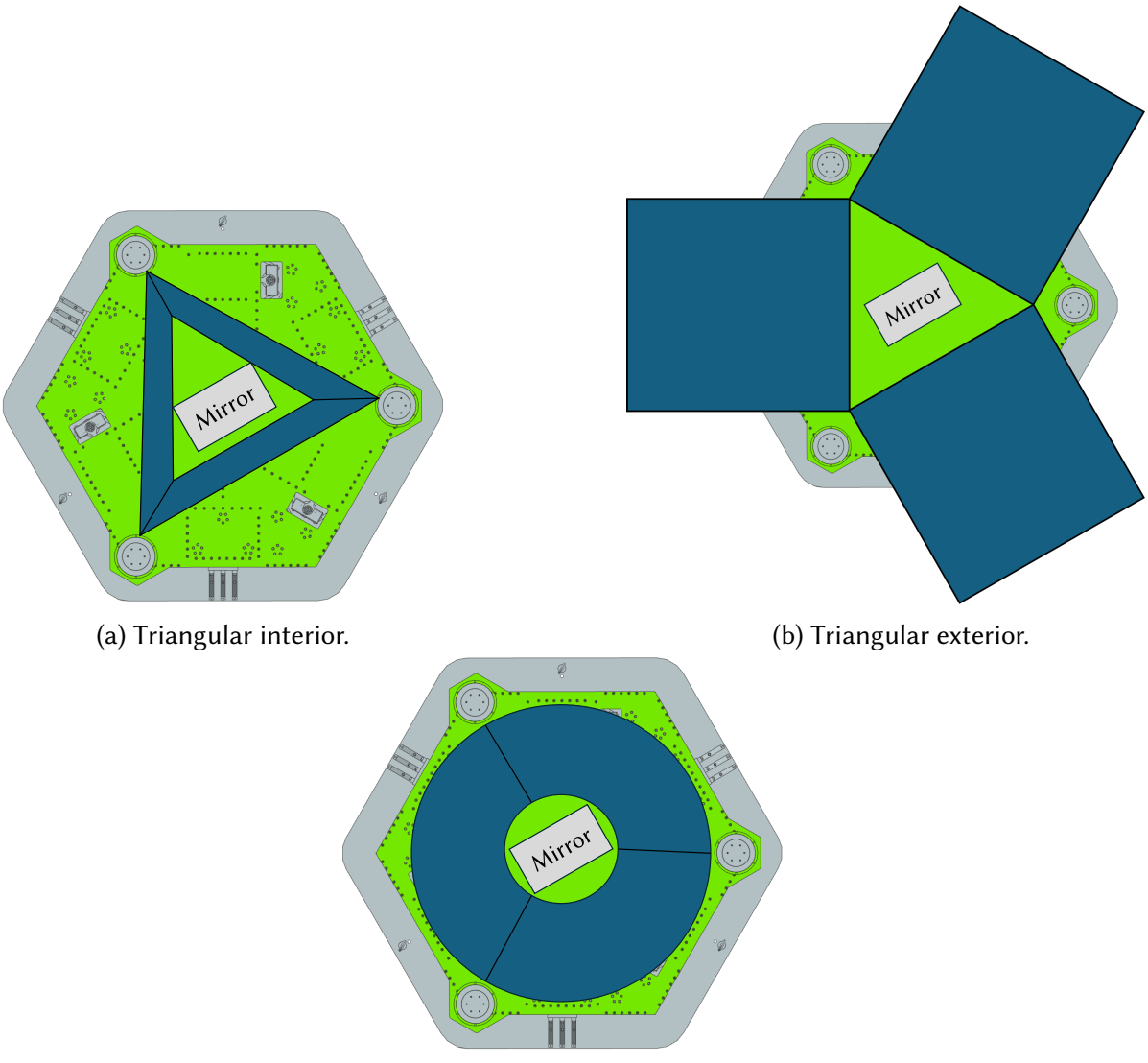

(a) Triangular interior.

(b) Triangular exterior.

(c) Circular.

Figure 4.6: Drafts of the RHX design options.

To make the best use of the space available for the cryostat, which is limited by the triangular shape formed by the inverted pendulum legs, and to make the assembly process easier, several new designs for the fin support structure are studied.

The most obvious idea is to use a triangular base. This would allow the external fin set to be inserted without disassembling the inverted pendulum. Two design options are explored.

The first option is to make the internal and external shape of the RHX structure triangular. This configuration is roughly shown in Figure 4.6a. The blue area shows the allocated space for the fins. As the sketch suggests, this design is not optimal, even if it would greatly simplify the assembly procedure. Actually, it leaves very little room for the fins due to the sharp corners and narrow areas between the pendulum legs.

The second triangular configuration uses rectangular fins units placed between the legs of the inverted pendulum. Together, these parts form a triangular geometry around the mirror cage, as shown in Figure 4.6b. This enables to dedicate more space for the fins. However, it also increases the distance between some mass elements and the suspension point of the overall inner cryostat structure, which may reduce overall stability. Indeed, even a small change in the IRHX position could move its center of gravity and cause instability. In addition, it is not ideal for the fins structure to extend far beyond the platform, since the test is performed inside a $3\,\mathrm{m}$ diameter circular vacuum chamber.

Finally, a circular fin structure is considered. This design is shown in Figure 4.6c. Both the IRHX and the ERHX structures follow a circular layout, resulting in a ring-shaped configuration. This shape is then divided into three equal segments to simplify the assembly process.

This configuration allows for a larger surface area to be covered between the mirror and the inverted pendulum legs. It also facilitates the insertion within the circular vacuum chamber, on the contrary to the configuration outlined in Figure 4.6b. This design can also be easily adapted to the constraints of the Einstein Telescope cryostat, because it is itself limited by circular thermal shields.

Therefore, among other options, the circular fin design is chosen for the current study and is thus further discussed below.

Circular RHX with horizontal fins design

The design begins by estimating the total radiative heat transfer area A_{IRHX} required to maintain the target payload temperature $T_{mirror} = 22\,\mathrm{K}$, assuming a sink temperature of $T_{ERHX} = 15\,\mathrm{K}$, while dissipating a heat rate $\dot{Q}_{parasit} = 360\,\mathrm{mW}$. In the case of E-TEST, the IRHX temperature is assumed to be approximately the mirror temperature, that is $T_{IRHX} = T_{mirror} = 22\,\mathrm{K}$. In the case of E-TEST, the IRHX temperature is assumed to be equal to the mirror temperature, that is $T_{IRHX} = T_{mirror} = 22\,\mathrm{K}$. This simplification is acceptable at this early stage of the design, based on the small temperature difference observed between these components in the current prototype, as shown in Table 3.14.

The fins are assumed to be large, diffuse, opaque and gray, with an emissivity $\varepsilon_{RHX} = 0.65$ [13]. In addition, the view factor between two facing fins is assumed to be unity. Therefore, using Equation 2.5 the total required IRHX radiative surface area is

$$A_{IRHX} = \dot{Q}_{parasit} \frac{(2 - \varepsilon_{RHX})}{\varepsilon_{RHX}\sigma} \frac{1}{T_{IRHX}^4 - T_{ERHX}^4} = 71.8[m^2]. \tag{4.2}$$

Next, the maximum number of horizontal fin layers that can be placed inside the cryostat is determined. This is done using a method similar to the one applied to the current prototype. In this

particular configuration, a fin layer refers to a group of three parallel fins placed side by side at the same height, forming a ring-shaped configuration.

The maximum number of horizontal fin layers depends on the total available height in the cryostat, $h_{cryostat} = 1.5\,\mathrm{m}$, the space margin between two facing fins, $h_{sm} = 2\,\mathrm{cm}$, and the thickness of the fins, $h_{thickness} = 3.5\,\mathrm{mm}$. It is expressed as

$$N_{Hfins} = \left\lfloor \frac{h_{cryostat}}{2h_{sm} + h_{thickness}} + 1 \right\rfloor = 35 \text{ fins.} \tag{4.3}$$

The numerical values used in the above equation are taken from the current E-TEST cryostat parameters [13].

It is important to note that $h_{cryostat} = 1.5\,\mathrm{m}$ differs from the height $h_{ETEST} = 2.35\,\mathrm{m}$ reported in Table 1.1. In fact, the former represents the height that can be fully occupied by the fins. It is therefore smaller than the latter, in order to leave additional space for the portion of the top tubes extending beyond the main cryostat structure, as well as for the assembly margin, as previously mentioned.

The area associated with a single fin layer, A_H is then obtained from

$$A_H = \frac{1}{2}\frac{A_{IRHX}}{N_{Hfins}} \approx 1\,\mathrm{m}^2. \tag{4.4}$$

Once this area is known, the detailed fin geometry can be determined by specifying a single parameter, either the internal radius, r_{int}, or the external radius, r_{ext}. These radii must satisfy the condition

$$r_1 = 0.35\,\mathrm{m} < r_{int} < r_{ext} < r_2 = 1\,\mathrm{m}, \tag{4.5}$$

where, r_1 and r_2 are the cryostat limits introduced earlier in Figure 1.7a.

For a better visualization and understanding, the main dimension parameters used to design the fins are shown in Figure 4.7.

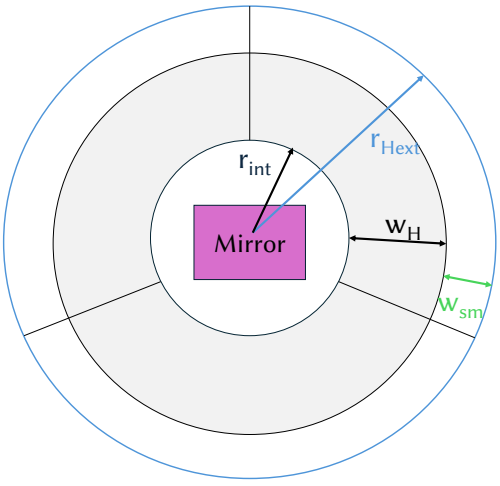

Figure 4.7: Dimension parameters of the horizontal circular fins and its structure

The width w_H, is calculated using the internal radius and the fin layer area. The external radius is

then obtained by adding a safety margin, $w_{sm} = 2\,\mathrm{cm}$. The expression used are

$$w_H = \sqrt{r_{int}^2 + \frac{A_H}{\pi}} - r_{int}, \tag{4.6}$$

$$r_{Hext} = r_{int} + w_H + w_{sm} = \sqrt{r_{int}^2 + \frac{A_H}{\pi}} + w_{sm}. \tag{4.7}$$

This leads to an almost linear relation between the internal and external radius of the circular fins. Therefore, to minimize the overall space occupied, the fins should be positioned as close as possible to the mirror cage.

A simplified CAD representation of this cryostat configuration is shown in Figure 4.8. The fins appear in light gray, while GHe and LN_2 thermal insulation layers are shown in blue and brown, respectively. Moreover, in this representation, only two of the three parts of the cryostat are assembled to provide a clearer view of the fins. The parameters used for this model are listed in Table 4.1. This table is divided into three parts. The first set recalls the thermal characteristics, including payload and sink temperatures, fin emissivity, and heat to dissipate. The second group includes geometric parameters and spacing values known from the current prototype. The last set presents the resulting design parameters used in the CAD model.

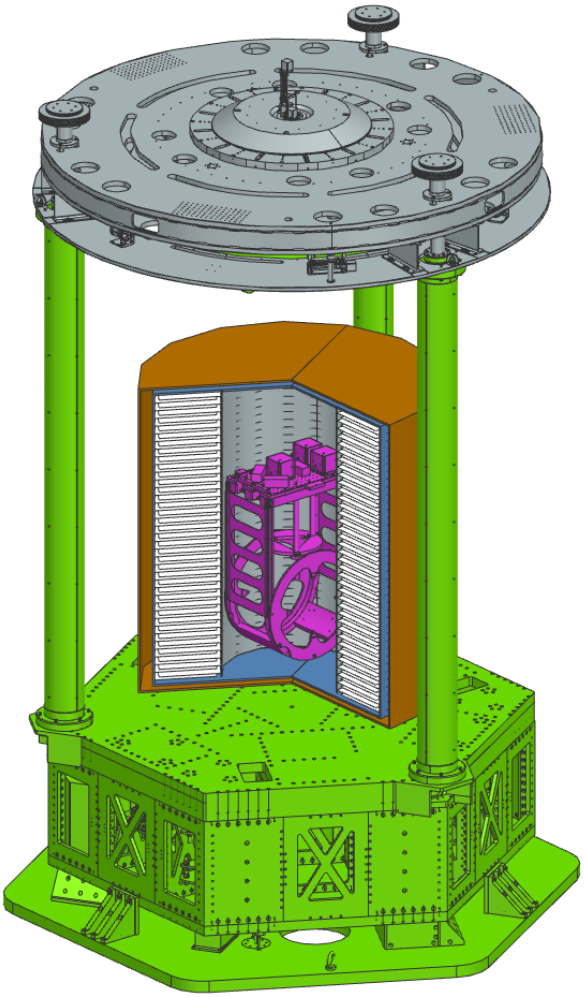

Figure 4.8: NX CAD of one circular RHX with horizontal fins configuration, following the design parameters presented in Table 4.1.

Parameters	Circular Horizontal Fins Configuration
T_{ERHX}	15 K
T_{IRHX}	20 K
ε_{RHX}	0.65
$\dot{Q}_{parasit}$	360 mW
$h_{cryostat}$	1.5 m
$h_{thickness}$	3.5 mm
h_{sm}	2 cm
w_{sm}	2 cm
N_{Hfins}	35
r_{int}	0.35 m
w_H	32 cm
r_{Hext}	0.7 m

Table 4.1: Parameters of one circular horizontal fins configuration.

Circular RHX with vertical fins design

Another option to use the ring-shaped RHX structure is to place the fins vertically rather than horizontally. In this case, the fins take the form of rectangular panels, placed circumferentially around the internal and external perimeters of the RHX structure. This simplifies the manufacturing process, as rectangular fins are easier to fabricate compared to circular ones.

Unlike the horizontal configuration, the maximum number of vertical fins that can be installed depends directly on the internal radius r_{int}, which must still respect the condition defined in Equation 5.6. The expression for the maximum number of vertical fins is

$$N_{Vfins} = \left\lfloor \frac{2\pi r_{int}}{2h_{spacing} + h_{thickness}} \right\rfloor . \tag{4.8}$$

Each fin again has two radiating surfaces, so the surface area per vertical fin is

$$A_V = \frac{1}{2}\frac{A_{IRHX}}{N_{Vfins}}, \tag{4.9}$$

with $A_{transfer}$ that is the same as in Equation 4.2, since the required total radiative area is independent of the fin orientation and design. Knowing the area of the fin, the detailed design of the vertical fins can be calculated using the internal radius of the circular fin structure, r_{int}. Like in the horizontal case, the parameters used to design the fins and the circular RHX structure are shown in Figure

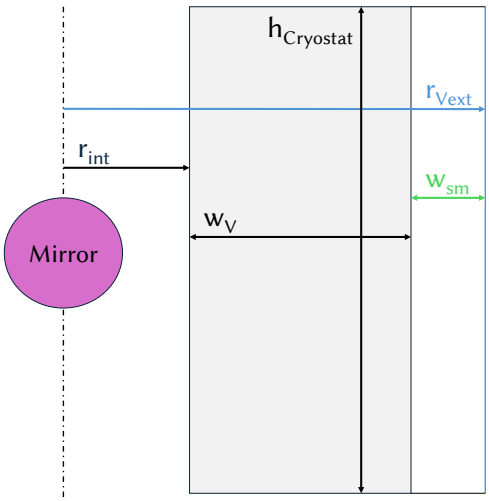

Figure 4.9: Dimensional parameters of the vertical fins and corresponding RHX circular structure.

Given the rectangular geometry of the fins and the vertical limitation imposed by the cryostat height, the width of each vertical fin is

$$w_V = \frac{A_{Vfins}}{h_{cryostat}}, \tag{4.10}$$

with $h_{cryostat} = 1.5\,\mathrm{m}$ as in the previous case. The external radius is then

$$r_{Vext} = r_{Vint} + w_V + w_{sm} \sim r_{Vint} + \frac{\frac{1}{2}A_{IRHX}(2h_{spacing} + h_{thickness})}{h_{cryostat}\ 2\pi\ r_{Vint}} + w_{sm}. \tag{4.11}$$

As it can be seen in Equation 5.12, unlike in the horizontal case, the relation between the external and internal radius of the vertical fins structure is not linear anymore. Therefore, an increase in the internal radius does not always lead to an increase in the external radius. This is illustrated in Figure 4.10, which compares two designs with different internal radii. In addition, Table 4.2 compares these two configurations in terms of the number of fins, their widths, and the external radius. The first case shown in Figure 4.10a, uses a smaller internal radius, $r_{int} = 0.35\,\mathrm{m}$, but requires a larger external radius. The second case, presented in Figure 4.10b, with $r_{int} = 0.4\,\mathrm{m}$, allows for narrower fins and a smaller r_{ext}. This happens because a larger perimeter allows more fins, and therefore, each fin can be narrower while still meeting the total radiative required surface. This shows that the most space-efficient design is not always the one with the smallest r_{int} for the vertical fins configuration.

Parameters	$\mathbf{r_{int}} = 0.35\,\mathrm{m}$	$\mathbf{r_{int}} = 0.4\,\mathrm{m}$
$N_{V fins}$	54	62
$w_{V fins}[cm]$	45	38
$r_{ext}[m]$	0.82	0.8

Table 4.2: Comparison of two vertical fins configurations parameters with a smaller and a larger internal radius, illustrating the impact of r_{int} on fin width and external radius.

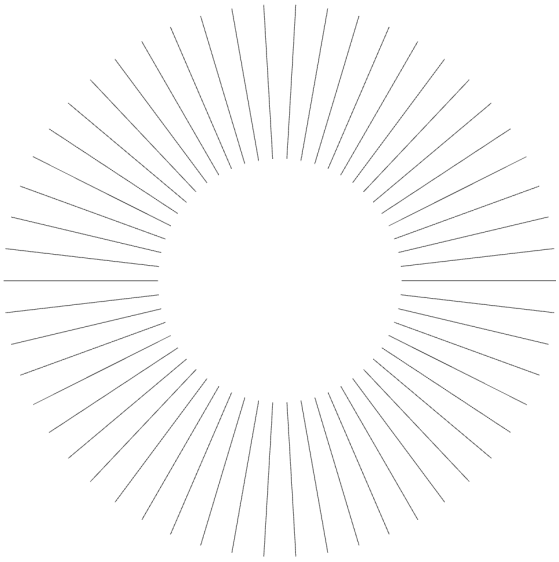

(a) Vertical interior fins configuration with smaller internal radius, $r_{int} = 0.35\,\mathrm{m}$.

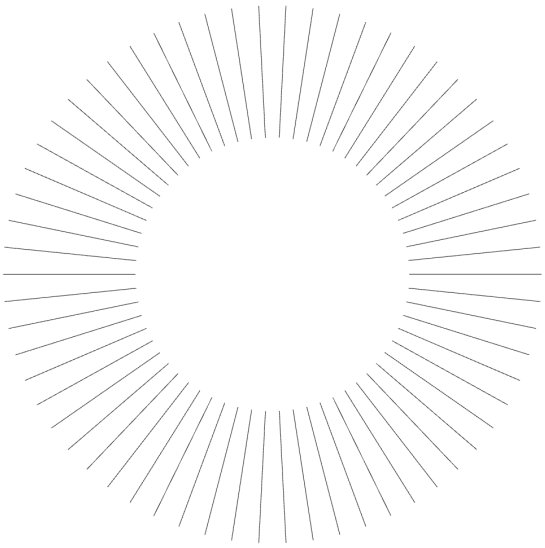

(b) Vertical interior fins configuration with larger internal radius, $r_{int} = 0.4\,\mathrm{m}$.

Figure 4.10: Comparison of two vertical fins configurations with different internal radii, illustrating the impact of r_{int} on fin width and external radius.

A simplified CAD model of the cryostat incorporating vertical fins is illustrated in Figure 4.11. The parameters used for this model are listed in Table 4.3 and are organized in the same way as for the horizontal configuration.

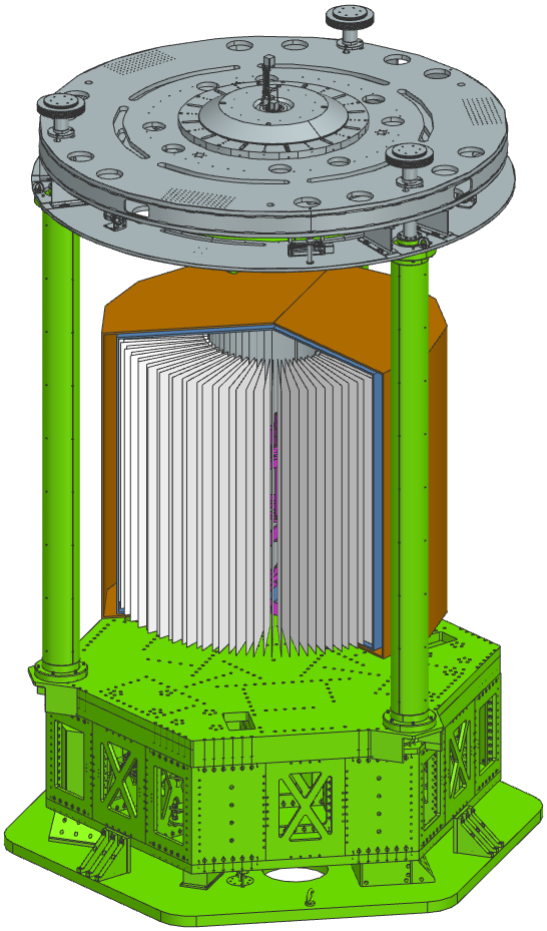

Figure 4.11: NX CAD of one circular vertical fins configuration, following the design parameters presented in Table 4.3.

Parameters	Circular Vertical Fins Configuration
T_{ERHX}	15 K
T_{IRHX}	20 K
ε_{RHX}	0.65
$\dot{Q}_{parasit}$	360 mW
$h_{cryostat}$	1.5 m
$h_{thickness}$	3.5 mm
h_{sm}	2 cm
w_{sm}	2 cm
N_{Vfins}	50
r_{int}	0.35 m
w_{Vfins}	48 cm
r_{Vext}	0.85 m

Table 4.3: Parameters of one circular vertical fins configuration.

Comparison of the two circular RHX designs

Now that both circular RHX configurations have been defined, a comparative analysis is performed to identify the most suitable option.

The first element that could be compared is the space taken by the RHX. To do so, Figure 4.12 presents the variation of the external radius, r_{ext}, as a function of the internal radius, r_{int}. The blue curve corresponds to the vertical fins configuration, while the black curve represents the horizontal fins configuration. Moreover, a horizontal dashed red line is drawn at the upper limit for the external radius of the RHX, $r_{ext} = r_{2,ETEST} = 0.85$. A green-shaded area also highlights the range of acceptable values for the internal and external RHX radii.

It can be seen in this figure that for the horizontal fins configuration, r_{ext} increases almost linearly with r_{int}. In contrast, the vertical configuration exhibits a minimum in the curve, marked with a point. This minimum corresponds to an optimal configuration in which the smallest external radius, $r_{ext} \approx 0.84\,\mathrm{m}$, is achieved for $r_{int} \approx 0.41\,\mathrm{m}$. It can also be seen that for any internal radius considered, the horizontal fin configuration enables a more compact cryostat compared to the vertical fin configuration.

However, for the E-TEST prototype, spatial constraints are not a limiting factor for either configuration. The vertical configuration remains within the allowable external radius limit up to $r_{int} \approx 0.5\,\mathrm{m}$, and the horizontal configuration remains compliant up to $r_{int} \approx 0.6\,\mathrm{m}$. Therefore, both configurations are viable when considering spatial constraints alone.

Manufacturability is another key consideration. Rectangular fins, as used in the vertical configuration, are significantly easier and more cost-effective to fabricate compared to circular fins. This practical advantage favors the vertical design.

Moreover, one should consider the impact of mechanical bending. In the vertical configuration, gravitational forces are aligned with the fin orientation, which reduces its bending. Therefore, less safety margin between the fins could be considered for the vertical configuration compared to the horizontal one.

In conclusion, for the design of a new cryostat, the circular RHX with vertical fin configuration, corresponding to the marked point in Figure 4.12, appears to be the most advantageous option. It offers a good compromise between spatial efficiency, limited fin bending, and ease of manufacturing. This conclusion is valid under current assumptions, in particular, that the fin thickness is similar to that of the existing cryostat. However, fin thickness is a key parameter, and its impact is examined in the next section.

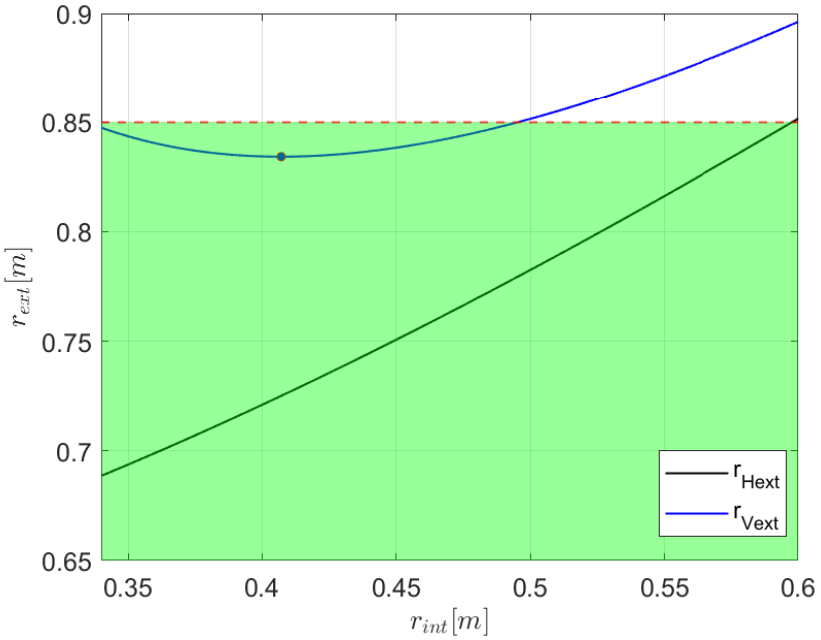

Figure 4.12: Evolution of the external radius of with the internal radius of the RHX, assuming fin emissivity and thickness of $\varepsilon_{RHX} = 0.65$ and $h_{thickness} = 3.5\,\mathrm{mm}$ respectively. The black curve represents the horizontal fins configuration and the blue curve the vertical fins configuration with its minimum external radius marked with a point. An horizontal dotted line is plotted at the cryostat external radius limit and a green rectangle show the acceptable configurations region.

Circular RHX designs for various fin thickness and emissivity

In the current E-TEST prototype, the fins are made from thin aluminum sheets, reinforced and painted black. This results in a fin thickness of $h_{thickness} = 3.5\,\mathrm{mm}$ and an emissivity of $\varepsilon_{RHX} = 0.65$. In the previous section, new circular RHX designs were introduced, using the same thickness and emissivity values.

However, alternative methods to increase fin emissivity are being investigated. These include using a more emissive coating or changing the fin shape from flat to corrugated or honeycomb, which could also reduce the fin bending. These changes despite increasing the emissivity would increase the fin thickness. Therefore, it is important to check whether the new RHX designs remain compatible with cryostat constraints for different thicknesses and emissivities.

To study how different fin thicknesses and emissivities affect circular RHX designs, several cases are shown in Figure 4.13.

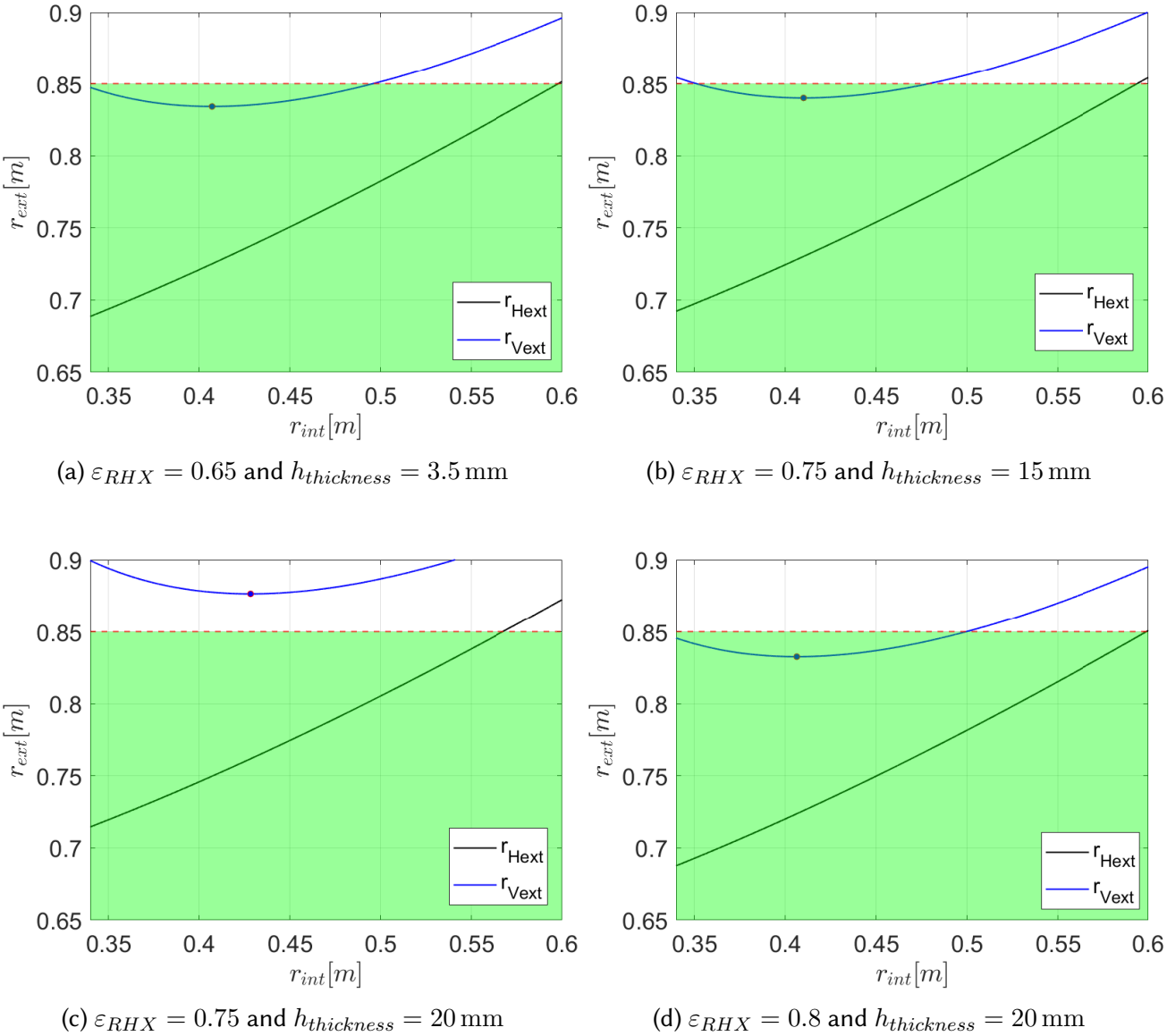

(a) $\varepsilon_{RHX} = 0.65$ and $h_{thickness} = 3.5\,\mathrm{mm}$

(b) $\varepsilon_{RHX} = 0.75$ and $h_{thickness} = 15\,\mathrm{mm}$

(c) $\varepsilon_{RHX} = 0.75$ and $h_{thickness} = 20\,\mathrm{mm}$

(d) $\varepsilon_{RHX} = 0.8$ and $h_{thickness} = 20\,\mathrm{mm}$

Figure 4.13: Evolution of the external radius of the circular RHX with its internal radius for different fin emissivities and thicknesses. The black curve represents the horizontal fins configuration and the blue curve the vertical fins configuration with its minimum external radius marked with a point. An horizontal dotted line is plotted at the cryostat external radius limit and a green rectangle show the acceptable configurations region.

Figure 4.13a recalls the original curves from the first circular RHX designs, presented in Figure 4.12 and discussed previously. If the honeycomb structure results in a fin thickness of $15\,\mathrm{mm}$ and an emissivity of 0.75, the new curves, shown in Figure 4.13b, lead to the same discussion between the horizontal and vertical fin configurations, even though both curves are slightly shifted up.

In contrast, if the fin thickness increases to $20\,\mathrm{mm}$, an emissivity of 0.75 is not sufficient to keep the vertical fin configuration as the best choice, since the blue curve is completely out of the green zone. In this case, an alternative solution could be considered, such as the triangular exterior RHX structure shown in Figure 4.6b, although not detailed in this paper. This geometry offers additional space by extending beyond the area enclosed by the inverted pendulum legs.

However, if the emissivity increases to 0.8, a fin thickness of $20\,\mathrm{mm}$, or below, leads again to the previous conclusions, made for the initial case, and the circular RHX with vertical fins remains the preferred setup.

4.2.2 Alternative fin designs

As mentioned earlier, one idea for the next-generation E-TEST prototype is to use fins with higher emissivity, either by applying different coatings or by changing their shape, to reduce the mirror temperature. This section aims to study the effect of such alternative fin shapes. The analysis is performed on the first version of the E-TEST cryostat RHX, which provides a reliable reference.

To begin with, rather than the current flat simple design, shown in Figure 4.14a, the fins could have a corrugated shape, as presented in Figure 4.14b, or honeycomb shape, as illustrated in Figure 4.14c. These new shapes could improve heat radiation between the IRHX and the ERHX by increasing the fin emissivity.

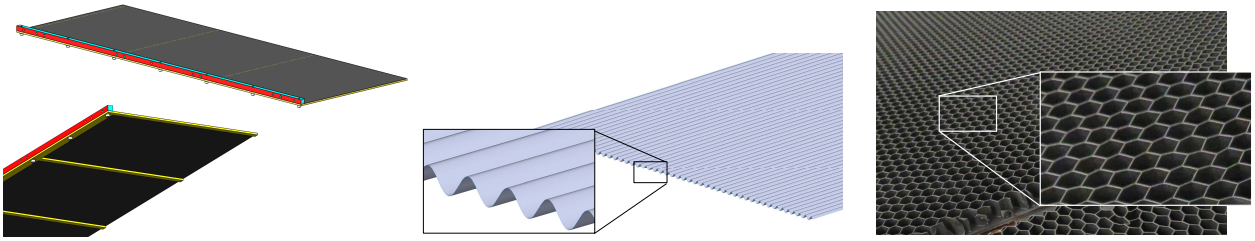

(a) Fin flat shape with fork reinforcement in yellow and additional reinforcement at the base in red.

(b) Corrugated fin shape.

(c) Honeycomb fin shape.

Figure 4.14: Different possible fin shapes.

However, these new designs would likely require apparent thicker fins. This reduces the number of fins that fit into the cryostat and therefore could induce the need for wider fins, which cannot fit within the current RHX anymore.

This study focuses on these limiting cases, specifically, the minimum emissivity values required to compensate for the reduced number of thicker fins.

It is important to note that in reality, the changes in fin thickness will not necessarily lead to a decrease in the number of fins that can be mounted in the IRHX. In fact, for the current prototype, the safety margin between two fins was highly conservative, since it was known that the fins were highly deformable and that they were not perfectly flat as initially designed. Therefore, if the fin apparent stiffness is higher with another geometry, the safety margin could be decreased, compensating for the higher thickness. However, since the exact geometries and resulting apparent stiffness are not known, this effect will be disregarded to stay the more conservative possible and ensure that no matter what the apparent stiffness is, the discussion remains reliable. Therefore, the safety margin between two fins of the RHX remains the same, $h_{sm} = 2\,\mathrm{cm}$, for all thicknesses considered.

The total radiation surface per fin stage on the cryostat is calculated using the size of the current cryostat fins. These dimensions are shown in Figure 4.15. The total resulting radiation surface per fin stage is $A_{stage} = 2.3\,\mathrm{m}$.

The number of stages that can be mounted on the cryostat, is computed in the same expression as the one presented in Equation 4.8 for the circular RHX horizontal fins configuration.

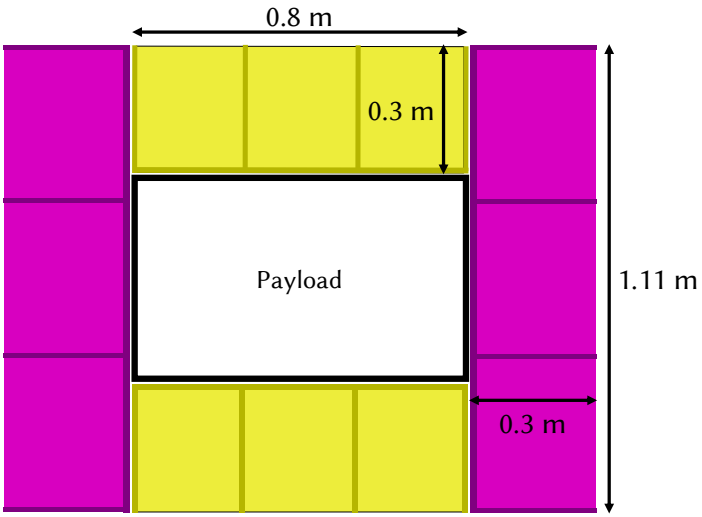

Figure 4.15: Dimensions of the fins shown on the top view of the current IRHX design.

Then, the total radiative surface of the RHX is simply obtained as,

$$A_{IRHX} = A_{stage} N_{H,fins}. \tag{4.12}$$

The minimum emissivity of the fins to reach the required $T_{IRHX} = 22\,\mathrm{K}$ is then computed by rearranging the Equation 2.4 into,

$$\varepsilon_{RHX} = \frac{2\,\dot{Q}_{parasit}}{A_{IRHX}\sigma(T_{IRHX}^4 - T_{ERHX}^4) + \dot{Q}_{parasit}}, \tag{4.13}$$

with $T_{ERHX} = 15\,\mathrm{K}$ and $\dot{Q}_{parasit}$, the same temperature of ERHX and heat rate reaching the payload as previously.

The emissivities for different fin thicknesses are computed and presented in Table 4.4.

$\mathbf{h_{thickness}}[\mathrm{mm}]$	**3.5**	**10**	**15**	**20**
$\mathbf{N_{H,fins}}$	35	31	28	26
$\boldsymbol{\varepsilon_{RHX}}$	0.6	0.66	0.7	0.73

Table 4.4: Fin minimum required emissivity to achieve the same thermal performance for different fin thicknesses and the resulting number of fin stages that can fit in the IRHX.

The thinnest fin thickness considered, $3.5\,\mathrm{mm}$, corresponds to that of the current cryostat. The associated emissivity, $\varepsilon = 0.6$, differs from the reference value in [13], which is expected since the actual emissivity of the fins is unknown. In that earlier study, emissivity was chosen to calibrate a thermal model instead of being directly measured. For the purpose of the ongoing analysis, the analytical value $\varepsilon = 0.6$ will serve as the reference.

Table 4.4 shows that the required emissivity increases relatively slightly with fin thickness. As the thickness increases from $3.5\,\mathrm{mm}$ to $15\,\mathrm{mm}$, the minimum emissivity rises from 0.6 to 0.7. This moderate change suggests that using thicker fins is a viable option if they can reach higher emissivity. These results are particularly encouraging for honeycomb structures. For example, an aluminum honeycomb with a cell size of about $3\,\mathrm{mm}$ and a height of $10\,\mathrm{mm}$, coated with black paint, can achieve an emissivity of approximately 0.85 at $20\,\mathrm{K}$ [28]. If the E-TEST fins were made from such

a structure, the high emissivity could offset the effect of increased thickness and still result in a lower mirror temperature than the one currently obtained. Indeed, assuming fins with a thickness of $10\,\mathrm{mm}$ and a surface emissivity of 0.85 leads to a temperature $T_{IRHX} = 20.4\,\mathrm{K}$, which is approximately the mirror temperature in the E-TEST prototype.

In summary, considering more advanced fin geometries than the current flat design could improve the cryostat thermal performance. Some structures can significantly increase the fin emissivity. Although these geometries may increase the fin thickness, a sufficiently high emissivity still lead to better thermal results. This is even more true if the new geometries also increase the overall rigidity of this fin. One promising option is the black-coated honeycomb structure mentioned in [28], which already shows characteristics that could lead to a lower mirror temperature. However, additional factors must be considered when selecting a fin geometry, such as cost and ease of manufacturing. For example, honeycomb structures are typically more expensive to produce than flat surfaces. Therefore, a detailed study comparing thermal performance and cost for specific geometries should be conducted to determine whether the thermal gains justify the added expense.

4.3 Conclusion

This chapter presented both simple and advanced improvements to the current E-TEST prototype design. On the low-complexity side, it has been shown that increasing the emissivity of the tube interior surfaces enables to compensate for shorter and/or wider tubes. In addition, an alternative assembly method was proposed to avoid disassembling the inverted pendulum and make the overall process more practical.

On the high-complexity side, several new RHX geometries were introduced to simplify assembly, avoiding the need to disassemble the IP, while keeping the process very similar to that of the current prototype. These new designs were also made to optimize the space occupied by the cryostat. Among them, a circular RHX with vertical fin design was identified as the most efficient. It optimizes the use of available space, is relatively easy to manufacture with rectangular fins, and provides the required radiative surface to reach the required temperature. The impact of fin thickness and emissivity was also studied, confirming the feasibility of this design under a wide range of realistic conditions. In addition, the possibility of using different fin geometries while keeping the same RHX architecture as in the current E-TEST prototype was studied. It showed that using alternative fin designs that increase the fin emissivity, such as corrugated or honeycomb shapes, could be thermally efficient. Indeed, the required emissivity to compensate for the reduction of the RHX radiative surface, as a result of the higher thickness of such geometries, increases relatively slightly with this increasing thickness. In particular, one specific honeycomb geometry painted in black showed characteristics that would outperform the thermal performance of the current cryostat and enable to reach a mirror temperature close to $20.4\,\mathrm{K}$ instead of the current $22\,\mathrm{K}$. However, these improvements must still be weighed against factors such as manufacturing complexity and cost.

Overall, the suggested improvements provide a basis for upgrading the E-TEST prototype and adapting its main concepts to the more challenging ET constraints.

Part II

ET-LF

CHAPTER 5

CRYOSTAT DESIGN

Now that the current E-TEST prototype has been thoroughly examined and potential improvements have been considered, the insights provided from these analyses will be applied to the case of the ET cryostat and its specific constraints. This begins with the design of a RHX that can fit within the allocated space while still being capable of extracting, through radiation, the thermal load to cool the mirror down to its target temperature. The design process and considerations for this RHX are presented in this chapter.

5.1 RHX designs derived from E-TEST improvements

The real Einstein Telescope Low Frequency cryostat has to fit within cylindrical space. This cylindrical space is externally bounded by the thermal shield field by single phase helium at $5\,\mathrm{K}$, as discussed in the introduction and shown in Figure 1.7.

To start the design of the RHX for the ET-LF, the first step is to evaluate the total radiative heat transfer area of IRHX, A_{IRHX}, required to cool the payload at a temperature of $10\,\mathrm{K}$-$20\,\mathrm{K}$. As explain earlier, this computation is completely independent of the fin design and depends only on the ERHX and IRHX temperatures, T_{ERHX}, T_{IRHX}, the emissivity of the fins, ε_{RHX}, and the heat rate reaching the payload that has to be evacuated, $\dot{Q}_{parasit}$.

The heat rate to the payload is evaluated as $500\,\mathrm{mW}$[17]. Similarly, it is assumed that $T_{ERHX} = 2\,\mathrm{K}$[8], since it corresponds to the expected cooling capacity temperature reached by the ERHX GHe panels in the configuration presented in Figure 1.6. The emissivity, is initially assumed to be the same as the actual emissivity of the E-TEST fins, $\varepsilon_{RHX} = 0.65$. A discussion about this emissivity is lead later in this thesis. The last parameter to be determined to apply the Equation 2.5 and calculate the total required transfer area, is the IRHX temperature.

During the very first design of the ET cryostat, the IRHX and the mirror were assumed to be at the same temperature, similarly as in the E-TEST prototype, leading to $T_{IRHX} = T_{mirror} = 20\,\mathrm{K}$. This yielded a very small required total radiative area,

$$A_{IRHX} = \dot{Q}_{parasit} \frac{(2 - \varepsilon_{RHX})}{\varepsilon_{RHX}\sigma} \frac{1}{T_{IRHX}^4 - T_{ERHX}^4} = 102.4\,\mathrm{m}^2. \tag{5.1}$$

However, the thermal study presented in the following chapter made it possible to realize that it was a too optimistic assumption. Indeed, this assumption means that all the payload elements,

including the mirror, the marionette, the platform and the heat exchanger, are at the same temperature, which does not reflect the reality. In fact, as represented in Figure 6.1, and described in the thermal analysis, the components are in relation with each other by radiation and/or conduction and are not all at the same temperature depending on the heat transfer between them.

Considering this area as the RHX area actually leads to a mirror temperature of $25.13\,\mathrm{K}$, which is above the maximal desired temperature of $20\,\mathrm{K}$. After testing several values, the thermal model showed that to reach $T_{mirror} = 20\,\mathrm{K}$, the internal heat exchanger temperature should be around a temperature $T_{IRHX} = 13\,\mathrm{K}$. This new temperature leads to

$$A_{\mathrm{IRHX}} = \dot{Q}_{parasit} \frac{(2 - \varepsilon_{RHX})}{\varepsilon_{RHX}\sigma} \frac{1}{T_{IRHX}^4 - T_{ERHX}^4} = 573.7\,\mathrm{m}^2. \tag{5.2}$$

The fins can be subsequently designed in detail using the same methodology as presented earlier in Section 4.2.1 for the E-TEST cryostat. Indeed, since the boundaries of the ET cryostat volume are cylindrical, the same circular designs with vertical and horizontal fins can be sized up to fit the ET constraints. This is done in the following sections.

In addition, an order of magnitude of the additional mass of the IRHX fins to the payload can be roughly estimated from the required radiative surface area. To get a first rough estimate, it is considered that the fins of the ET cryostat are shaped similarly to the ones of the first version of the E-TEST prototype. Therefore, an approximate fin surface mass density can be computed from the characteristics of the E-TEST fin tested in the laboratory. The fin had a length of $1.11\,\mathrm{m}$ and a width of $0.3\,\mathrm{m}$, as illustrated in Figure 4.15. Its measured mass was $0.77\,\mathrm{kg}$, yielding a surface density of approximately $\rho_S \approx 2.3\,\mathrm{kg\,m^{-2}}$. The total mass of all IRHX fins in the cryostats can then be approximated as

$$m_{IRHX,fins} = \rho_S \, \frac{A_{IRHX}}{2}, \tag{5.3}$$

where the factor of 2 accounts for the fact that each fin has two radiative surfaces.

The resulting total masses of the IRHX fins for both the E-TEST prototype and the ET cryostat are presented in Table 5.1. These values are based on the total radiative areas provided in Equation 4.2 for E-TEST and Equation 5.2 for ET-LF. As expected, the IRHX fins for the ET cryostat are significantly heavier due to the larger required radiative area. However, considering that the mirror alone has a mass of approximately $200\,\mathrm{kg}$ in ET-LF, this additional mass may be acceptable for a system of this scale.

It is important to note that this calculation provides only an initial estimate of the IRHX fins mass in the ET cryostat, based on the current E-TEST fin chape. In future versions of the E-TEST prototype and the ET-LF cryostat, the fin geometry is expected to change, as the existing E-TEST fin design was too flexible and exhibited unpredictable mechanical behavior. Consequently, the surface density of the fins will also change, and a more accurate mass evaluation will be required using updated parameters. Therefore, it is only at that point that it will be possible to assess whether the total mass of the IRHX fins is a critical issue for the ET cryostat.

	E-TEST	**ET**
$\mathbf{m_{IRHX,fins}}$ [kg]	84	664

Table 5.1: Masses of all the fins in IRHX for E-TEST and ET cryostats.

5.1.1 Circular RHX with horizontal fins design

To begin the design of the ET RHX, the number of horizontal fins integrated in the IRHX is calculated using the same expression as the one used to compute the number of horizontal fin stages in the design of the E-TEST RHX. However, the values of the parameters within this formula are different. The safe margin between two facing fins, $h_{sm} = 2\,\mathrm{cm}$, is the same as the one used to design the E-TEST fins. The height of the ET cryostat, $h_{cryostat} = 2.6\,\mathrm{m}$, differs from that of the E-TEST. This value corresponds to the limit presented in Table 1.1. Finally, the thickness of the fins is currently unknown, but a discussion about its impact on the fins design is provided at the end of this section.

Once the thickness is fixed, the number of fins that can be superposed within the cryostat space is calculated like in Equation 4.8,

$$N_H = \left\lfloor \frac{h_{cryostat}}{2h_{sm} + h_{thickness}} + 1 \right\rfloor \tag{5.4}$$

Therefore the area of one fin is

$$A_H = \frac{1}{2}\frac{A_{IRHX}}{N_H}. \tag{5.5}$$

Here, the factor two again comes from the fact that one fin has two radiative surfaces.

Following the same methodology as previously, the internal radius is then fixed to determine the detailed design of the fins. This time both RHX radii have to satisfy the condition,

$$r_{1,ET} = 0.6[m] < r_{int} < r_{ext} < r_{2,ET} = 1.95\,\mathrm{m}. \tag{5.6}$$

The width of the fins and the external radius of the structure are computed with the following equations, assuming the same safe margin, between the tip of the fin of one RHX part and the structure of the other, as for E-TEST, $w_{sm} = 2\,\mathrm{cm}$,

$$w_H = \sqrt{r_{int}^2 + \frac{A_H}{\pi}} - r_{int}, \tag{5.7}$$

$$r_H = r_{int} + w_H + w_{sm} = \sqrt{r_{int}^2 + \frac{A_H}{\pi}} + w_{sm}. \tag{5.8}$$

5.1.2 Circular RHX with vertical fins design

Similarly, for the vertical fins structure design, the number of fins is computed with

$$N_V = \left\lfloor \frac{2\pi r_{int}}{2h_{spacing} + h_{thickness}} \right\rfloor. \tag{5.9}$$

Therefore the fin area is,

$$A_V = \frac{1}{2}\frac{A_{IRHX}}{N_V}, \tag{5.10}$$

with the same $h_{cryostat} = 2.6\,\mathrm{m}$.

Finally, the width and external radius are evaluated with

$$w_V = \frac{A_V}{h_{cryostat}}, \tag{5.11}$$

$$r_{V,ext} = r_{int} + w_V + w_{sm} \approx r_{int} + \frac{\frac{1}{2}A_{IRHX}(2h_{sm} + h_{thickness})}{h_{cryostat}\ 2\pi\ r_{int}} + w_{sm}. \tag{5.12}$$

5.1.3 Circular RHX designs for various fin thickness and emissivity

To determine the most suitable ET design in terms of projected occupied surface, Figure 5.1 presents the external radius as a function of the internal radius for both configurations and various fin thicknesses, considering the same fin surface emissivity $\varepsilon_{RHX} = 0.65$. The black curve represents the circular RHX with horizontal fin configurations, while the blue curve corresponds to the vertical fin configuration.

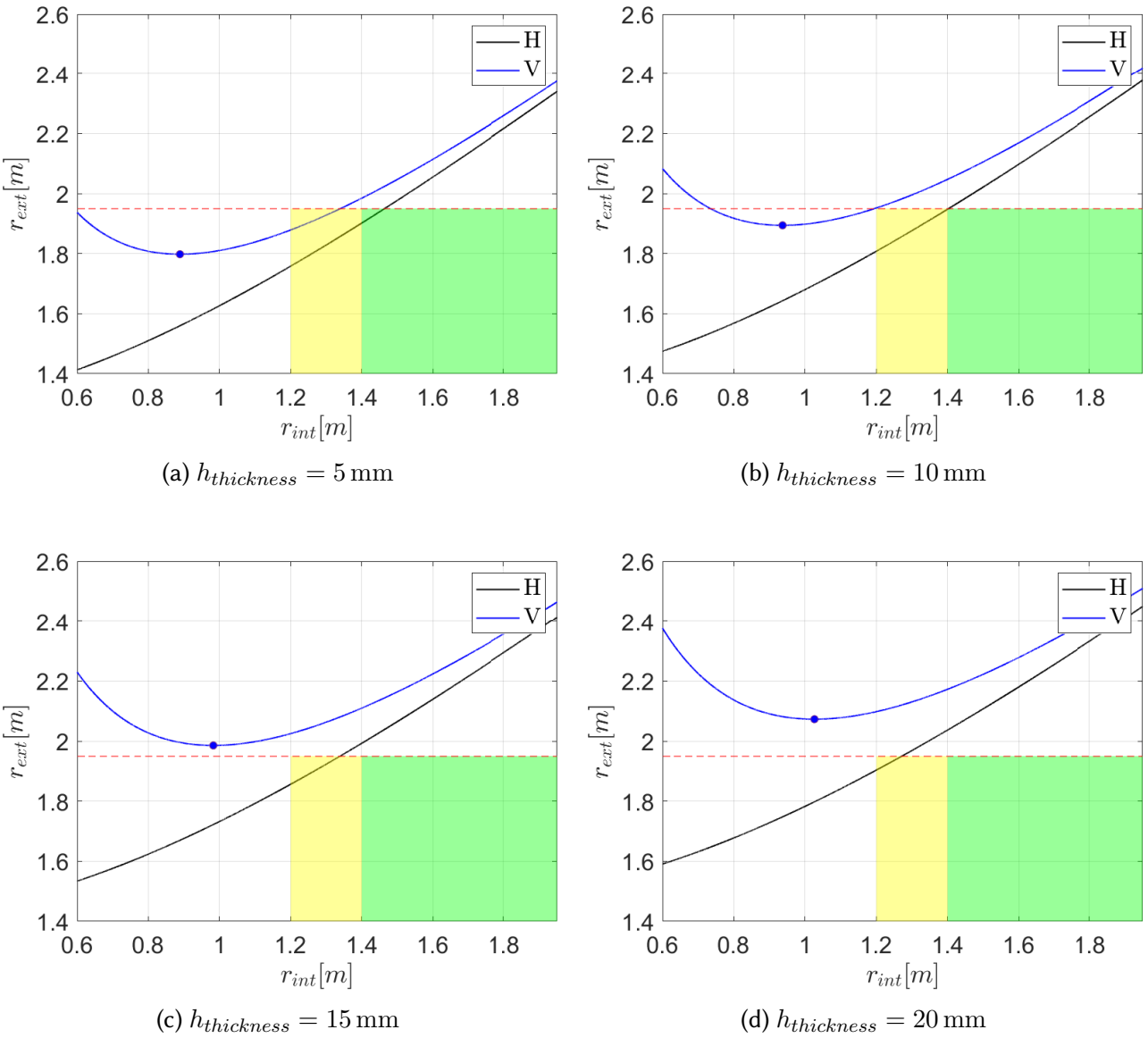

(a) $h_{thickness} = 5\,\text{mm}$

(b) $h_{thickness} = 10\,\text{mm}$

(c) $h_{thickness} = 15\,\text{mm}$

(d) $h_{thickness} = 20\,\text{mm}$

Figure 5.1: Comparison of the evolution of the external radius with the internal radius of the fins structure of the two circular configurations for different fin thicknesses.

As in the E-TEST design comparison, in the subfigures of Figure 5.1, a dotted red line indicates the maximum allowable external radius of the fin structure. This provides a clear visual limit. In addition, colored rectangles have been added to represent a new constraint specific to the ET cryostat, the need for a technician to walk around the payload. It is assumed that a clearance of at least $80\,\mathrm{cm}$ between the payload and the IRHX allows for comfortable access. The minimum acceptable clearance is assumed to be $60\,\mathrm{cm}$.

Green and yellow areas are used to indicate compliance with this constraint. The green area corresponds to regions where the clearance is equal to or greater than $80\,\mathrm{cm}$ and the external radius is less than $1.95\,\mathrm{m}$. The yellow area covers a clearance equal to or greater than $60\,\mathrm{cm}$ under the same external radius limit. The green area represents the ideal condition, while the yellow may still be acceptable.

As observed in the E-TEST results, the horizontal fin configurations show an almost linear trend for all fin thicknesses considered. In contrast, the vertical fin configurations show a distinct minimum marked with a point.

Figure 5.1 also shows that increasing the fin thickness affects both configurations similarly. A vertical shift of about $0.2\,\mathrm{m}$ is observed between Figure 5.5a ($h_{thickness} = 5\,\mathrm{mm}$) and Figure 5.1d ($h_{thickness} = 20\,\mathrm{mm}$). However, since the blue curve is always above the black one, it crosses the external radius limit sooner and becomes unsuitable for some thicknesses. For example, in Figure 5.1c ($h_{thickness} = 15\,\mathrm{mm}$), the blue curve is entirely above the limit line.

Additionally, the vertical configuration never enters the green area and only enters the yellow area at the smallest thickness. The horizontal configuration reaches the green area only once, at the edge, for $h_{thickness} = 10\,\mathrm{mm}$, and not at all for larger thicknesses.

In conclusion, to ensure adequate space for a technician to work comfortably around the payload, a new fin configuration must be developed.

5.2 RHX design optimization

The previous section highlighted that although the scale up to ET constraints of the E-TEST circular new designs allows the cryostat to fit within the available space, it fully occupies that space and there is no room left for a person to walk around the mirror cage. Condition that is imposed for the ET cryostat. To solve this, fins with a smaller width are needed. However, in the previous design, the fin width is fixed by the internal radius, making this change impossible.

Nevertheless, the vertical fin layout leads to wasted space. Along certain parts of the internal fin structure, the fins could extend farther without obstructing the beam pipe that is in front of the mirror. This section introduces a new vertical fin design that includes two fin sizes. Shorter fins are placed above the beam pipe and longer fins are placed where they do not block the laser path in front of the mirror, nor the projected surface of the beam pipe.

Firstly, the portion of the inner RHX perimeter that interferes with the optical aperture is evaluated. A representation of this trigonometric problem is presented in Figure 5.2. In this latter, the perimeter that could interfere with the optical aperture, where short fins are needed, is highlighted in yellow and named p_s. Using the notation shown in this figure, this perimeter can be computed as

$$\beta = arcsin\left(\frac{r_{BP}}{r_{int}}\right); \qquad p_s = 2 \times 2\beta r_{int}, \tag{5.13}$$

with r_{BP}, the radius of the beam pipe in front of the two sides of the mirror.

Then, since the perimeter of the inner fins structure, p, and the number of fins, N_V are directly linked, the number of fins in front of the optical aperture, N_{Vs} and the corresponding perimeter, p_s are also linked, following the equation,

$$\frac{p}{N_V} = \frac{p_s}{N_{Vs}} \Leftrightarrow N_{Vs} = \frac{p_s}{p} N_V = \frac{2\beta}{\pi} N_V. \tag{5.14}$$

In Equation 5.14, the total number of vertical fins that can be integrated in the IRHX, N_V, is defined in the same way as in the previous section and can thus be evaluated with Equation 5.9. Similarly as in the previous case, $h_{sm} = 2\,\mathrm{cm}$ and the thickness of the fins, $h_{thickness}$, is unknown. Its effect on the design is discussed at the end of this section.

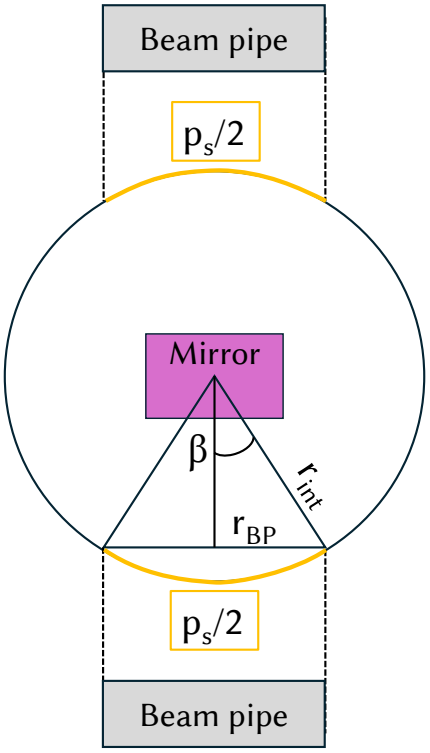

Figure 5.2: Draft of the top view of the inner fins structure, with the mirror and beam pipe projection.

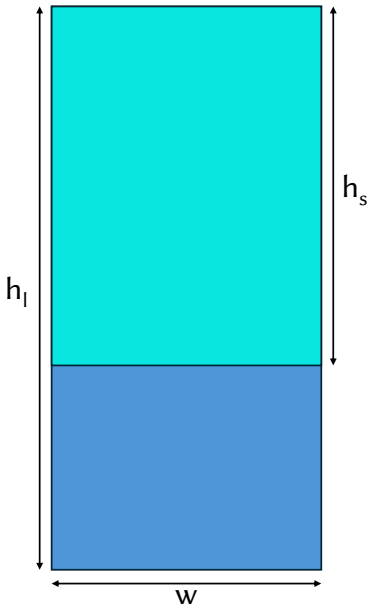

Figure 5.3: Dimension parameters of the two-sizes vertical fins in the circular structure.

In addition, since the fins of both sizes, the shorter and the longer ones, are rectangular and designed with the same width w, the ratio of the fin areas, R_A is the same as the ratio of the lengths of the fins. That is

$$R_A = \frac{A_s}{A_l} = \frac{h_s}{h_l}, \tag{5.15}$$

with A_l and A_s, and h_l and h_s, respectively the area and length of the longer and shorter fins, that are shown in Figure 5.3.

Therefore, the width of the fins, w, can be obtained by successively computing

$$A_{tot} = N_s A_s + N_l A_l \tag{5.16}$$

$$= N_s R_A A_l + (N_{fins} - N_s) A_l, \tag{5.17}$$

$$\Leftrightarrow A_l = \frac{A_{tot}}{N_s R_A + (N_{fins} - N_s)} \tag{5.18}$$

$$= \frac{A_{IRHX}/2}{(R_A \frac{2\beta}{pi} + 1 - \frac{2\beta}{pi}) N_{fins}}, \tag{5.19}$$

$$\Rightarrow \text{and } w = \frac{A_l}{h_l} = \frac{A_{IRHX}/2}{(R_A \frac{2\beta}{pi} + 1 - \frac{2\beta}{pi}) N_{fins} h_l}. \tag{5.20}$$

Here, A_{IRHX} is the same as in the previous section since, as mentioned before, it does not depend on the fin design. Similarly, the factor two reflects the fact that one fin has two radiative surfaces, like in the previous cases.

Afterwards, the external radius of the vertical fins structure can be obtained with

$$r_{Vsl,ext} = r_{int} + w + w_{sm} = r_{int} + \frac{A_{IRHX}/2}{h_l (R_A \frac{2\beta}{pi} + 1 - \frac{2\beta}{pi}) N_{fins}} + w_{sm} \tag{5.21}$$

$$\approx r_{int} + \frac{(2h_{spacing} + h_{thickness}) A_{IRHX}/2}{h_l (R_A \frac{2\beta}{\pi} + 1 - \frac{2\beta}{\pi}) 2\pi r_{int}} + w_{sm}. \tag{5.22}$$

Therefore, the external radius of the fin structure is again not linear with the internal radius as for the vertical one fin size case.

An example of this new two sizes fins design is shown in Figure 5.4. In this figure, the thermal shielding and outer boundary with the environment are cut in half to better see the fins design. In addition, the inner limit of the cryostat, that is the payload, is shown in purple, while the external limit of the cryostat, the He $2\,\mathrm{K}$ plate, is shown in green. In addition, for a better understanding, the model is seen from its front and trimetric views, respectively in Figures 5.4a and 5.4b. The parameters that were used to design this cryostat are shown in Table 5.2

Parameters	**Circular Vertical Two- Sizes Fins Configuration**
h_s	$1.1\,\mathrm{m}$
h_l	$2.6\,\mathrm{m}$
$h_{thickness}$	$5\,\mathrm{mm}$
h_{sm}	$2\,\mathrm{cm}$
w_{sm}	$2\,\mathrm{cm}$
N_V	209
N_{Vs}	45
r_{int}	$1.4\,\mathrm{m}$
w_{Vfins}	$40\,\mathrm{cm}$
$r_{Vsl,ext}$	$1.9\,\mathrm{m}$

Table 5.2: Parameters of one circular vertical two-sizes fins configuration.

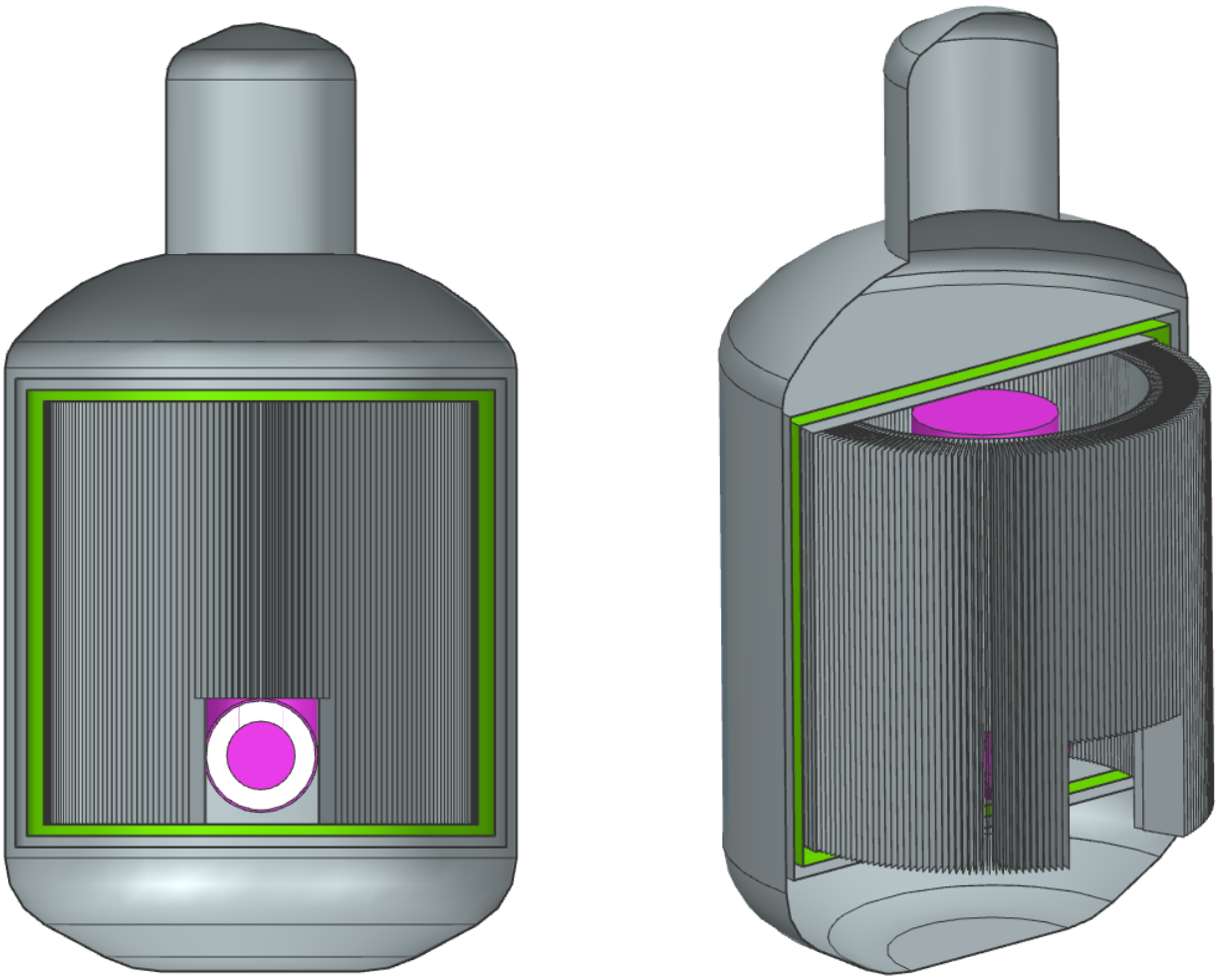

(a) Front view.

(b) Trimetric view.

Figure 5.4: NX CAD of one circular vertical two sizes fins configuration, following the design parameters presented in Table 5.2.

To evaluate the advantage of this new fin design compared to the two previous ones, and to determine if it is a suitable solution for the ET cryostat, Figure 5.5 shows the evolution of the external radius as a function of the internal radius for different thicknesses, considering again the same emissivity $\varepsilon_{RHX} = 0.65$. The curve corresponding to the new two-size fin design is shown in magenta. As in Figure 5.1, the horizontal red dotted line represents the upper limit of the external radius. The green and yellow rectangles again indicate the areas that also meet the clearance requirements of $80\,\mathrm{cm}$ and $60\,\mathrm{cm}$ between the payload and the fin structure, ensuring enough space for a technician to access the payload.

It can be observed that, in the most relevant areas, the yellow and especially the green regions, the curve for the two-size vertical fins lies below the other two configurations for all considered thicknesses. This allows the new design to remain within the green area up to a thickness of $15\,\mathrm{mm}$. Even at the largest thickness, it provides more available space for the technician compared to the previous designs.

Therefore, this third circular configuration can be considered the most suitable option. It allows for the use of rectangular-shaped fins, which are less expensive to manufacture than circular fins, while still maximizing the available space within the cryostat. At the same time, it provides sufficient clearance to ensure comfortable access for a technician across nearly all the fin thicknesses considered.

However, it is important to highlight a potential drawback of this configuration related to thermal noise. In the case of vertical fins, thermal noise can cause mechanical vibrations aligned with the direction of the laser beam used for optical measurements. This alignment increases the risk that thermal noise introduces unwanted displacement along the laser path, potentially affecting the sensitivity and accuracy of the optical system. Therefore, a careful evaluation of the thermal noise contribution in this configuration is essential to determine whether it is a critical issue for the cryostat performance.

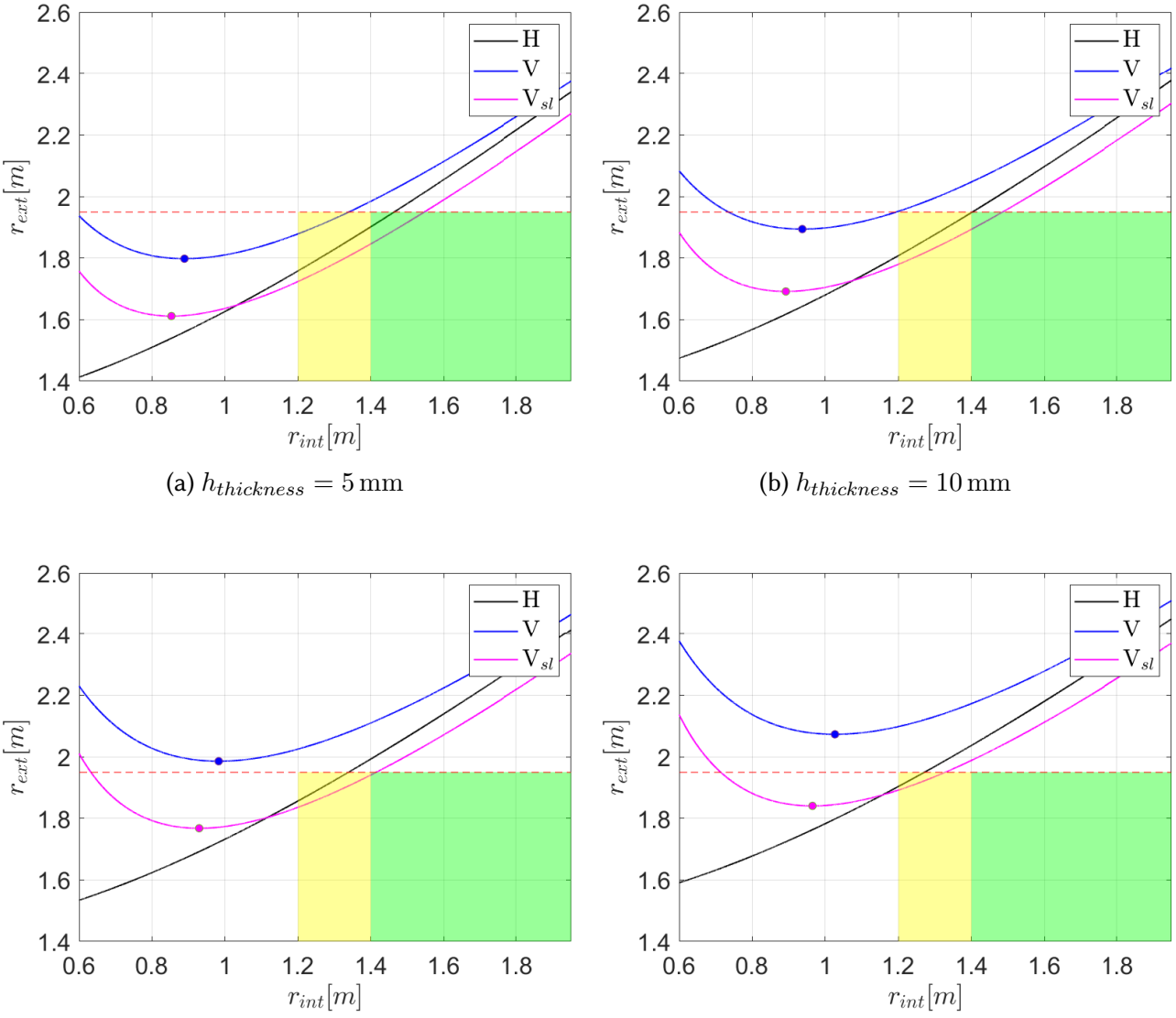

(a) $h_{thickness} = 5\,\mathrm{mm}$

(b) $h_{thickness} = 10\,\mathrm{mm}$

(c) $h_{thickness} = 15\,\mathrm{mm}$

(d) $h_{thickness} = 20\,\mathrm{mm}$

Figure 5.5: Comparison of the evolution of the external radius with the internal radius of the two-sizes vertical fins configuration with the initial vertical and the horizontal ones.

5.3 Conclusion

This chapter focused on designing a RHX that fits the specific constraints of the ET-LF cryostat. The goal was to adapt the designs developed for the E-TEST prototype in the previous chapter, to the ET-LF cryostat. Therefore, the two circular RHX designs, with horizontal and vertical fins, were scaled to meet the thermal needs of the ET-LF. Both provided enough radiative surface to extract the required $500\,\mathrm{mW}$ but completely filled the available space. Thus, there was no room left for technicians to access the mirror, which is a requirement for the ET cryostat.

To solve this, a new configuration, similar to the circular RHX with vertical fins configuration but including two different fin lengths, was introduced. In this new design, the shorter fins are placed in front of the optical apertures to avoid blocking the laser path, while the longer fins fill the remaining available space. This solution makes better use of the volume around the payload and creates enough free space for maintenance work.

A key design parameter in the RHX design is the thickness of the fins, as already explained in the E-TEST cryostat design part. Therefore, the ET RHX designs were analyzed considering fin thicknesses of 5, 10, 15, and $20\,\mathrm{mm}$. It showed that as expected, it becomes harder to fit the RHX within the cryostat while preserving access around the mirror as the fin thickness increases. Most vertical configurations exceeded spatial limits at higher thicknesses. Horizontal fin configurations remained feasible, but occupied too much volume to allow comfortable access for the maintenance.

The two-size vertical fin design proved to be the most effective. It remained within the cryostat limits up to a fin thickness of $20\,\mathrm{mm}$ and maintained more free space around the mirror than the comfortable limit, up to a fin thickness of $15\,\mathrm{mm}$. In addition, it uses a rectangular fin shape which is relatively easy to manufacture. However, due to the vertical orientation of the fins, a detailed thermal noise analysis is needed to assess the risk of vibrations along the laser axis, which could affect optical sensitivity if not properly controlled.

CHAPTER 6

THERMAL ANALYSIS

The primary challenge of the ET-LF is to cool the mirror to a temperature not exceeding $20\,\mathrm{K}$. In the previous chapter, a RHX was developed to achieve this target through radiative heat transfer between ERHX, the thermal sink, and IRHX. To assess the effectiveness of this RHX and to evaluate whether the innovative cooling approach demonstrated by the E-TEST prototype meets the demanding requirements of the ET-LF, this chapter presents a detailed thermal analysis of the system.

6.1 Thermal model description

To begin the thermal study of the ET Cryostat, an electrical network analogy is made using isothermal nodes discretization, as in the E-TEST thermal study. This model consists of five key components: the mirror, the marionette (MA), the platform (PF), the internal radiative heat exchanger (IRHX), which includes the internal fin set and the payload, and the external radiative heat exchanger (ERHX). This latter is the thermal sink of the system and is made up of the external fin set and the He $2\,\mathrm{K}$ thermal shield. A sketch of this system is shown in Figure 6.1a, and the corresponding electrical network analogy, called the thermal node model is shown in Figure6.1b.

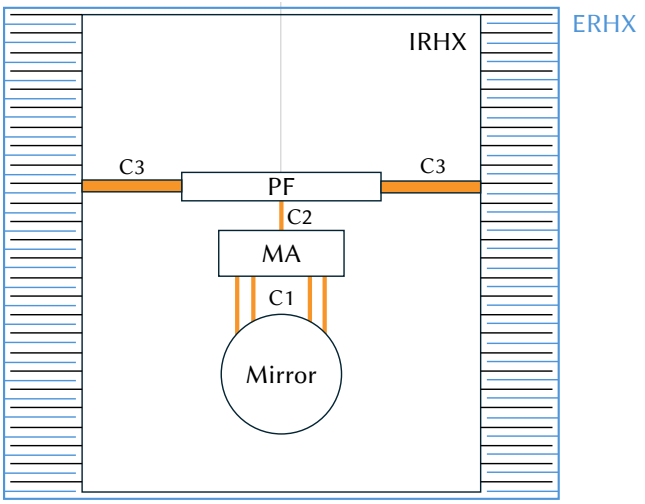

(a) Draft of the thermal system of the cryostat.

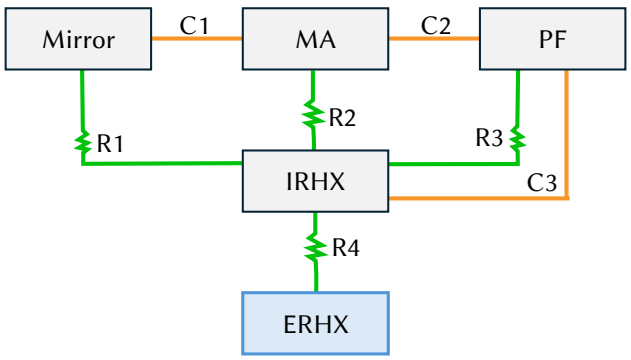

(b) Thermal node model of the cryostat with the conductive links shown in orange and the radiative links shown in green.

Figure 6.1: Thermal system representation of the ET-LF cryostat.

In both figures, the ERHX is shown in blue, as it is the only node maintained at a fixed temperature and serves as the thermal boundary of the system. Conductive links are shown in orange, while radiative links are shown in green. It is important to note that the conductive links are of different types. For example, the connection between the platform and the internal fins set is made through a rigid structure composed of several horizontal beams that support and connect the platform to the heat exchanger. On the other hand, the links between the mirror, the marionette, and the platform are cables.

To evaluate the thermal behavior of this system, the thermal model is implemented and solved in ESATAN software. In this implementation, the conductive radiative heat rates are computed with the expression presented in Equation 2.1. The links between the mirror and the marionette, as well as the link between the marionette and the platform, are made of silicon. The silicon has been chosen among other materials, such as sapphire, because its fibers maintain higher thermal conductivity at cryogenic temperatures. Both materials conduct heat well in bulk form, but thin fibers lose conductivity due to phonon scattering. This scattering occurs when heat particles bounce off the fiber surfaces. In silicon fibers, this effect is small in comparison with sapphire fibers, therefore they are more conductive and enable to cool the mirror at lower temperatures[16]. The links between the platform and the heat exchanger are unknown. Several options have been tested. Finally, it has been chosen to work with 6 tubes made of Al6061, displaced all around the platform as shown in Figure 6.2.

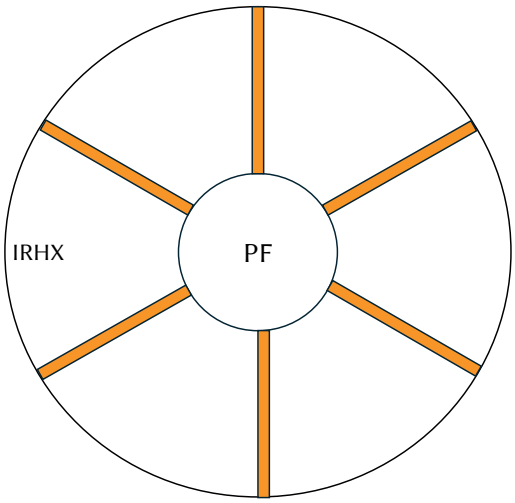

Figure 6.2: Top view of the cryostat to show the conductive link between the platform and the internal heat exchanger (C3).

The material, length and cross-section area of the different conductive links, presented in Figure 6.1 are listed in Table 6.2.

Links	**Materials**	**Cross-section** $[\mathrm{m}^2]$	**Length**$[\mathrm{m}]$
C1	Si	4×	1.2
C2	Si		1
C3	Al6061	6×	0.8

Table 6.1: Conductive links characteristic of the ET system.

For the radiation analysis, the radiative heat transfer rates between elements are evaluated using the expression provided in Equation 3.35. In this simplified model study, the radiative conduc-

tance is linearized under the assumptions that the surfaces are diffuse and gray. Accordingly, it is expressed as

$$GR_{ij} = F_{ij}\varepsilon_i A_i. \tag{6.1}$$

All internal components, mirror, MA, and PF, are assumed to have a unitary view factor with IRHX. The IRHX itself is assumed to have a unitary view factor with the ERHX. This implies full radiative coupling, it means that all the heat rate that is emitted by the internal component is received by IRHX and that all the radiative heat rate that is emitted by this latter is received by the sink.

The silicon mirror is assumed to have an emissivity $\varepsilon \approx 0.4$ at $20\,\mathrm{K}$ [13]. This assumption is made in the frame of the E-TEST project and is expended to this case since the exact emissivity of the silicon mirror at cryogenic temperatures is unknown. The MA and PF are modeled as being made of aluminum alloy Al6061, and are assumed to have an emissivity $\varepsilon \approx 0.04$. This value is taken since at $273\,\mathrm{K}$, the emissivity of aluminum rough surfaces is $\varepsilon = 0.07$ [29] and it is assumed that it is slightly smaller at cryogenic temperatures, but the exact value is unknown. The fins of the heat exchanger are coated with a high-emissivity black paint, similar to the one used in the E-TEST cryostat, resulting in an emissivity $\varepsilon = 0.65$ [13].

Radiative areas are calculated from the geometry of each component. The internal components (mirror, MA, PF) have fixed dimensions chosen to fit within the design constraints. On the contrary, the RHX area can vary depending on the fin geometry to obtain the required thermal performance. As explained in the previous section, initially, the required radiative area was estimated to be $102.4\,\mathrm{m}^2$. However, the solution of the node thermal system showed that an effective fins radiative surface area of $573.7\,\mathrm{m}^2$ was necessary to meet the cooling requirements. The final radiative parameters for each link are presented in Table 6.2.

Links	**F**	ε	**A**$[\mathrm{m}^2]$
R1	1	0.4	1.14
R2	1	0.04	2
R3	1	0.04	2.8
R4	1	0.65	102.4 573.7

Table 6.2: Radiative link properties in the ET thermal model.

6.2 Thermal model results

The node thermal system is then solved using ESATAN. The equilibrium temperatures of the system elements are compared for the two IRHX radiative surfaces introduced above, that is the initial estimate of $102\,\mathrm{m}^2$ and the revised surface of $574\,\mathrm{m}^2$. The results are presented in Table 6.3. It can be seen that with the smaller surface, the mirror temperature rises above the target of $20\,\mathrm{K}$. In contrast, the larger surface leads to lower temperatures in all internal components and allows the mirror to stay below the required limit.

Elements	**Temperatures**[K] ($\mathbf{A} = 102.4\,\mathrm{m}^2$)	**Temperatures** [K] ($\mathbf{A} = 573.7\,\mathrm{m}^2$)
Mirror	25.46	19.87
MA	21.21	15.27
PF	19.39	12.87
HX	19.08	12.40
Sink	2	2

Table 6.3: Temperature of cryostat components for two different HX radiative surface areas.

The thermal conductive path between the mirror and the marionette is considered the most critical, as identified in [16]. To verify the validity of the simplified 5-node model, this link was refined into 10 smaller intermediate elements. The resulting element temperatures are shown in Table 6.4. The mirror and MA temperatures remain the same as the ones obtained with the simpler model, confirming its validity for overall system-level thermal predictions.

Elements	**Temperatures**[K] ($\mathbf{A} = 573.7\,\mathrm{m}^2$)
Mirror	19.87
End C1 section 1	19.45
End C1 section 2	19.01
End C1 section 3	18.57
End C1 section 4	18.12
End C1 section 5	17.67
End C1 section 6	17.21
End C1 section 7	16.74
End C1 section 8	16.26
End C1 section 9	15.77
MA	15.27
PF	12.87
HX	12.40
Sink	2

Table 6.4: Temperature of cryostat components with refined nodes along the mirror-marionette conductive path.

Once thermal convergence is achieved, the heat flux across each link is evaluated. The heat rates, calculated using ESATAN, are shown in Figure 6.3.

This figure highlights that when two possible paths, radiative and conductive, exist between two elements, most of the heat is transferred through conduction. In addition, among the internal components, the mirror contributes the most to radiative transfer as a result of its higher temperature. It can be noted that the net power balance at each node is verified, which confirms that the system is in steady-state equilibrium.

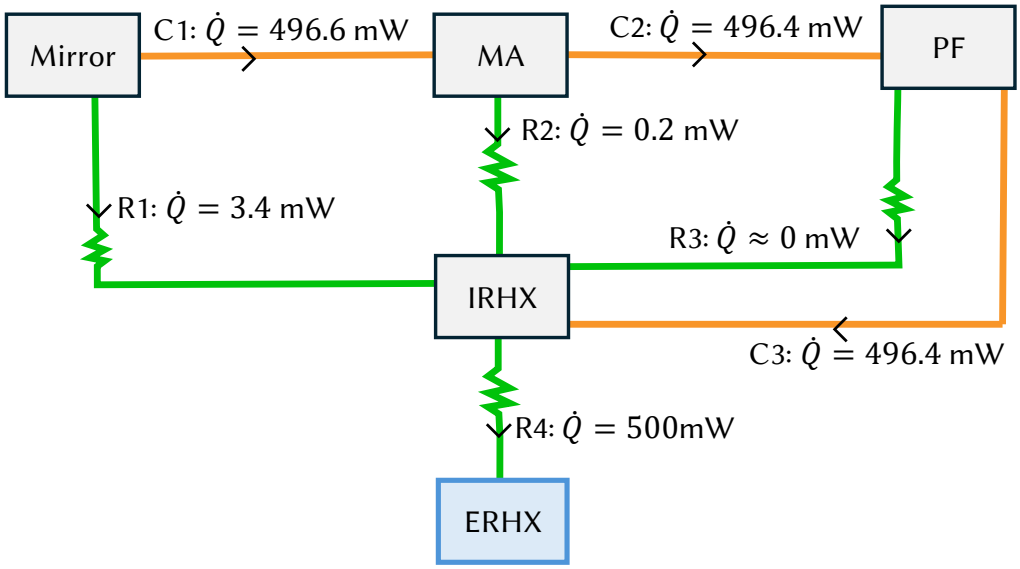

Figure 6.3: ET thermal node model with the resulting heat rate that passes through each link.

6.3 Conclusion

This chapter has presented a detailed thermal analysis of the ET-LF cryostat, with the aim of verifying whether a fully radiative cooling strategy could effectively bring the mirror to its target temperature of $20\,\mathrm{K}$. A simplified five-node thermal model was developed, including the mirror, marionette, platform, internal radiative heat exchanger, and the external radiative heat exchanger.

The analysis showed that the initial estimate of $102.4\,\mathrm{m}^2$ was not sufficient. However, increasing this area to $573.7\,\mathrm{m}^2$ allowed the mirror to reach a steady-state temperature of $19.86\,\mathrm{K}$. The thermal model also revealed that, inside the cryostat, heat transfer is dominated by conduction between the internal components. Radiative links between internal elements were minor in comparison. This validates the RHX design choices and material selections, such as using silicon for its high thermal conductivity at low temperatures.

The results confirmed that no conductive thermal link is required between the payload and the external environment. All the cooling of the payload, mirror, marionette, and platform is done through radiation heat transfer only. However, to enable sufficient radiative heat transfer, the ERHX must be actively cooled at 2K using an external cooling system.

Finally, the analysis showed good energy balance across all nodes, and refining the model along the critical conductive path confirmed the accuracy of the simplified version. Overall, this study demonstrated that, with an actively cooled ERHX, a fully radiative cryostat design is feasible and effective for ET-LF.

CHAPTER 7

CONCLUSION

7.1 Conclusion

This thesis focused on analysing the feasibility of using a fully radiative cryostat to cool down a suspended mirror to cryogenic temperatures, as required for the ET-LF. The work was based on the E-TEST prototype, developed in the context of the E-TEST project. It included a study of how this prototype could be improved and how the principles could be adapted to the ET-LF cryostat constraints.

After recalling the theoretical background of heat transfer, a vibrational and thermal analysis of the current E-TEST prototype was conducted. First, the vibrational behavior of a single fin was measured experimentally. It was then compared with two simplified models, a mass-spring model and a FEM model. Both captured the first natural frequencies well but did not reproduce the experimental mode shapes. The mass-spring model was found to be the most promising model for future analysis because it offers the best compromise between accuracy and ease of use. The first natural frequencies of the fin were found to lie above$10\,\mathrm{Hz}$, reducing the risk of resonance with environmental vibrations.

Then, the thermal behavior of the prototype was studied using a simplified node model. The parasitic heat loads were estimated analytically with the parameters set to match the reference simulation data. Following that, the transient evolution of the E-TEST cryostat was also estimated analytically and reproduced the measured prototype thermal behavior quite well. Therefore, similar thermal models were later used in this thesis to study the thermal behavior of alternative cryostats. This study also confirmed that the current E-TEST cryostat can cool the mirror to approximately $22\,\mathrm{K}$ in less than three weeks.

Several enhancements for the E-TEST cryostat were then suggested. On the low-complexity side, the effect of increasing the emissivity of the inner surface of the top tubes of the cryostat to compensate for making them shorter or wider was studied. It was found that if the coating is sufficiently emissive, it is possible to make the tubes shorter and wider without decreasing the thermal performance of the cryostat. An alternative assembly method was also suggested to simplify the construction process. Thereafter, more complex modifications involved redesigning completely the radiative heat exchanger and the fins shape. A circular RHX with vertical fins design was identified as the most promising solution, offering good compatibility with spatial constraints and decreasing the bending of the fins. In addition, it was found that using a different fin shape than the flat one used in the first version of the E-TEST prototype could help to enhance the thermal performance

of the cryostat. Indeed, some shapes, such as corrugated or honeycomb, increase the emissivity of the fins. They also increase the thickness of the fins, reducing the number of fins that can be integrated in the IRHX, but if the emissivity is sufficiently high, it can compensate for this effect and still lead to a lower mirror temperature. In fact, a particular aluminum honeycomb structure painted in black showed characteristics that would enable to reach a mirror temperature of $20.4\,\mathrm{K}$ instead of the current $22\,\mathrm{K}$ one.

Subsequently, the new designs were applied to the ET-LF cryostat. The circular RHX with vertical fins configuration was promising, but did not allow sufficient clearance for maintenance around the payload. To address this, a two-size vertical fin configuration has been developed. Short fins were placed above the optical apertures, whereas longer fins were used elsewhere to maximize the radiative surface within the available volume. The design was evaluated across a range of fin thicknesses and surface emissivities. It performed well, fitting within the constrained space while maintaining the clearance required in ET-LF for maintenance operations.

Then, a five-node thermal model of the ET cryostat was developed. It showed that the mirror can be cooled below $20\,\mathrm{K}$ using radiative transfer alone, if the IRHX radiative surface exceeds $570\,\mathrm{m}^2$ and that the ERHX is maintained at $2\,\mathrm{K}$. The model also indicated that conductive heat transfer dominates internal heat exchange between payload components.

In conclusion, the results demonstrated that a fully radiative cryostat is a promising solution for the future ET-LF cryostat. The study identified key improvements for the E-TEST prototype and confirmed, through simplified models, that the required thermal performance can be achieved for both the E-TEST and ET-LF cryostats. These results open the way for further investigations, including improving the vibration model, studying thermal noise, and refining the designs of the cryostats. These aspects are further discussed in the following section.

7.2 Future work

This thesis studied the E-TEST and ET cryostats from both thermal and vibrational perspectives. It has improved the understanding of the systems and presented several possible improvements. However, more work is still needed to reach fully satisfying and valid results.

To begin, the simplified vibrational models, spring mass and FEM models, developed in Section 3.1 to simulate the vibrational behavior of one single E-TEST cryostat fin, still need refinement to better reflect reality. The most promising approach is the mass-spring model. It could be improved by increasing the number of masses and springs and adjusting the parameter values to better match the experimental data. Then, once an accurate model is achieved, the next goal would be to scale it to the full E-TEST cryostat, to predict its vibrational behavior, and, later, to estimate its thermal noise.

In addition, regarding the RHX design, this thesis introduced new circular RHX with vertical fins. These appear to be the most promising designs, using one-size fins for the E-TEST prototype and two-size fins for the ET cryostat. However, two important points must still be investigated to validate and improve this design. These are discussed below. It is important to note that this discussion applies to the general circular vertical RHX design and is valid for both cryostats.

The circular RHX with vertical fins design presented in this thesis implies fins with uniform thickness that are placed all around the circular internal and external RXH structures, with the ERHX fins intertwined with the IRHX fins. This causes uneven spacing between adjacent fins, as shown in Figure 7.1a, which complicates the assembly. One solution that could be studied is to design the fins with a varying thickness that decreases along their width. A schematic top view of the resulting RHX is shown in Figure 5.4. As it can be seen, this fin shape makes the spacing between the fins

uniform, simplifying the assembly. In addition, this shape could improve the thermal performance of the cryostat.

Indeed, in this thesis, the entire IRHX and ERHX were each represented by one single node of the thermal node model. Therefore, the fins were assumed to have a uniform temperature equal to the IRHX and ERHX structure temperatures. However, in reality, the fin temperature is not uniform. In fact, the ERHX fin tips are further from the cold source and are therefore warmer. A thinner tip could help it cool more quickly. This effect should be studied and the general impact of this design on the general thermal performence of the cryostats should be evaluated using a more detailed thermal model with additional temperature nodes along the width of the fins.

Moreover, with this variable thickness, the fins could be placed more densely around the RHX, allowing for a greater number of fins in both the IRHX and the ERHX, potentially increasing the overall radiative surface.

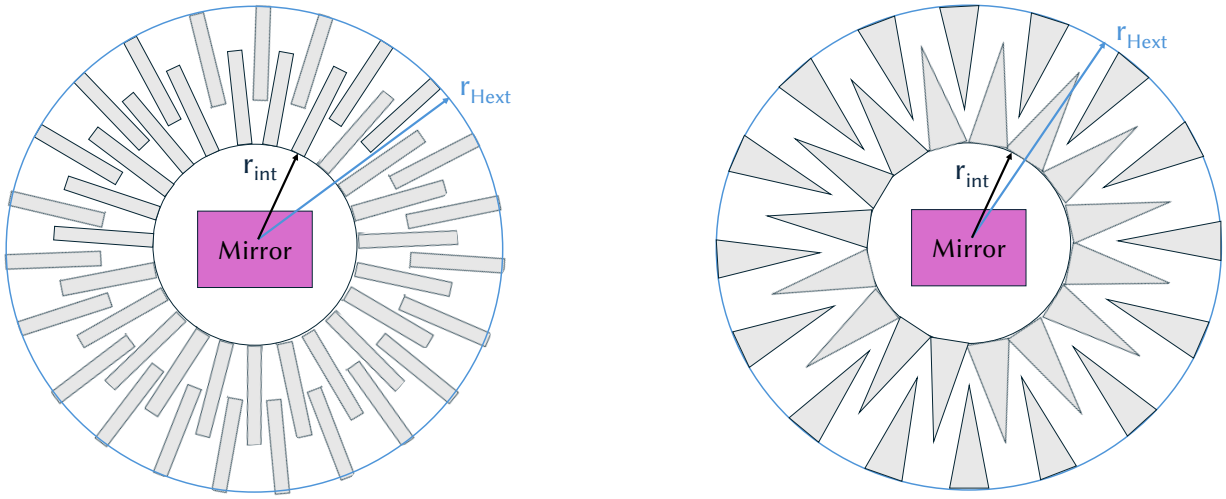

(a) Constant thickness.

(b) Decreasing thickness with fin width.

Figure 7.1: Schemes of the top view of the circular RHX with vertical fins, comparing the case of constant fin thickness and fin thickness that decreases along the fin width.

This alterative fin shape design could also be beneficial for the horizontal fins. It would reduce their bending and may also improve the cooling as for the vertical case.

Another important topic for future work is the evaluation of thermal noise in the fins. This is even more important for vertical fins, which could vibrate in the direction of the laser beam path and therefore affect the measurements.

Finally, it is necessary to study more deeply the optimal fin geometry that would maximize emissivity without excessively increasing the fin thickness, following the ideas discussed in Section 4.2.2. A particularly interesting case to explore is the honeycomb structure painted in black since it has already been found that it could enable the E-TEST cryostat to reach a mirror temperature of $20.4\,\mathrm{K}$ instead of the current $22\,\mathrm{K}$. In addition, the emissivity of such a structure can be enhanced by playing with the dimensions of the honeycomb cells.

LIST OF FIGURES

LIST OF TABLES

BIBLIOGRAPHY

[1] NASA: page edited by T. Vogel. Gravitational waves. https://science.nasa.gov/mission/hubble/science/science-behind-the-discoveries/hubble-gravity-waves, Accessed in Avril 2025.

[2] 2025-IOP Institute Of Physics. Gravitational waves. https://www.iop.org/gravitational-waves, Accessed in Avril 2025.

[3] LIGO Laboratory. Ligo: Global collaboration. https://www.ligo.caltech.edu/page/observatories-collaborations, Accessed in Avril 2025.

[4] T. Yamada et al. High performance thermal link with small spring constant for cryogenic applications. *Cryogenics*, 116:103280, 2021.

[5] T. Tomaru et al. *Vibration-Free Pulse Tube Cryocooler System for Gravitational Wave Detectors, Part I: Vibration-Reduction Method and Measurement*, pages 695–702. 01 2005.

[6] R. X Adhikari et al. Ligo voyager upgrade: Design concept. Technical report, California Institute of Technology and Massachusetts Institute of Technology and LIGO Hanford Observatory and LIGO Livingston Observatory, 2024.

[7] B. Shapiro et al. Cryogenically cooled ultra low vibration silicon mirrors for gravitational wave observatories. *Cryogenics*, 81:83–92, 2017.

[8] Nikhef et al. E-test prototype design report. 2022.

[9] ET Steering Committee Editorial Team. Design report: Update 2020 for the einstein telescope. Semptember 2020.

[10] T. Li. Triangle versus 2l geometry for the einstein telescope. KU Leuven:21 May 2025.

[11] A. Utina et al. Etpathfinder: a cryogenic testbed for interferometric gravitational-wave detectors. *Class. Quantum Grav. 39*, 2022.

[12] A. Xhahi et al. Conceptual design of a sorption-based cryochain for the etpathfinder. *Cryogenics*, 134:103717, 2023.

[13] L. Jacques et al. Cryogenic radiative cooling of a large payload for gravitational wave detector: design and results of the e-test project. Technical report, University of Liège: Centre Spatial de Liège and Precision and Mechatronics Laboratory et al., 2022.

[14] C. Lenaerts and L. Jacques. E-test prototype assembly: Cryostat assembly procedure. Ref. ETEST-CSL-PR-22001, issue 1.0, 24 August 2023.

[15] S. Grohmann et al. Et-lf tm tower design concepts: Integration of fundamental requirements and implications on infrastructure. 2025.

[16] X. Koroveshi et al. Cryogenic payloads for the einstein telescope: Baseline design with heat extraction, suspension thermal noise modeling, and sensitivity analyses. *Physical Review D 108, 123009*, 2023.

[17] on behalf of ISB Divisions I S. Grohmann and IV. Et-lf tm tower integration. Bologna: 2025.

[18] T. Bergman et al. *Fundamentals of Heat and Mass Transfer*. John Wiley Son: Seventh edition, 2011.

[19] L. Jacques. Aero-0038: Thermal analysis of space systems: Radiative heat exchanges modelling. 2025.

[20] S. L. Rickman. Form factors, grey bodies and radiation conductances. Thermal and Fluids Analysis Workshop, Pasadena, California, August 2012.

[21] Lake Shore Cryotronics. Phosphor bronze wire. https://www.lakeshore.com/docs/default-source/product-downloads/catalog/lstc_wire_l.pdf. Accessed in March 2025.

[22] NIST. Material Properties: Ti 6Al 4V (UNS R56400). https://trc.nist.gov/cryogenics/materials/Ti6Al4V/Ti6Al4V_rev.htm. Accessed in March 2025.

[23] S. H. Kim et al. Emissivity measurement of coated copper and aluminum samples at 80 k. *AIP Conf. Proc. 1573, 500–506*, 2017.

[24] J. R. Howell et al. *Thermal Radiation Heat Transfer 7h edition*. CRC Press, 2021.

[25] NIST. Material Properties: 6061-T6 Aluminum (UNS A96061). https://trc.nist.gov/cryogenics/materials/6061%20Aluminum/6061_T6Aluminum_rev.htm. Accessed in March 2025.

[26] P. Hanzellka et al. Cryogenics 50. 2010, p737-742.

[27] The MathWorks. Documentation:ode23. https://www.mathworks.com/help/matlab/ref/ode23.html, Accessed in May 2025.

[28] M. Ando et al. A database of metallic materials emissivities and absorptivities for cryogenics. *IOP Conf. Series: Materials Science and Engineering 502*, 2019.

[29] Fluke Corporation 2007. Emissivity values of common materials. http://www.fluke.com, Accessed in Avril 2025.